The statistical model for unpolarized and polarized parton distributions and fragmentations : a comparison with experiments

Claude Bourrely, Franco Buccella, Jacques Soffer

THE STATISTICAL MODEL FOR UNPOLARIZED AND POLARIZED PARTON DISTRIBUTIONS AND FRAGMENTATIONS: A COMPARISON WITH EXPERIMENTS

C. BOURRELY[1], F BUCCELLA[2] and J. SOFFER[3]

[1]Centre de Physique Théorique (UMR 6207)[1],
CNRS Luminy case 907,
13288 Marseille cedex 9, France

[2]Dipartimento di Scienze Fisiche, Università di Napoli,
Via Cintia, I-80126, Napoli, Italy
INFN, Sezione di Napoli

[3]Department of Physics, Temple University,
Philadelphia, Pennsylvania 19122-6082, USA

Updated March 2008

Abstract

In the framework of the statistical model for parton distributions and fragmentations functions we present a comparison of the model with a large set of unpolarized and polarized experimental data, the agreement with data supports our approach.

CPT-2003/P.4561
bourrely@cpt.univ-mrs.fr
jsoffer@temple.edu

[1]UMR 6207 is Unité Mixte de Recherche du CNRS and of Universités Aix-Marseille I and Aix-Marseille II and of Université du Sud Toulon-Var, laboratoire affilié à la FRUMAM.

Contents

1 Polarized Parton Distributions

We give a brief review of the parton distributions functions which are described in Refs. [1-6].

1.1 Quarks

The density functions are given by [2] :

$$xu^+(x) = \frac{AX_{0u}^+ x^b}{\exp[(x - X_{0u}^+)/\bar{x}] + 1} + \frac{\tilde{A}x^{\tilde{b}}}{\exp[\frac{x}{\bar{x}}] + 1} \tag{1}$$

$$xu^-(x) = \frac{AX_{0u}^- x^b}{\exp[(x - X_{0u}^-)/\bar{x}] + 1} + \frac{\tilde{A}x^{\tilde{b}}}{\exp[\frac{x}{\bar{x}}] + 1} \tag{2}$$

$$xd^+(x) = \frac{AX_{0d}^+ x^b}{\exp[(x - X_{0d}^+)/\bar{x}] + 1} + \frac{\tilde{A}x^{\tilde{b}}}{\exp[\frac{x}{\bar{x}}] + 1} \tag{3}$$

$$xd^-(x) = \frac{AX_{0d}^- x^b}{\exp[(x - X_{0d}^-)/\bar{x}] + 1} + \frac{\tilde{A}x^{\tilde{b}}}{\exp[\frac{x}{\bar{x}}] + 1} \tag{4}$$

$$A = 1.74938 \tag{5}$$
$$b = 0.40962 \pm 0.00438^{(*)} \tag{6}$$
$$\bar{x} = 0.09907 \pm 0.00110^{(*)} \tag{7}$$
$$X_{0u}^+ = 0.46128 \pm 0.00338^{(*)} \tag{8}$$
$$X_{0u}^- = 0.29766 \pm 0.00303^{(*)} \tag{9}$$
$$X_{0d}^+ = 0.22775 \pm 0.00294^{(*)} \tag{10}$$
$$X_{0d}^- = 0.30174 \pm 0.00239^{(*)} \tag{11}$$
$$\tilde{A} = 0.08318 \pm 0.00157 \tag{12}$$
$$\tilde{b} = -0.25347 \pm 0.00318^{(*)} \tag{13}$$

note:
The temperature $\bar{x}$ is identical for quarks, antiquarks and gluons.

[2] Values marked with an asterisk are free parameters of the model. The input scale is $Q_0^2 = 4\text{GeV}^2$, and $\Lambda(\overline{MS}) = 300\text{MeV}$. The evolution is performed at NLO.

1.2 Antiquarks

The density functions are given by:

$$x\bar{u}^+(x) = \frac{\bar{A}}{X_{0u}^-} \cdot \frac{x^{\bar{b}}}{\exp[(x + X_{0u}^-)/\bar{x}] + 1} + \frac{\tilde{A}x^{\tilde{b}}}{\exp[\frac{x}{\bar{x}}] + 1} \tag{14}$$

$$x\bar{u}^-(x) = \frac{\bar{A}}{X_{0u}^+} \cdot \frac{x^{\bar{b}}}{\exp[(x + X_{0u}^+)/\bar{x}] + 1} + \frac{\tilde{A}x^{\tilde{b}}}{\exp[\frac{x}{\bar{x}}] + 1} \tag{15}$$

$$x\bar{d}^+(x) = \frac{\bar{A}}{X_{0d}^-} \cdot \frac{x^{\bar{b}}}{\exp[(x + X_{0d}^-)/\bar{x}] + 1} + \frac{\tilde{A}x^{\tilde{b}}}{\exp[\frac{x}{\bar{x}}] + 1} \tag{16}$$

$$x\bar{d}^-(x) = \frac{\bar{A}}{X_{0d}^+} \cdot \frac{x^{\bar{b}}}{\exp[(x + X_{0d}^+)/\bar{x}] + 1} + \frac{\tilde{A}x^{\tilde{b}}}{\exp[\frac{x}{\bar{x}}] + 1} \tag{17}$$

$$\bar{A} = 1.90801 \pm 0.12627^{(*)} \tag{18}$$

$$\bar{b} = 2b = 0.81924 \tag{19}$$

$xs(x) = x\bar{s}(x) = \frac{1}{4}(x\bar{u}(x) + x\bar{d}(x))$

$x\Delta s(x) = x\Delta\bar{s}(x) = \frac{1}{3}(x\Delta\bar{d}(x) - x\Delta\bar{u}(x))$. This assumption was removed in a new version of the model, see [6].

$$xs^h(x, Q_0^2) = \frac{AX_{0u}^+ x^{b_s}}{\exp[(x - X_{0s}^h)/\bar{x}] + 1} \, \frac{\ln\left(1 + \exp\left[kX_{0s}^h/\bar{x}\right]\right)}{\ln\left(1 + \exp\left[kX_{0u}^+/\bar{x}\right]\right)} + \frac{\tilde{A}_s x^{\tilde{b}}}{\exp(x/\bar{x}) + 1} \,, \tag{20}$$

$$x\bar{s}^h(x, Q_0^2) = \frac{\bar{A}(X_{0d}^+)^{-1} x^{2b_s}}{\exp[(x + X_{0s}^{-h})/\bar{x}] + 1} \, \frac{\ln\left(1 + \exp\left[-kX_{0s}^{-h}/\bar{x}\right]\right)}{\ln\left(1 + \exp\left[-kX_{0d}^+/\bar{x}\right]\right)} + \frac{\tilde{A}_s x^{\tilde{b}}}{\exp(x/\bar{x}) + 1} \,. \tag{21}$$

$$A = 1.74938,\ \bar{A} = 1.90801,\ X_{0u}^+ = 0.46128,\ X_{0d}^+ = 0.22775,$$
$$\bar{x} = 0.09907,\ \tilde{b} = -0.25347,\ k = 1.42\,. \tag{22}$$

1.3 Gluon

$$xG(x) = \frac{A_G x^{b_G}}{\exp[x/\bar{x}] - 1} \tag{23}$$

$$A_G = 14.27535 \tag{24}$$

$$b_G = 1 + \tilde{b} = 0.74653 \tag{25}$$

$$x\Delta G(x) = 0 \qquad \text{at} \quad Q_0^2 = 4\mathrm{GeV}^2 \tag{26}$$

Charm

The charm is set to 0 at $Q_0^2 = 4\mathrm{GeV}^2$

2 Parton Fragmentation Functions

We propose to parametrize the fragmentation functions of the baryons octet with a statistical model as in the case of PDF.

For the quarks $q = u, s, d$ the FF are expressed as

$$D_q^B(x, Q_0^2) = \frac{A_q^B X_q^B x^b}{\exp[(x - X_q^B)/\bar{x}] + 1}, \tag{27}$$

where X_q^B is the potential corresponding to the fragmentation $q \to B$ and Q_0^2 is an initial scale, given below in Table 1. We will ignore the antiquark FF $D_{\bar{q}}^B$, which are considered to be strongly suppressed. The heavy quark FF $D_Q^B(x, Q_0^2)$ for $Q = c, b, t$, which are expected to be large only in the small x region ($x \leq 0.1$ or so), are parametrized by a diffractive term with a vanishing potential

$$D_Q^B(x, Q_0^2) = \frac{\tilde{A}_Q^B x^{\tilde{b}}}{\exp(x/\bar{x}) + 1}. \tag{28}$$

The initial scale Q_0^2, which is flavor dependent in this case, is given below in Table 1 [3]. This FF for $Q \to B$ depends on $\tilde{b}$ and a normalization constant $\tilde{A}_B^Q$ for each baryon B. For the other quarks, we make some reasonable assumptions in order to reduce the number of parameters in addition to b, the universal power of x in Eq. (27). First we have the obvious constraints, namely, $D_u^B = D_d^B$ for $B = p, \Lambda$. Moreover we assume that we need only *four* potentials, two for the proton $X_u^p = X_d^p$ and X_s^p and two for the hyperons $X_u^Y = X_d^Y$ and X_s^Y where $Y = \Lambda, \Sigma^{\pm}, \Xi^-$. Finally for the gluon to baryon FF $D_g^B(x, Q^2)$, which is hard to determine precisely, we take a Bose-Einstein expression with a vanishing potential

$$D_g^B(x, Q_0^2) = \frac{A_g^B x^{\tilde{b}+1}}{\exp(x/\bar{x}) - 1}. \tag{29}$$

We assume it has the same small x behavior as the heavy quarks and it is the same for all baryons. The normalization constants A_q^B, A_g^B and $\tilde{A}_Q^B$ are determined by fitting the data.

[3] Due to the fact that the input scale of the t quark is above the highest energy data investigated in this work, it does not contribute to our analysis.

Table 1: Input scales Q_0 and $\Lambda(\overline{MS})$ in GeV unit.

quark	u,d,s	c	b	t
Q_0	0.632	1.4	4.5	175
$\Lambda(\overline{MS})$	0.299	0.246	0.168	0.068

Now, let us report the values of the free parameters we have obtained from the NLO fit:

$$\begin{array}{llll} X_u^p = 0.648, & X_s^p = 0.247, & X_u^\Lambda = 0.296, & X_s^\Lambda = 0.476 \\ b = 0.200, & \tilde{b} = -0.472, & A_g^B = 0.051. & \end{array} \tag{30}$$

Table 2: Values of the normalization constants of the the octet baryons FF

Baryon	q_1	q_2	$A_{q_1}^B$	$A_{q_2}^B$	$\tilde{A}_Q^B$
$p(uud)$	$u=d$	s	0.264	1.168	2.943
$\Lambda(uds)$	$u=d$	s	0.428	1.094	0.720
$\Sigma^+(uus)$	u	s	0.033	0.462	0.180
$\Sigma^-(dds)$	d	s	0.030	0.319	0.180
$\Xi^-(dss)$	d	s	0.023	0.082	0.072

3 Parton distributions and fragmentation functions figures

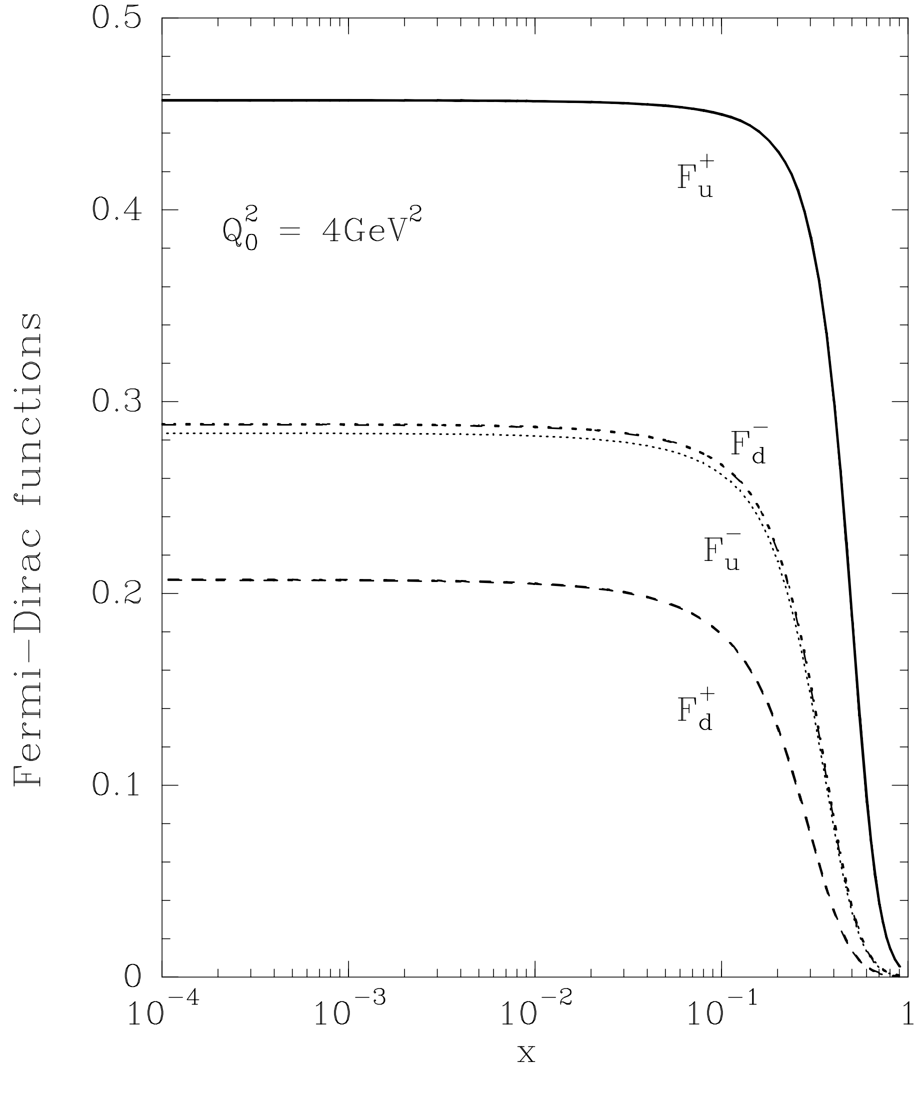

Figure 1: The Fermi-Dirac functions for quarks $F_q^h = X_{0q}^h/(\exp[(x-X_{0q}^h)/\bar{x}]+1)$ at the input energy scale $Q_0^2 = 4\mathrm{GeV}^2$, as a function of x.

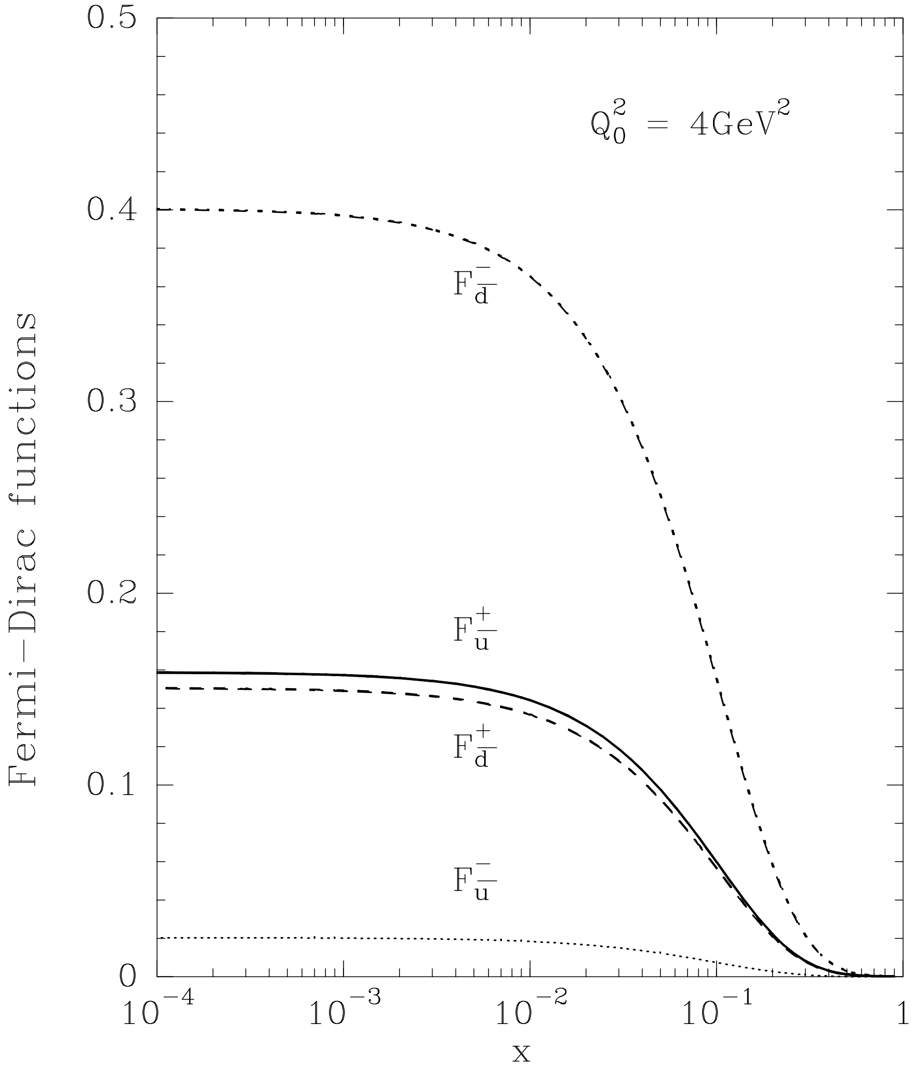

Figure 2: The Fermi-Dirac functions for antiquarks $F_{\bar{q}}^h = 1/X_{0\bar{q}}^h(\exp[(x + X_{0\bar{q}}^h)/\bar{x}] + 1)$ at the input energy scale $Q_0^2 = 4\mathrm{GeV}^2$, as a function of x.

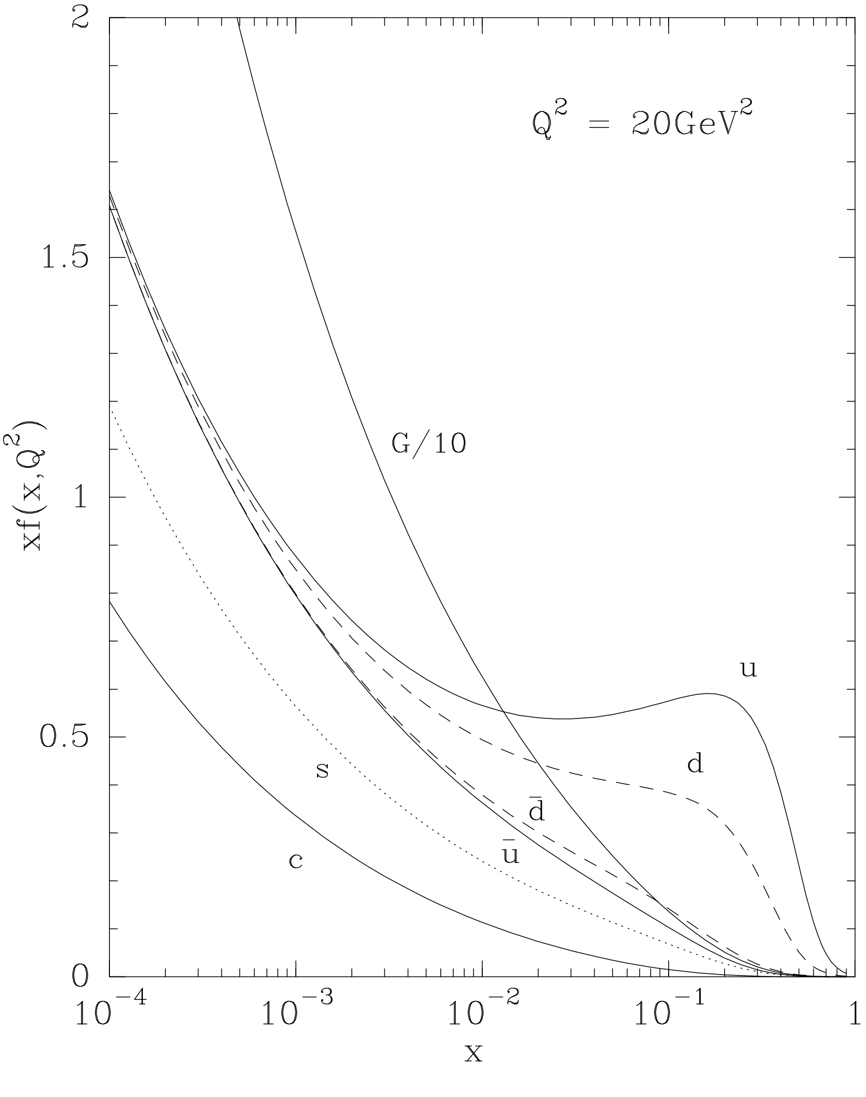

Figure 3: The different unpolarized parton distributions ($f = u$, d, $\bar{u}$, $\bar{d}$, s, c and G) after NLO evolution, at $Q^2 = 20\mathrm{GeV}^2$, as a function of x.

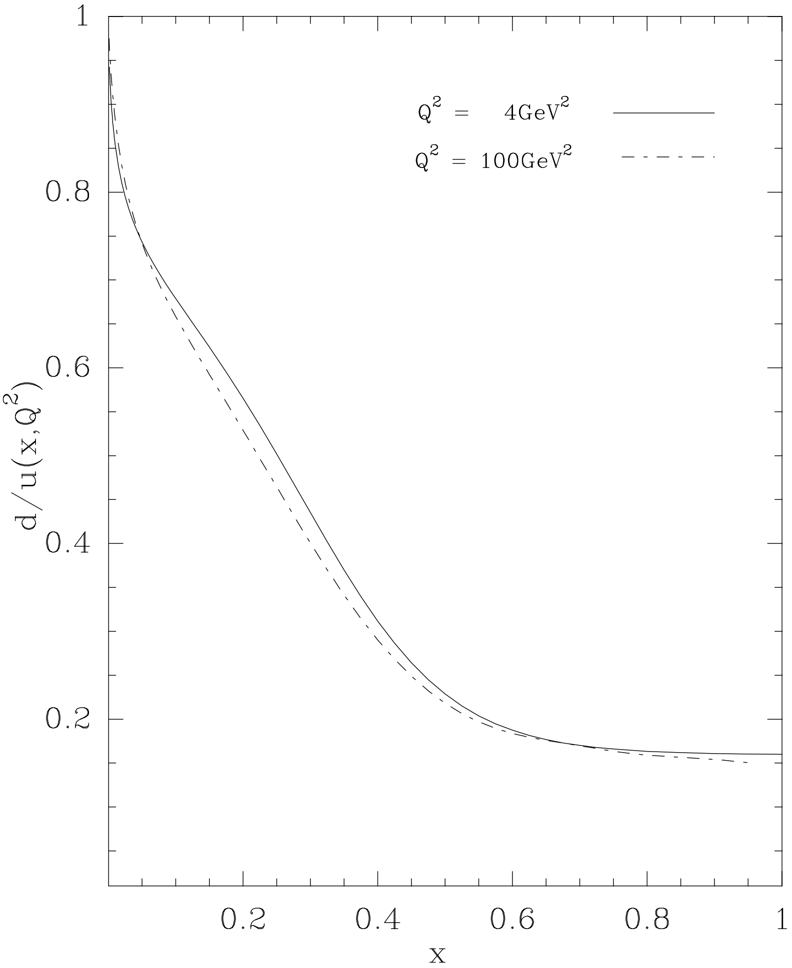

Figure 4: Variation of d/u at large x, for $Q^2 = 4, 100\text{GeV}^2$

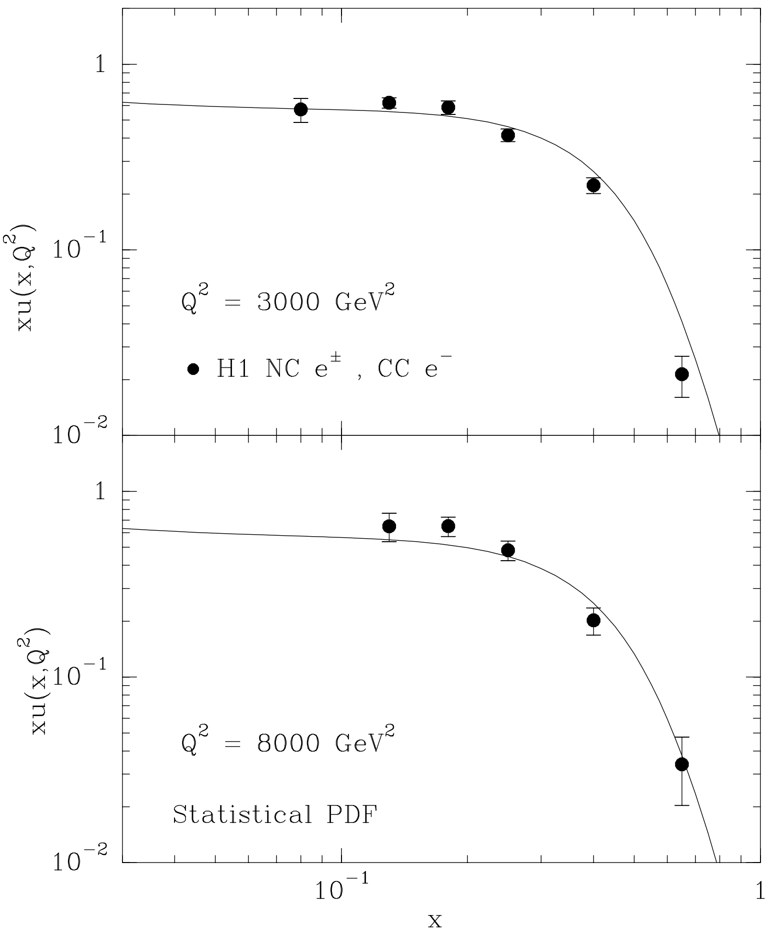

Figure 5: $xu(x, Q^2)$ as function of x for $Q^2 = 3000,\ 8000\mathrm{GeV}^2$, data from H1 collaboration [41, 42].

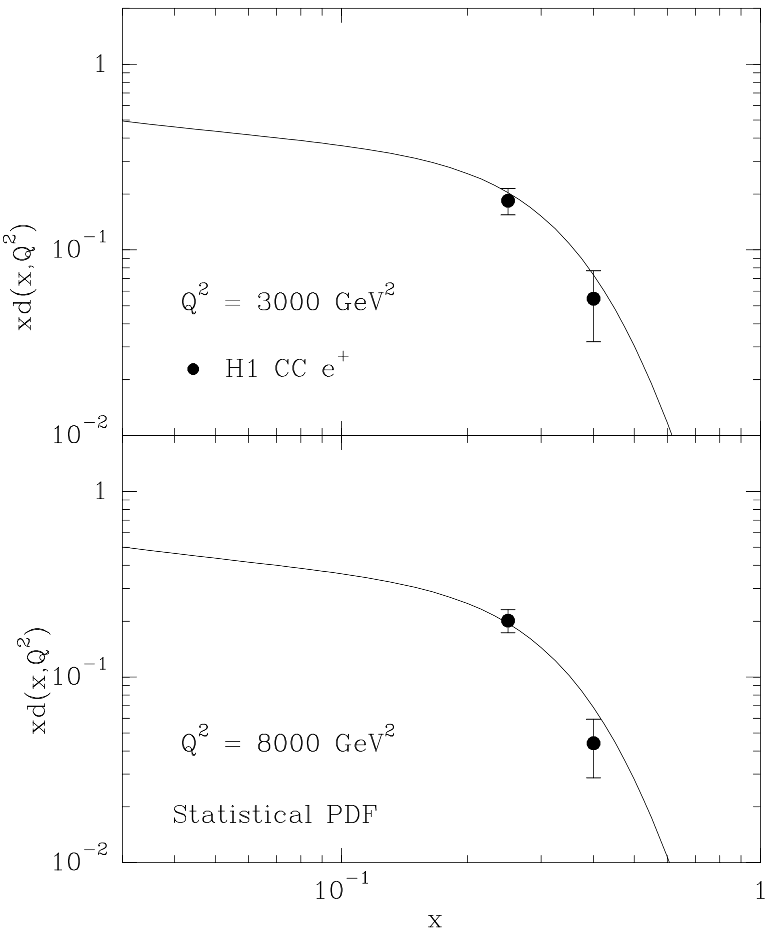

Figure 6: $xd(x, Q^2)$ as function of x for $Q^2 = 3000,\ 8000\mathrm{GeV}^2$, data from H1 collaboration [41, 42].

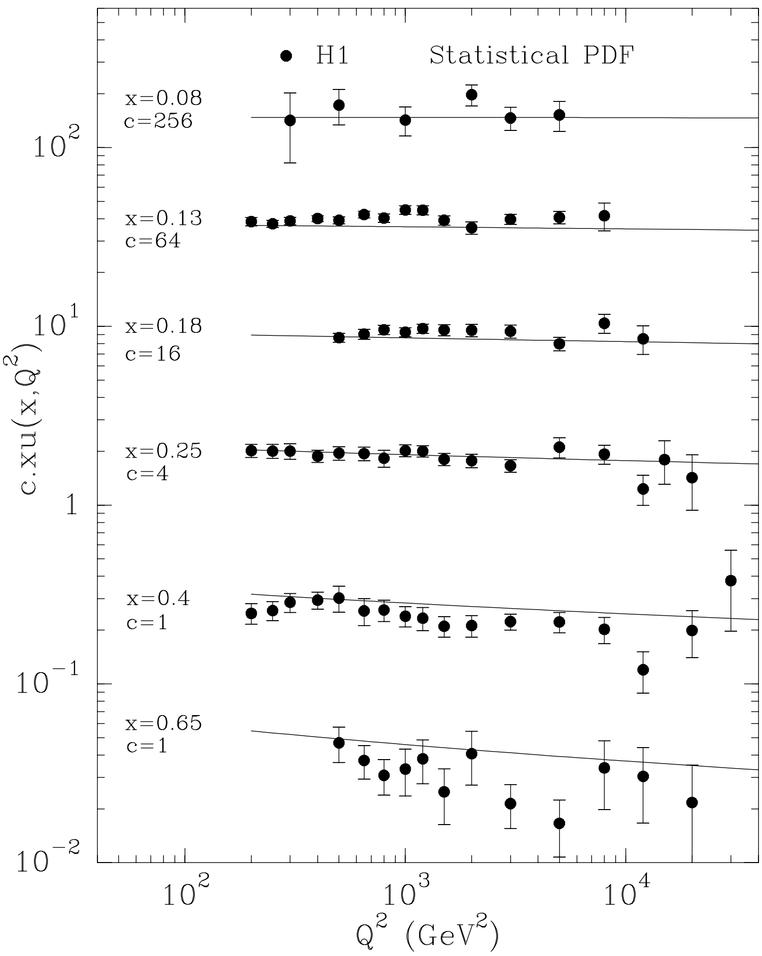

Figure 7: $c \cdot xu(x, Q^2)$ as function of Q^2 for different x bins, data from H1 collaboration [41, 42].

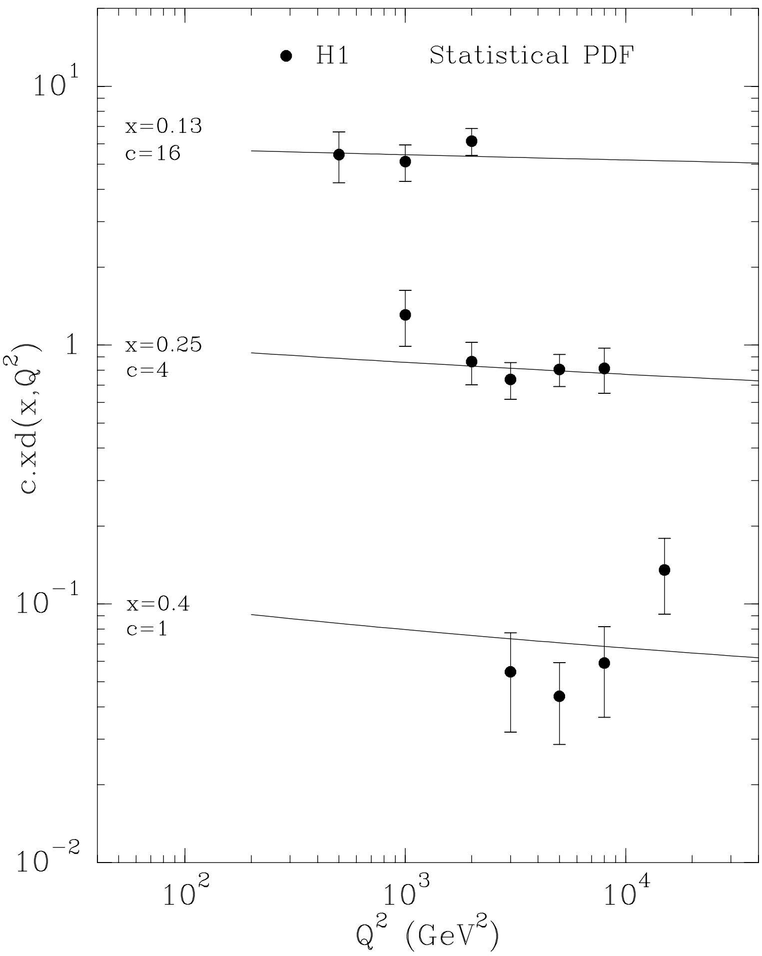

Figure 8: $c \cdot xd(x, Q^2)$ as function of Q^2 for different x bins, data from H1 collaboration [41, 42].

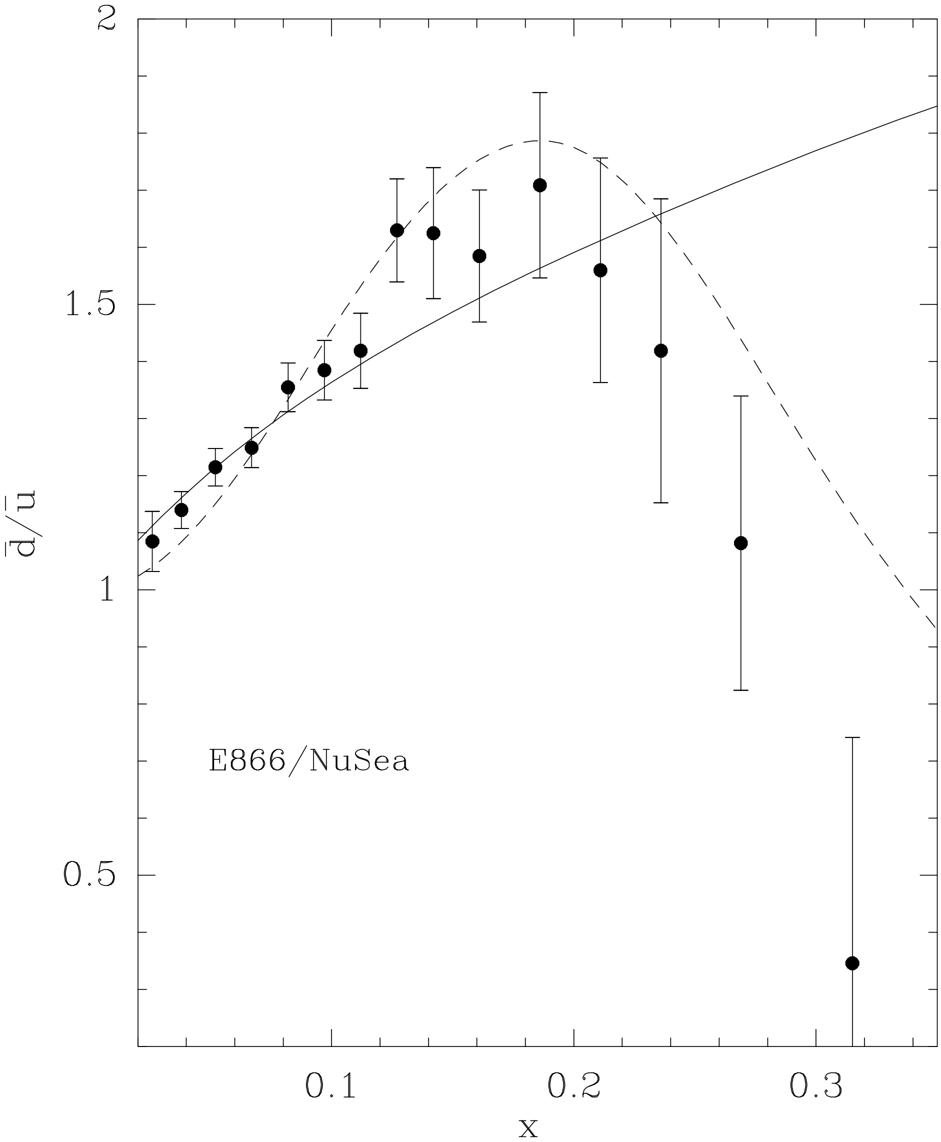

Figure 9: Comparison of the data on $\bar{d}/\bar{u}(x, Q^2)$ from E866/NuSea at $Q^2 = 54\text{GeV}^2$ [25], with the prediction of the statistical model (solid curve) and the set 1 of the parametrization proposed in Ref. [84] (dashed curve).

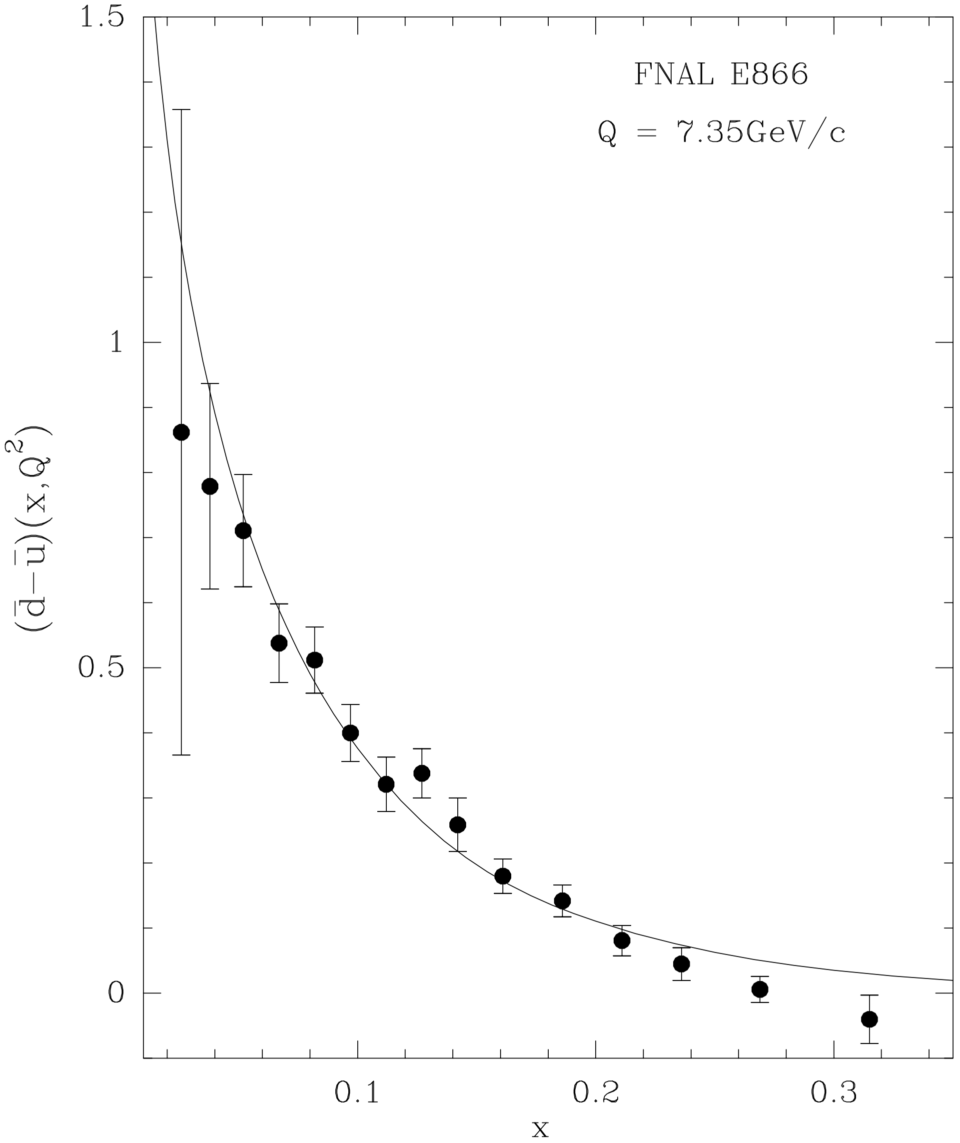

Figure 10: Difference $\bar{d} - \bar{u}$ as a function of x, $Q = 7.35$GeV, experimental results from FNAL-E866.

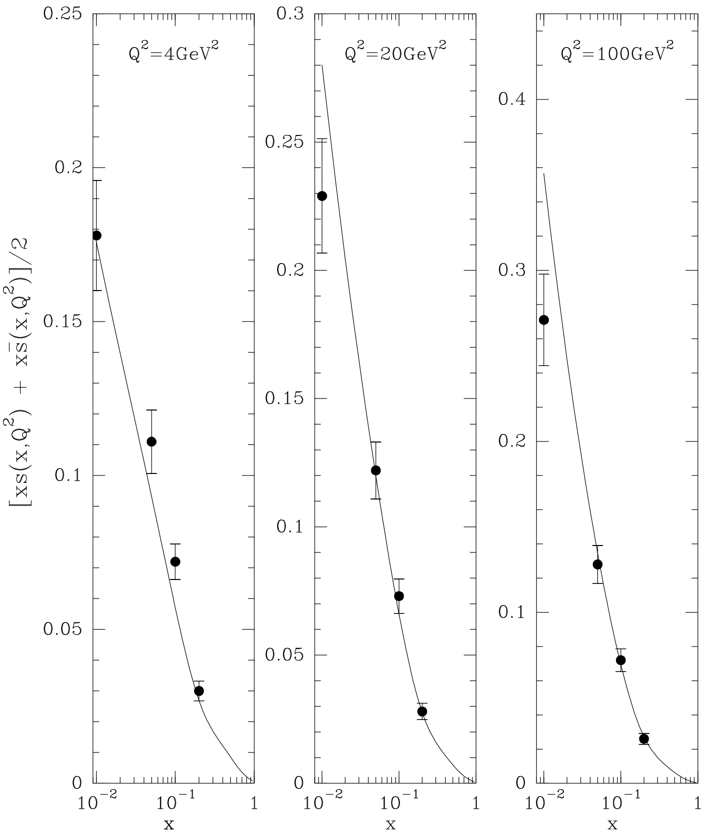

Figure 11: The strange quark distribution $xs(x, Q^2)$ determined at NLO as a function of x for different Q^2 values. Data from CCFR Collaboration [14].

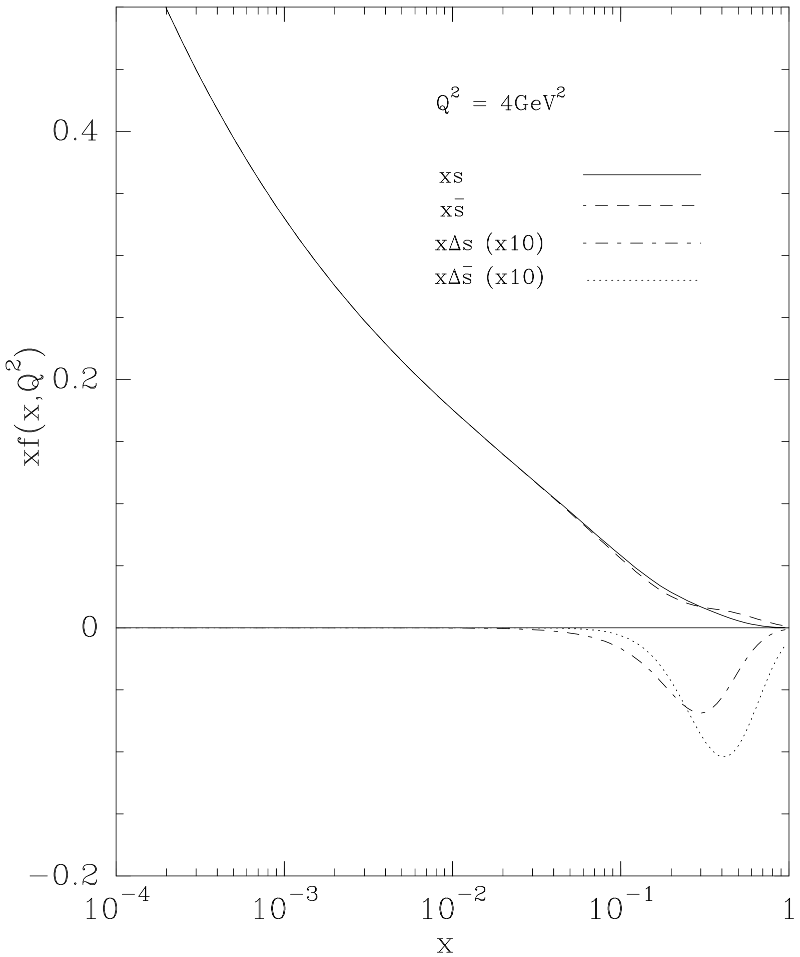

Figure 12: The unpolarized and polarized strange quark and antiquark distributions determined at NLO as a function of x for $Q^2 = 4\text{GeV}^2$.

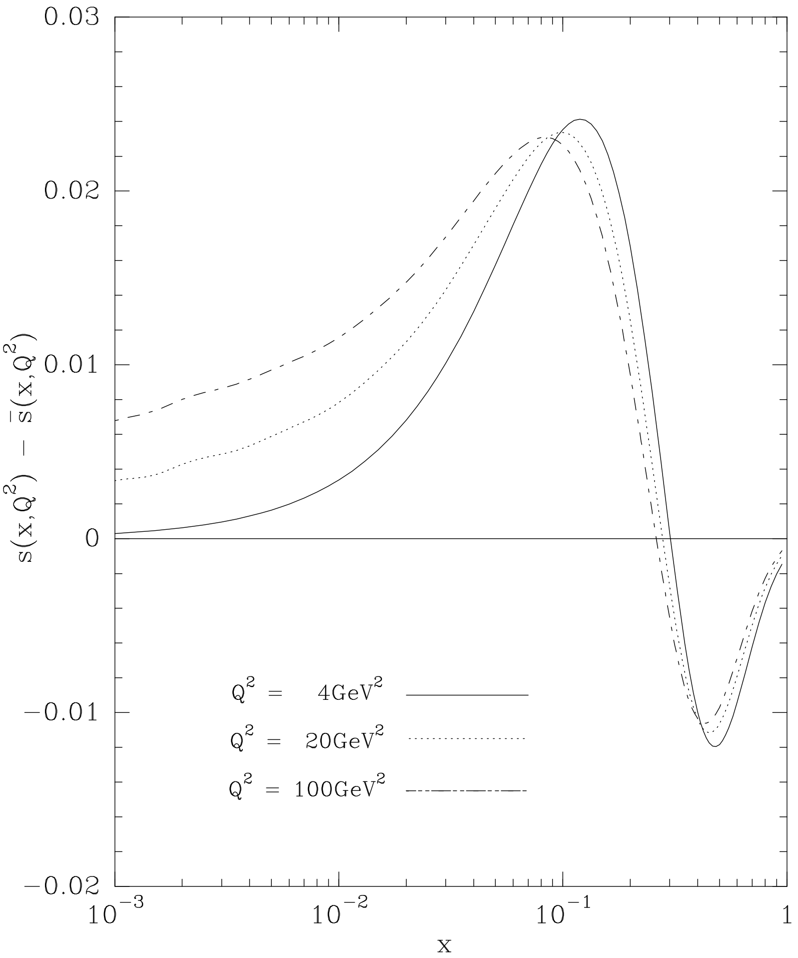

Figure 13: The difference $s - \bar{s}$ quark distributions determined at NLO as a function of x for $Q^2 = 4, 20, 100\text{GeV}^2$.

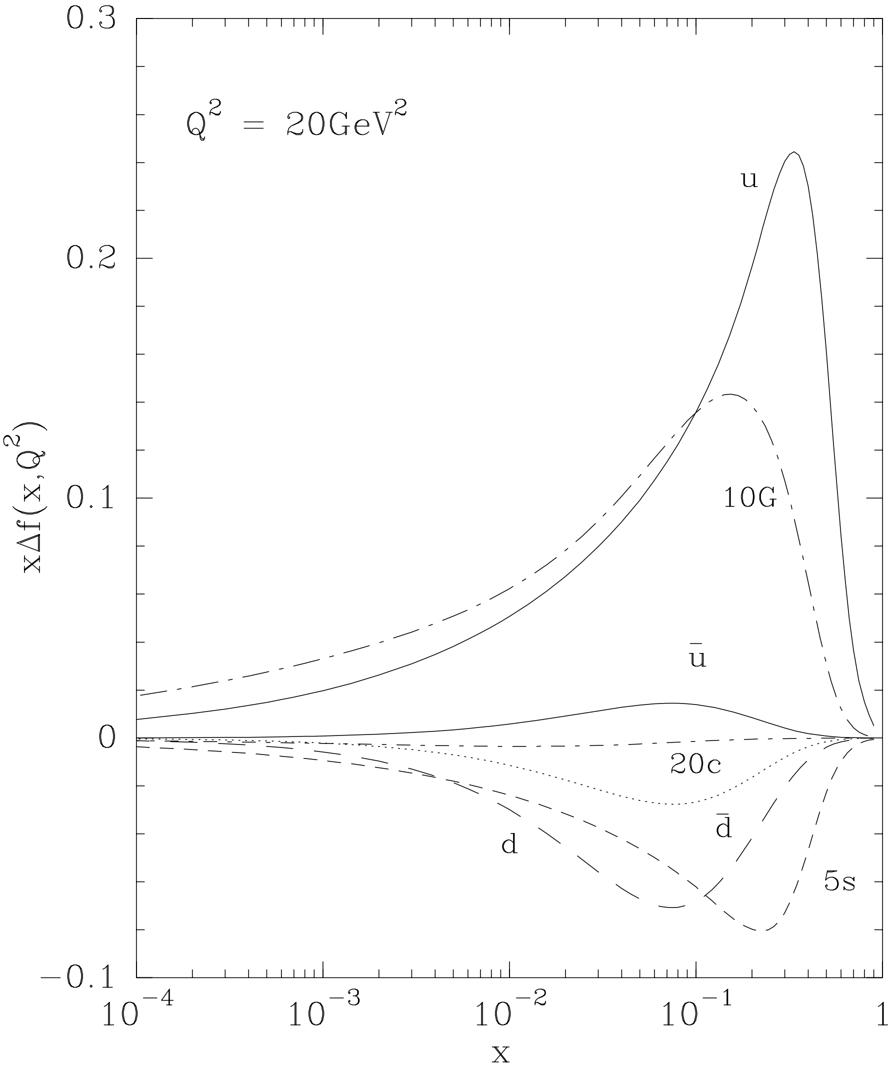

Figure 14: The different polarized parton distributions after NLO evolution, at $Q^2 = 20\mathrm{GeV}^2$, as a function of x.

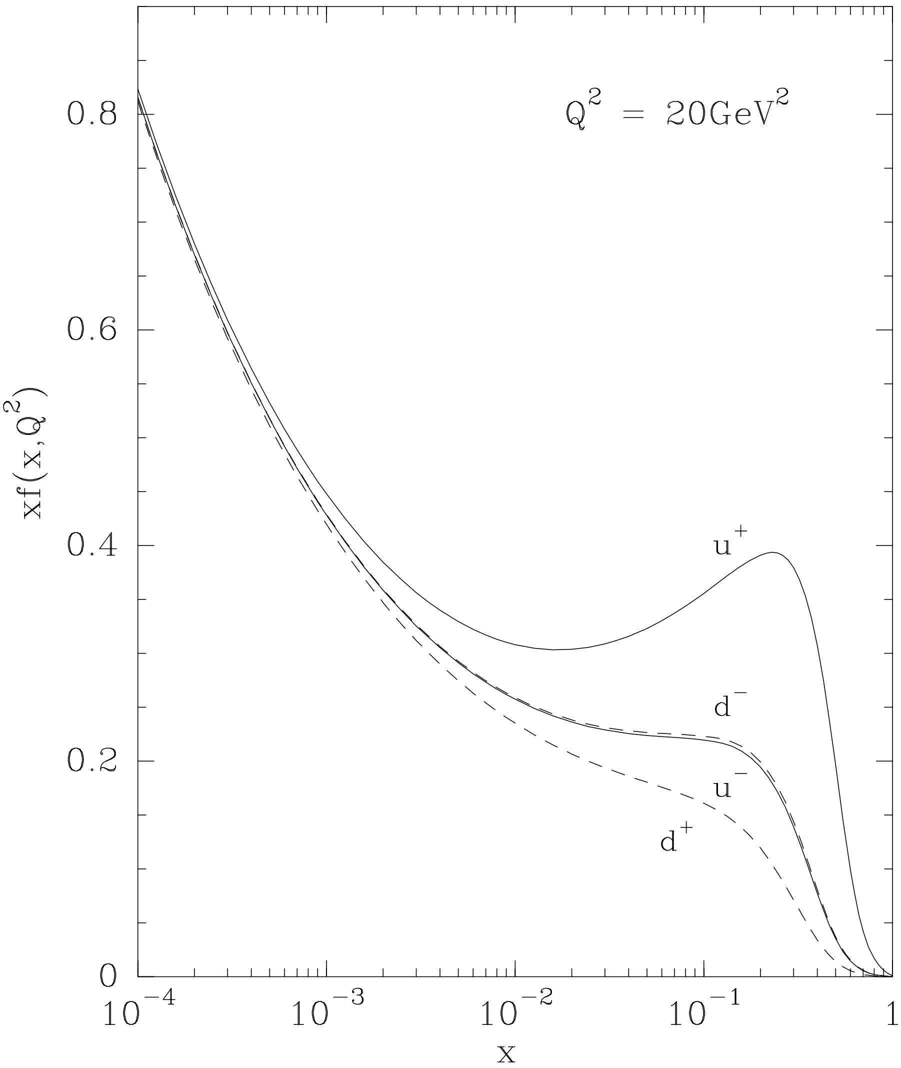

Figure 15: The different helicity components of the light quark distributions after NLO evolution, at $Q^2 = 20\mathrm{GeV}^2$, as a function of x.

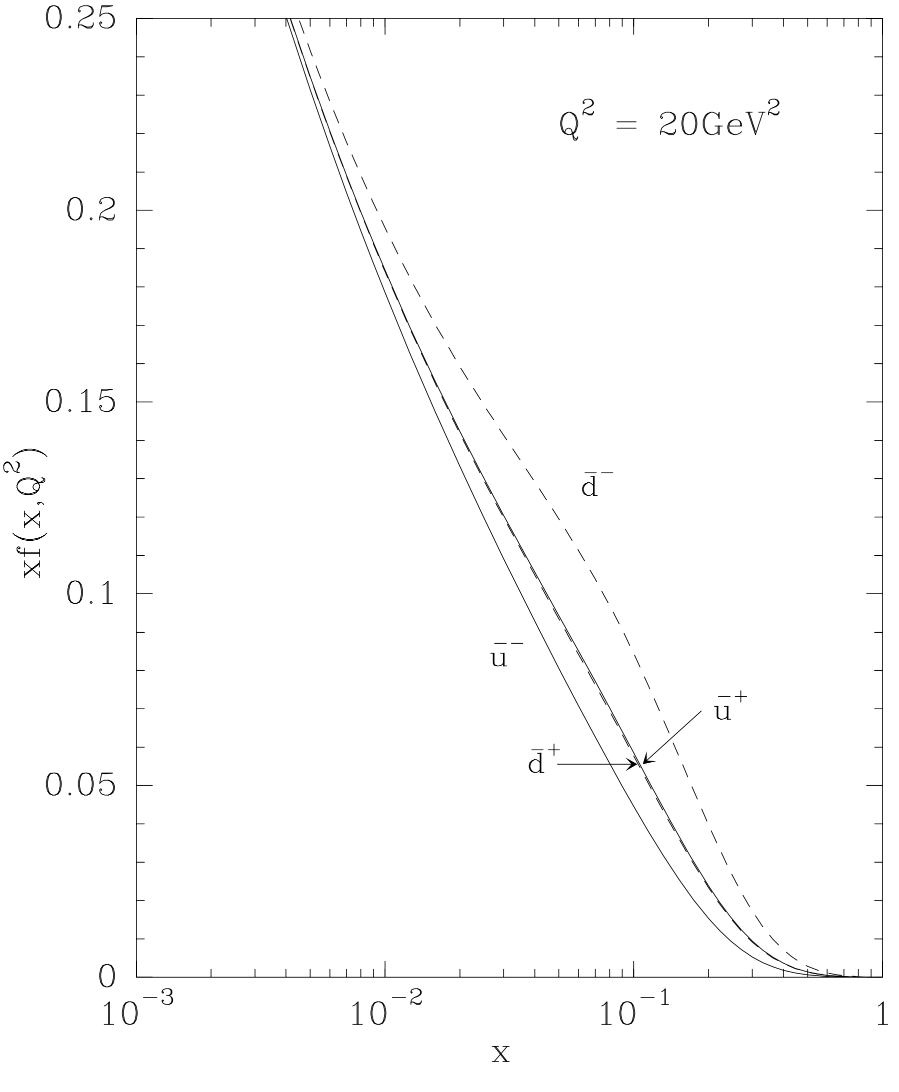

Figure 16: The different helicity components of the light antiquark distributions after NLO evolution, at $Q^2 = 20\mathrm{GeV}^2$, as a function of x.

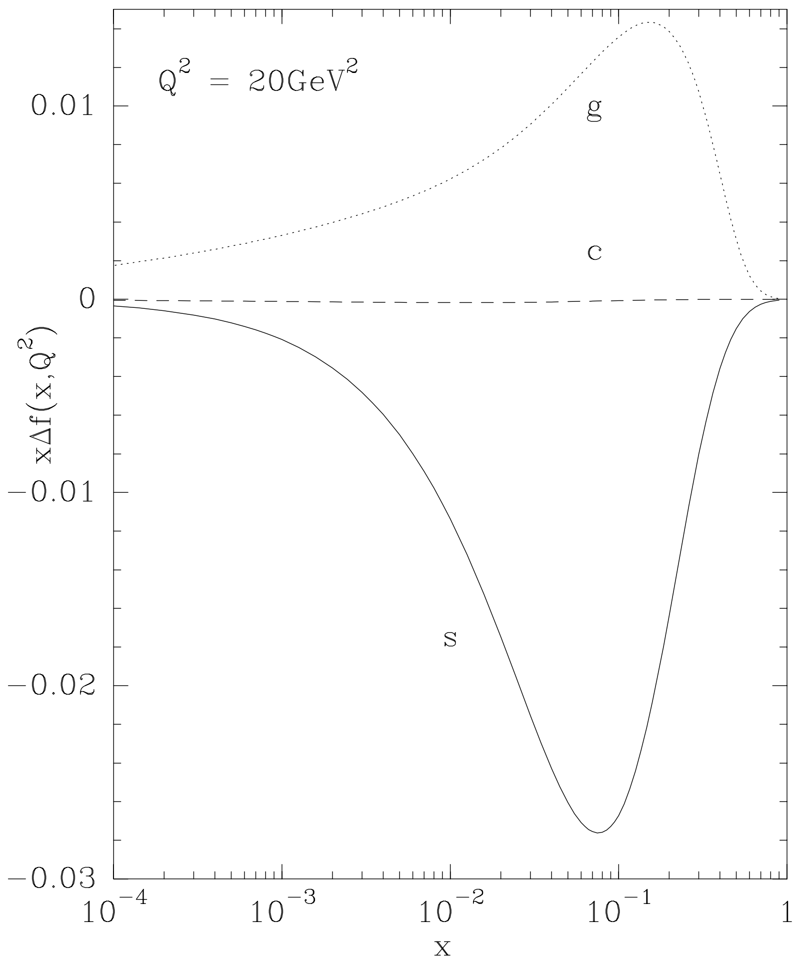

Figure 17: Details of the polarized parton distributions g, s, c, after NLO evolution, at $Q^2 = 20\text{GeV}^2$, as a function of x.

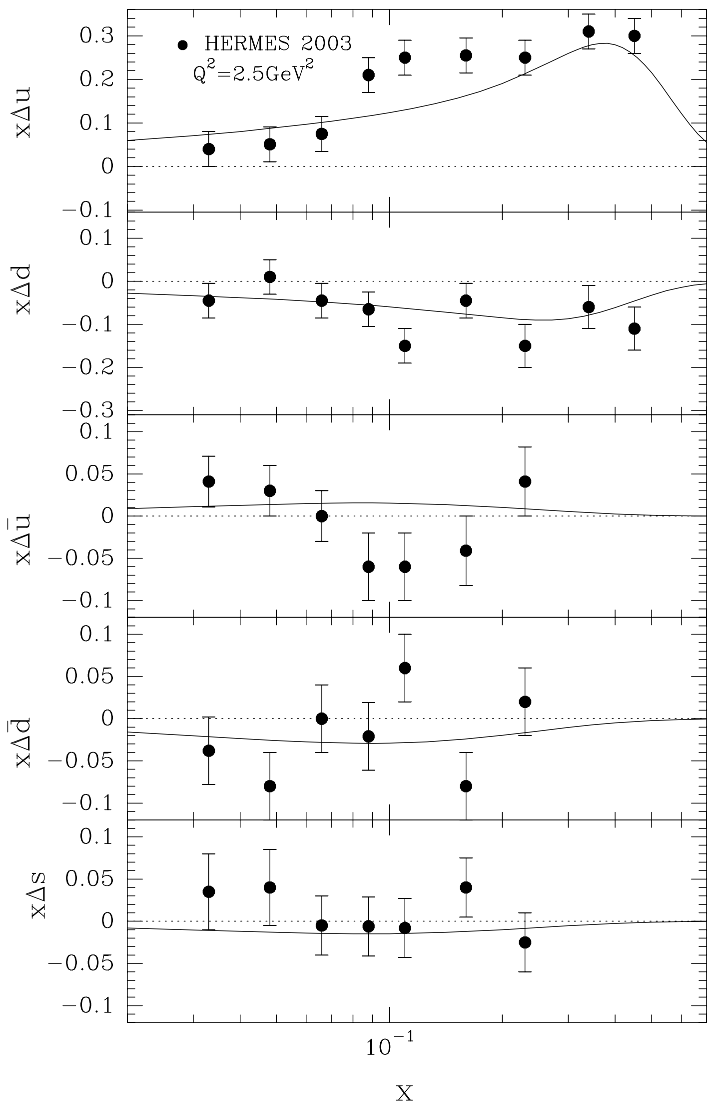

Figure 18: Quark helicity distributions at $< Q^2 >= 2.5\mathrm{GeV}^2$, as a function of x. Data from HERMES Coll. [46].

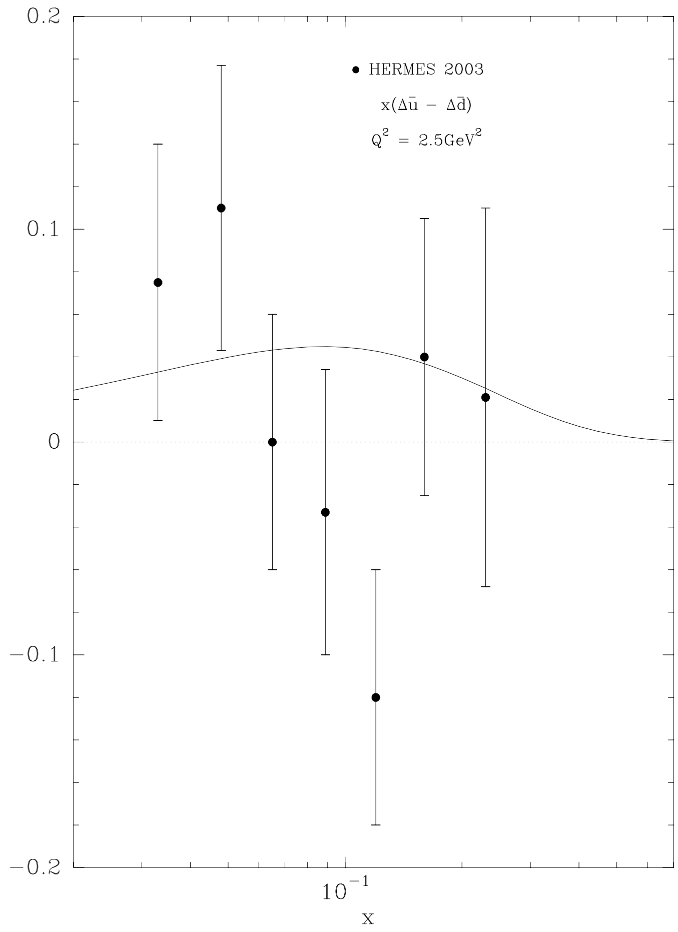

Figure 19: Flavor asymmetry $\Delta\bar{u} - \Delta\bar{d}$ of the light sea quark as a function of x, for $Q^2 = 2.5\text{GeV}^2$. Data from HERMES Coll. [46].

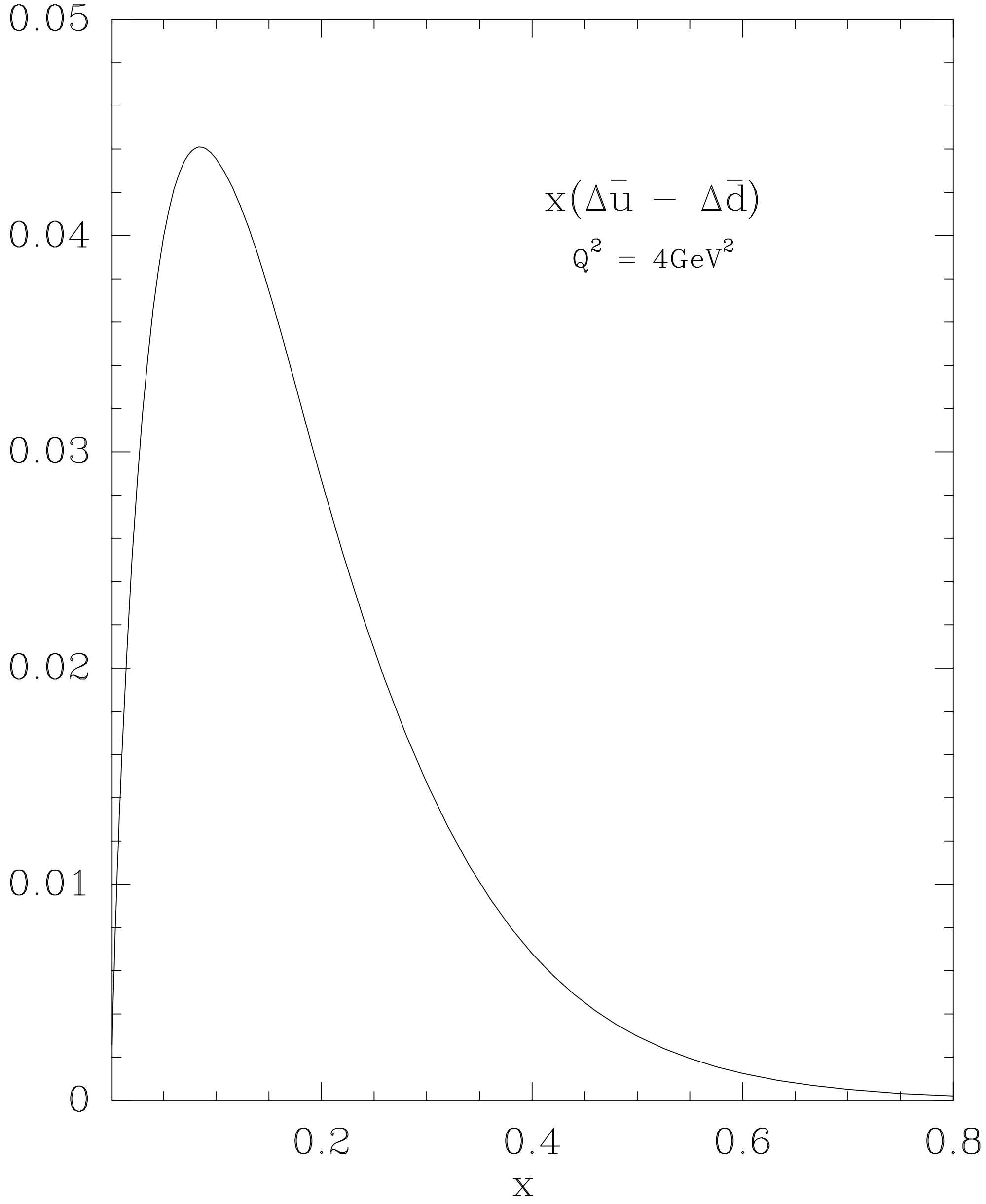

Figure 20: Flavor asymmetry $\Delta\bar{u} - \Delta\bar{d}$ of the light sea quark as a function of x, for $Q^2 = 4\mathrm{GeV}^2$.

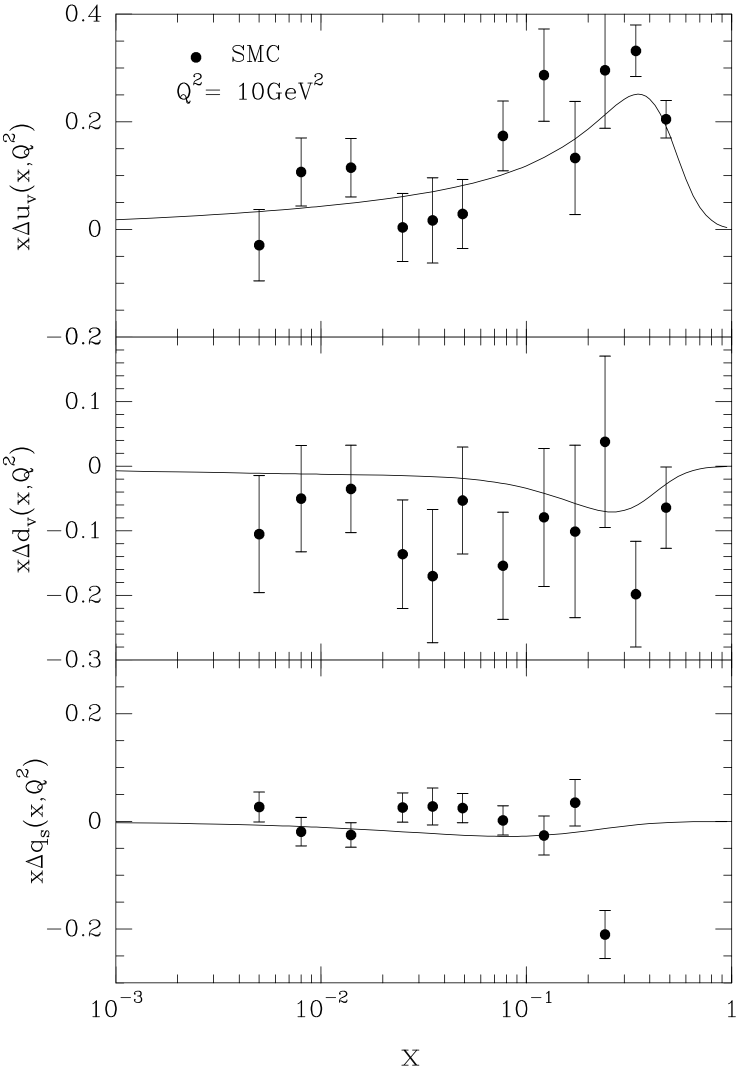

Figure 21: $x\Delta u_v,\ x\Delta d_v,\ x\Delta\bar{q}$ as function of x at fixed $Q^2 = 10\mathrm{GeV}^2$, experiment SMC Coll..

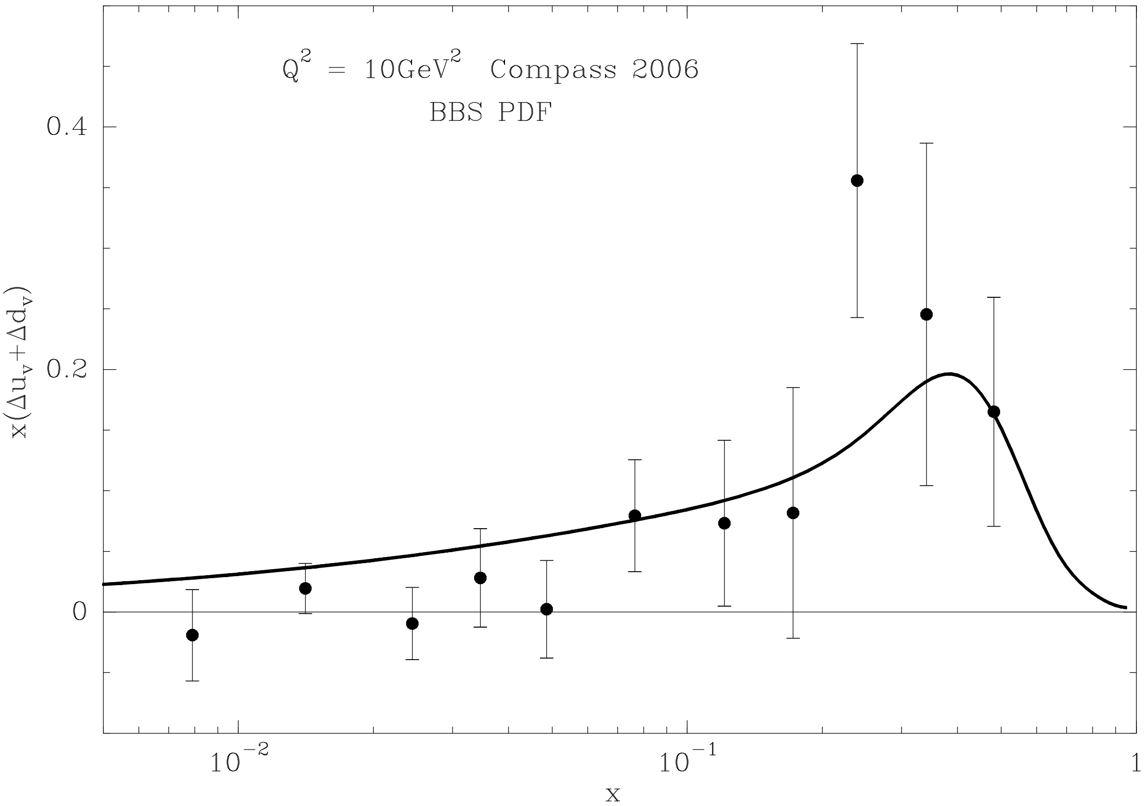

Figure 22: The sum of polarized valence quark distributions determined at NLO as a function of x for $Q^2 = 10\text{GeV}^2$, data from Compass Collaboration [109, 110].

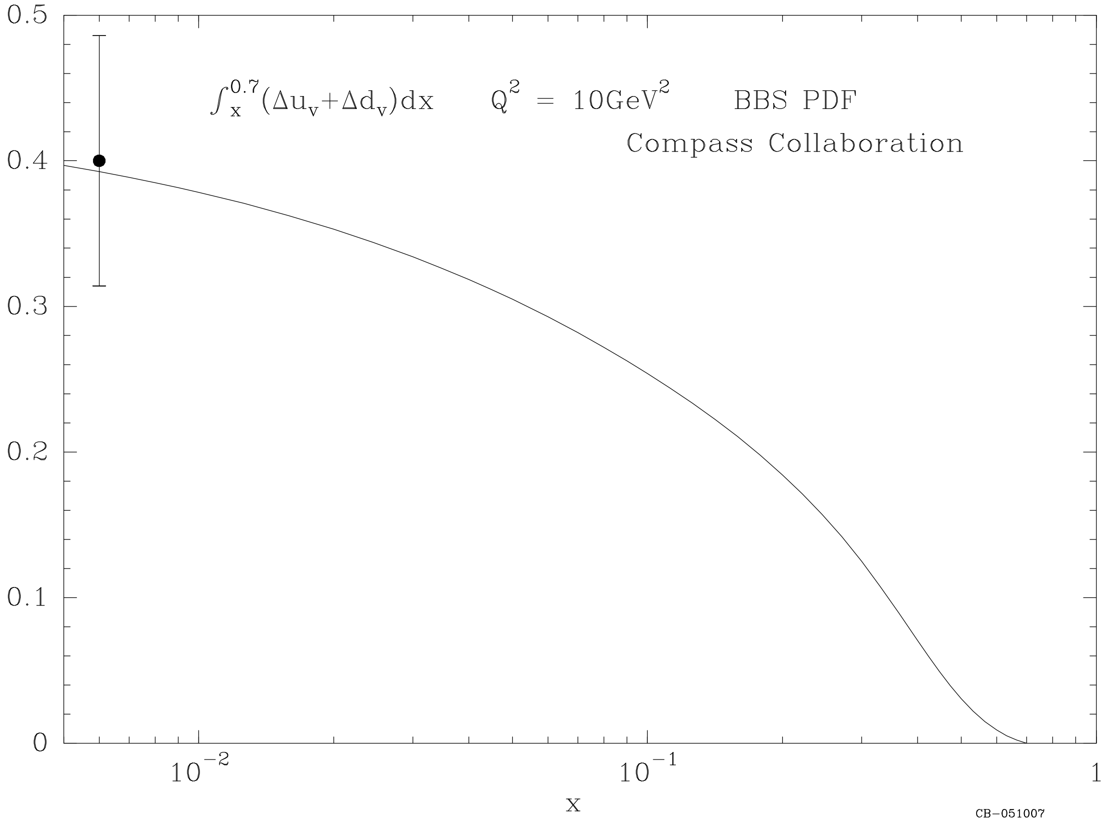

Figure 23: Prediction for the integral $\Delta u_v + \Delta d_v$ determined at NLO as a function of the lower limit x for $Q^2 = 10\text{GeV}^2$.

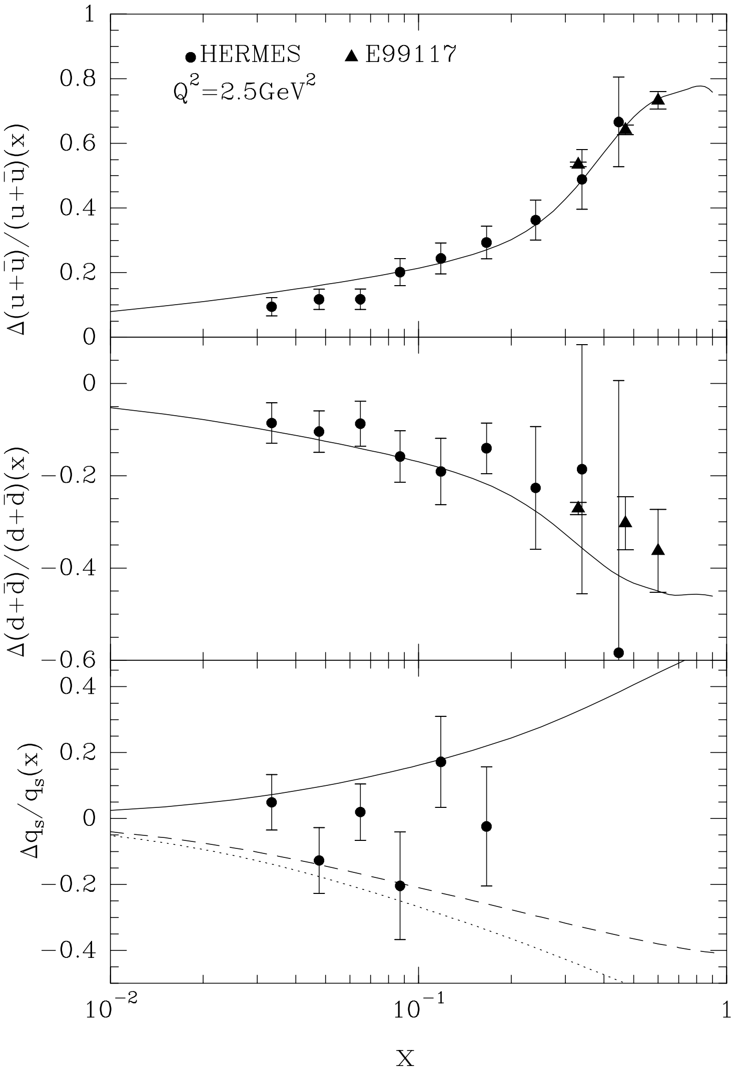

Figure 24: HERMES [44] and E99-117 [54] data on $(\Delta u+\Delta\bar{u})/(u+\bar{u})$, $(\Delta d+\Delta\bar{d})/(d+\bar{d})$, $\Delta q_s/q_s$ as function of x at fixed $Q^2 = 2.5\mathrm{GeV}^2$. The curves are our model calculations. For the sea quarks $\Delta\bar{u}/\bar{u}$ (solid curve) , $\Delta\bar{d}/\bar{d}$ (dashed curve) and $\Delta s/s$ (dotted curve).

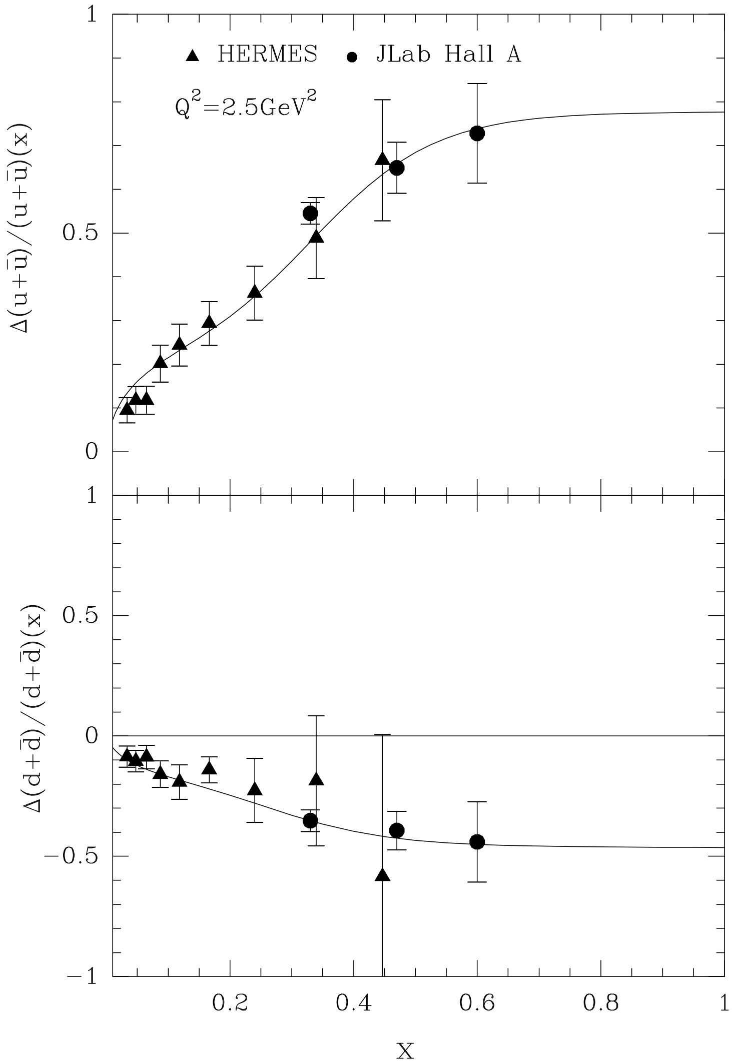

Figure 25: Ratios $(\Delta u + \Delta \bar{u})/(u + \bar{u})$ and $(\Delta d + \Delta \bar{d})/(d + \bar{d})$ as a function of x for $Q^2 = 2.5\text{GeV}^2$. Data from Hermes [44] and JLab experiments [45].

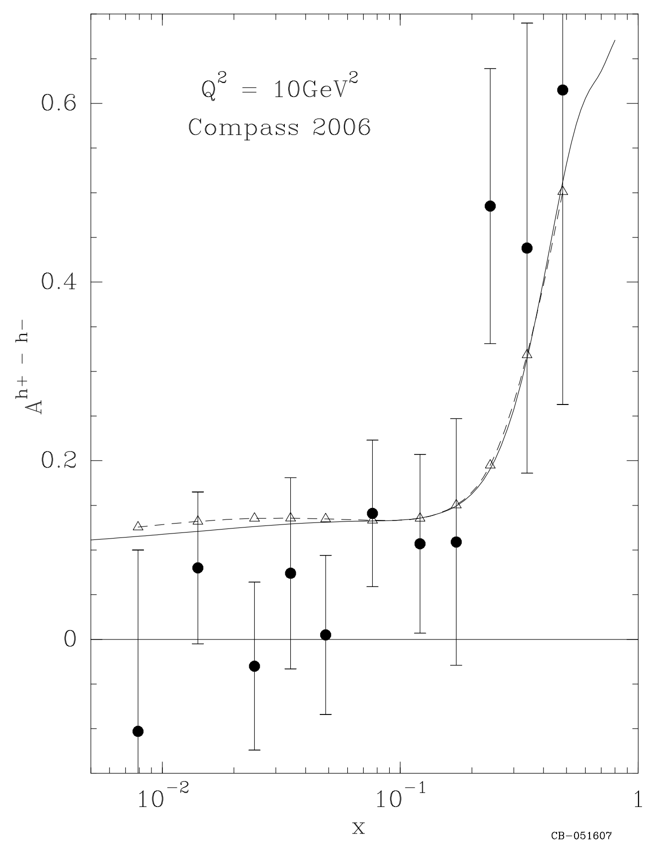

Figure 26: Prediction of BBS PDF for the difference asymmetry $A^{h^+-h^-}$ determined at NLO as a function of x for $Q^2 = 10\mathrm{GeV}^2$, data from Compass Collaboration.

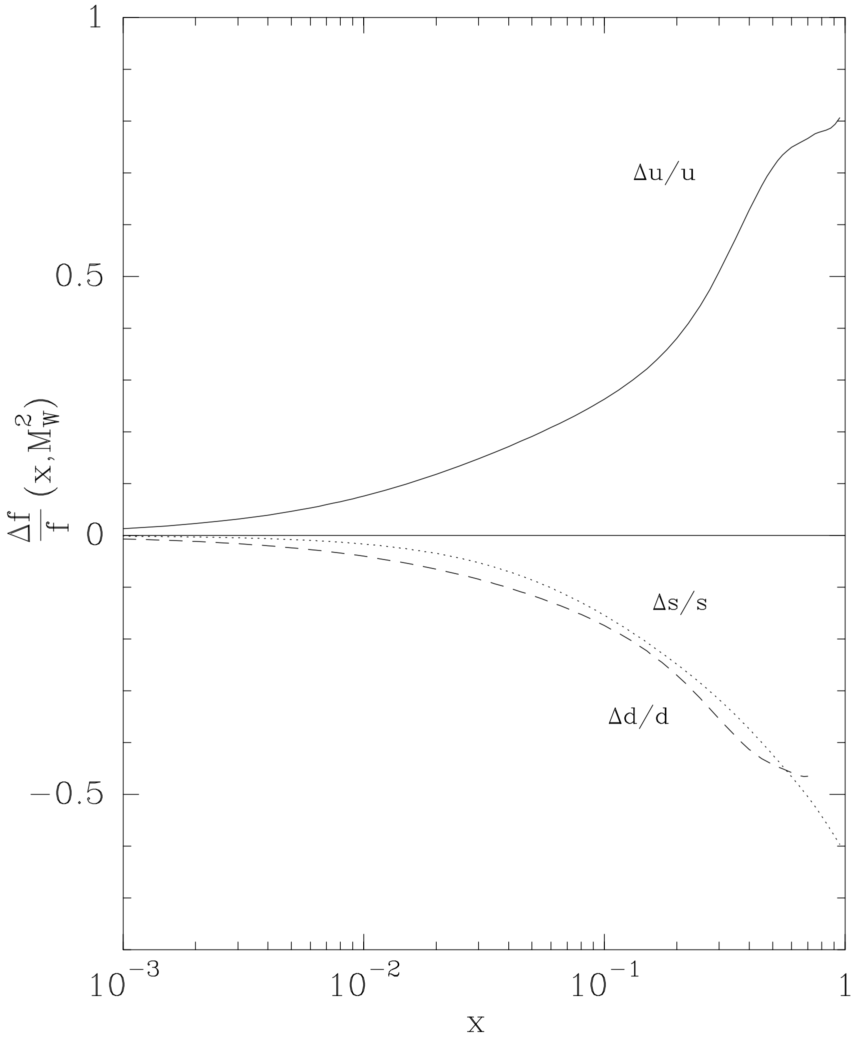

Figure 27: Ratio polarized/unpolarized quark distributions for u, d, s, at $Q^2 = 4\mathrm{GeV}^2$.

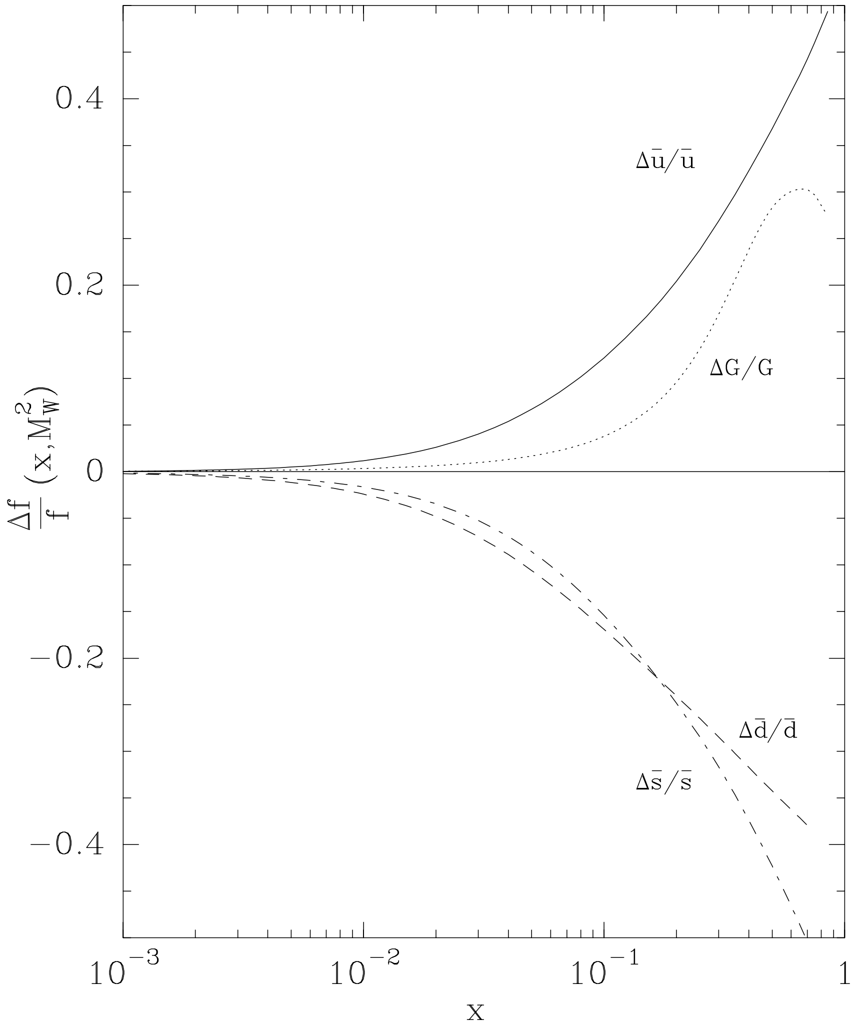

Figure 28: Ratio polarized/unpolarized antiquark distributions for $\bar{u}$, $\bar{d}$, $\bar{s}$ and G, at $Q^2 = 4\text{GeV}^2$.

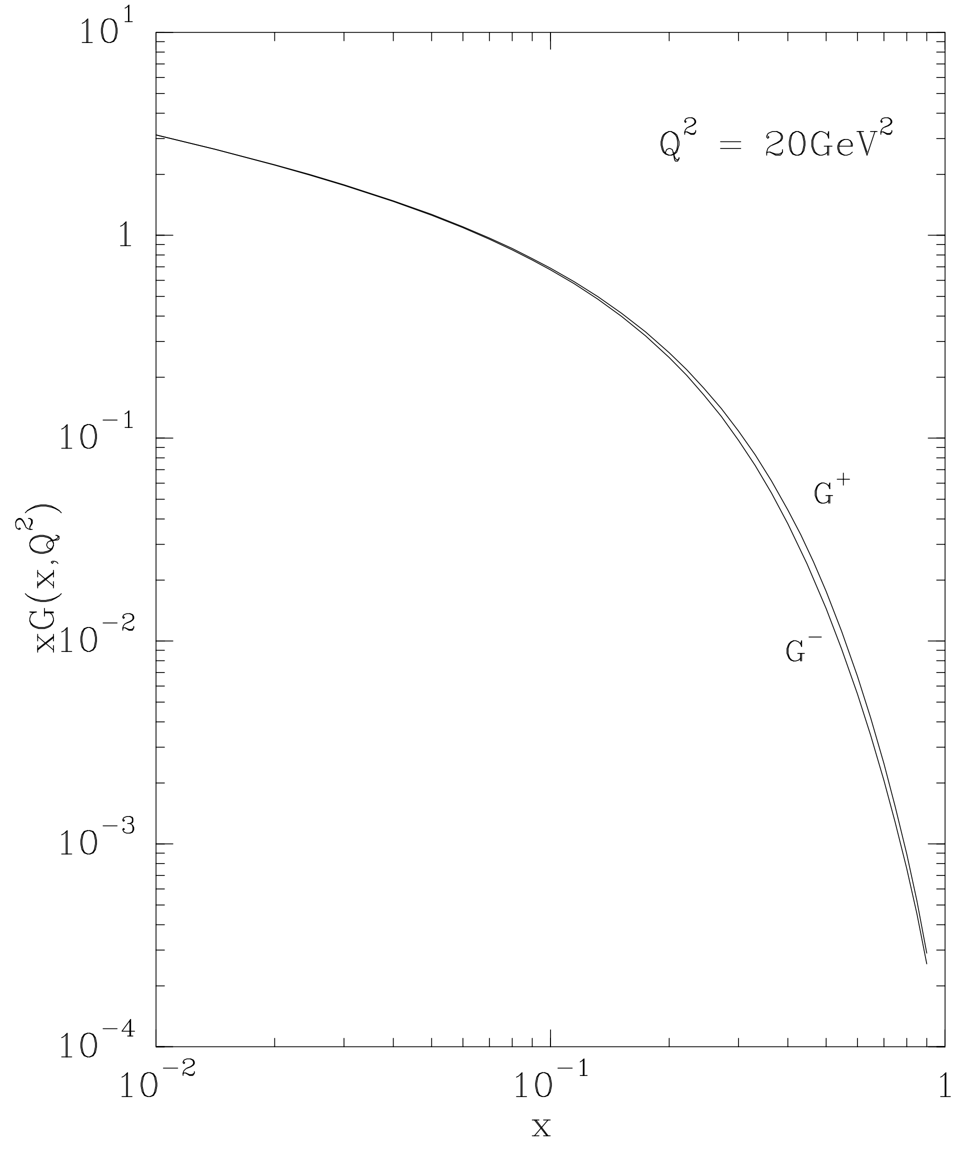

Figure 29: Spin components of gluon density

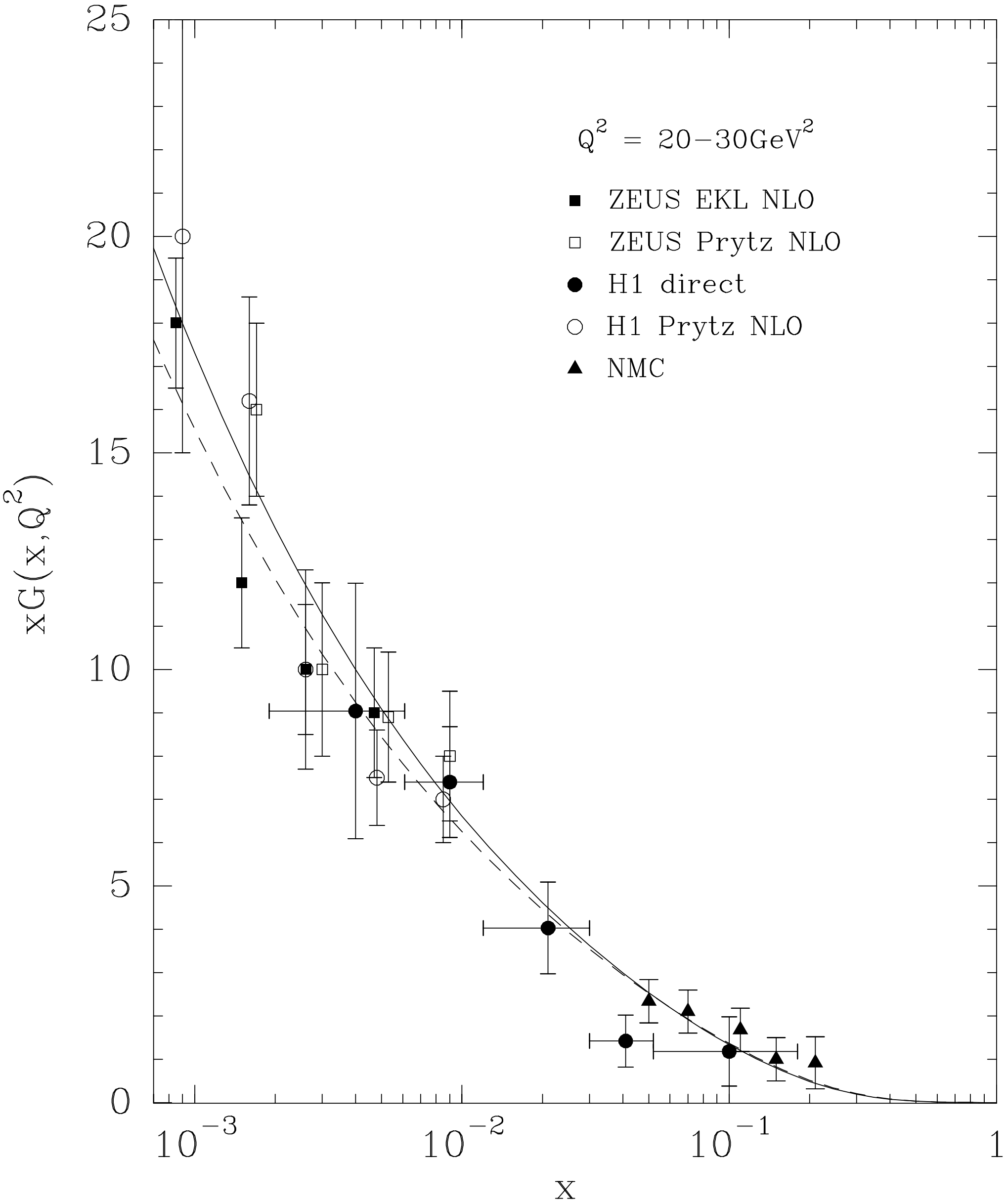

Figure 30: Comparison of $xG(x, Q^2)$ at $Q^2 = 20 - 30\text{GeV}^2$ (dashed-solid) with experimental determination from NMC [57], H1 [39] and ZEUS [91] experiments.

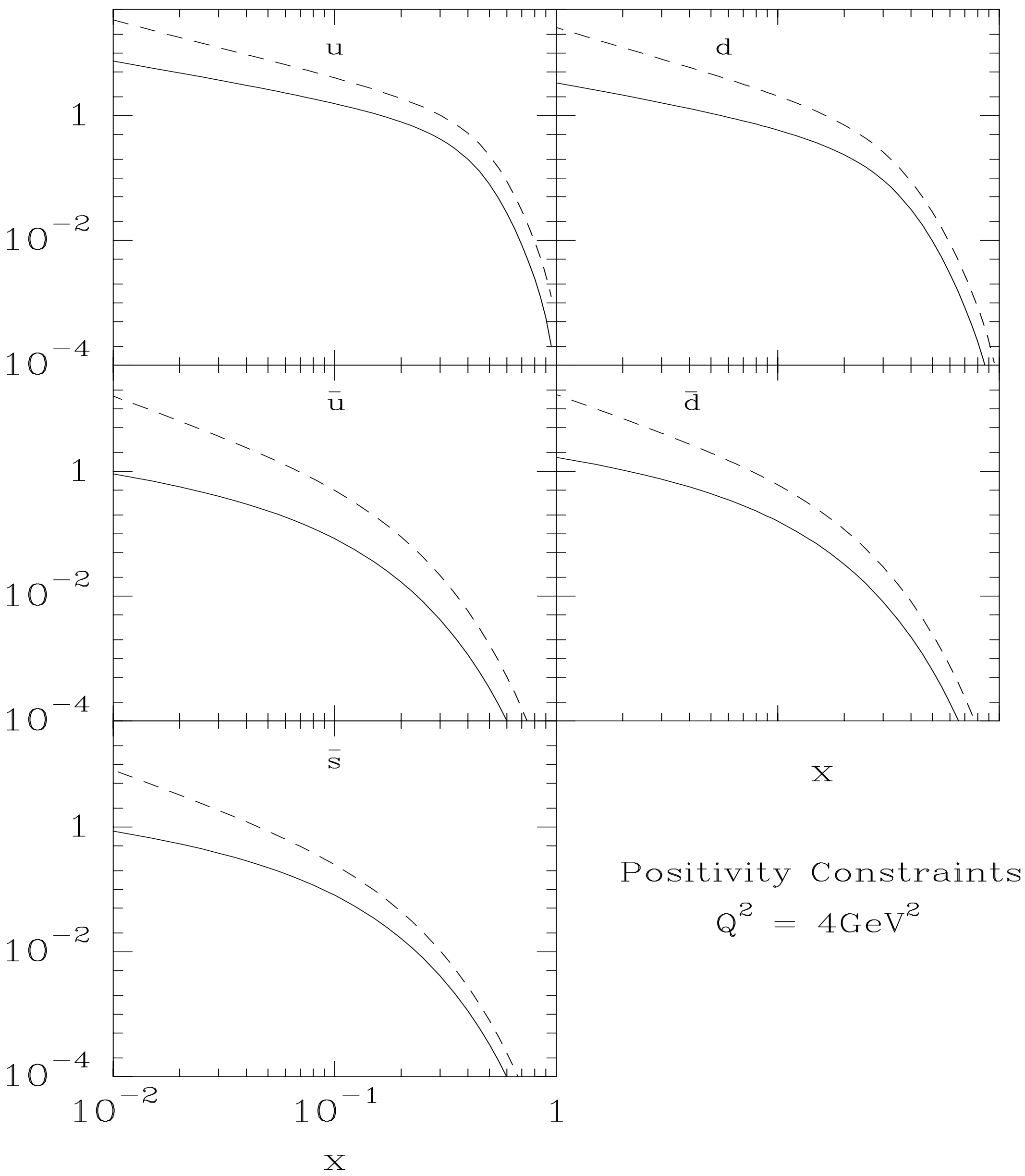

Figure 31: Positivity constraints between polarized and unpolarized distributions according to the inequality of Soffer-Teryaev [98].

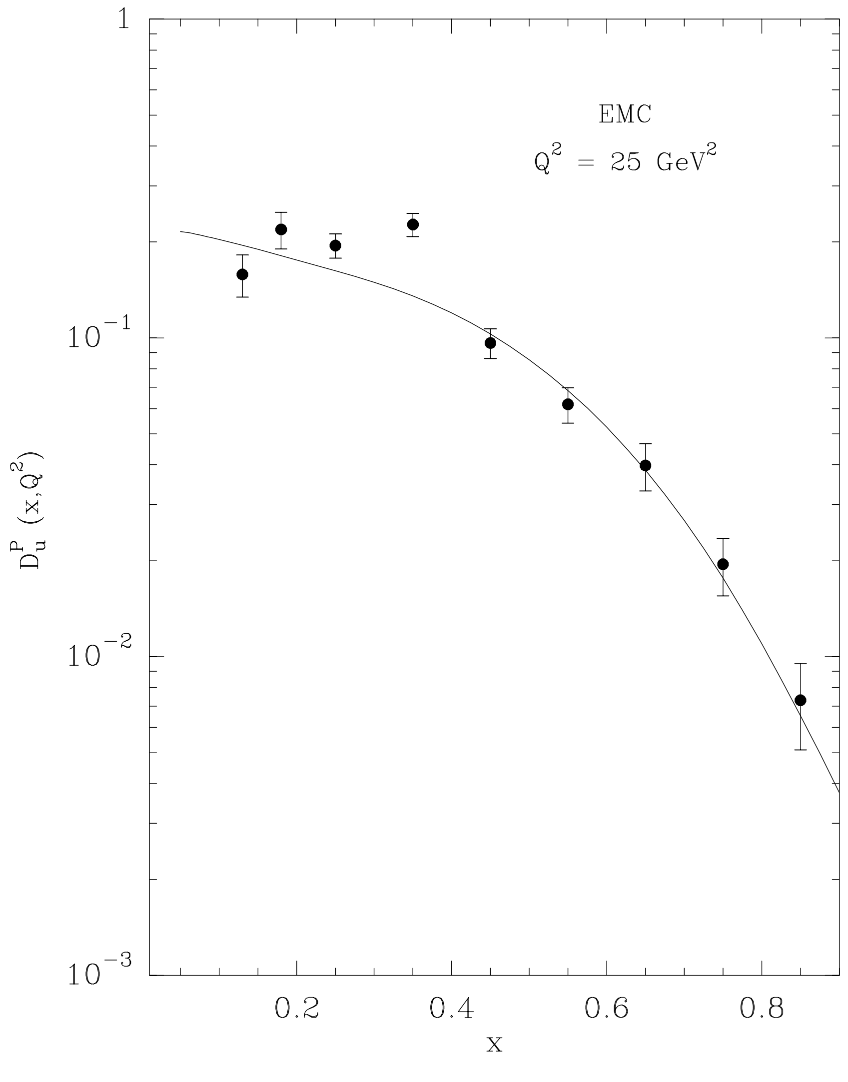

Figure 32: The u quark to proton fragmentation function $D_u^p(x, Q^2)$ as a function of x at $Q^2 = 25\text{GeV}^2$. The experimental data are from Ref. [36].

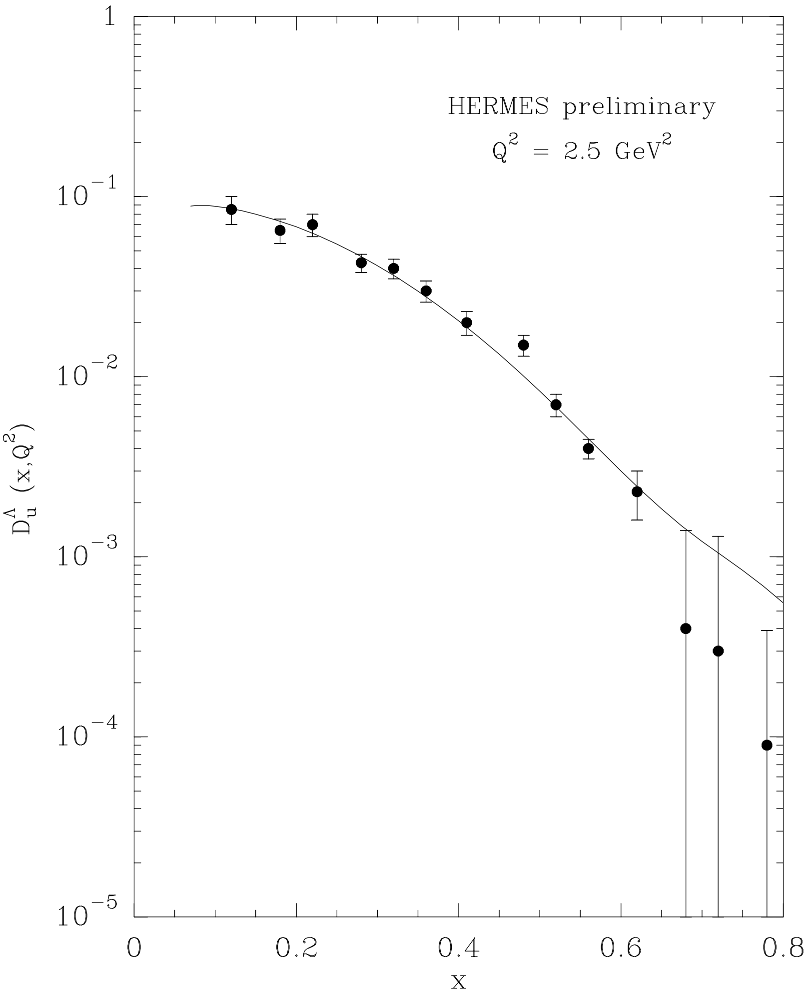

Figure 33: The fragmentation function for u quark to Λ, $D_u^\Lambda(x, Q^2)$, as a function of x at $Q^2 = 2.5\text{GeV}^2$. The experimental data are from Ref. [43].

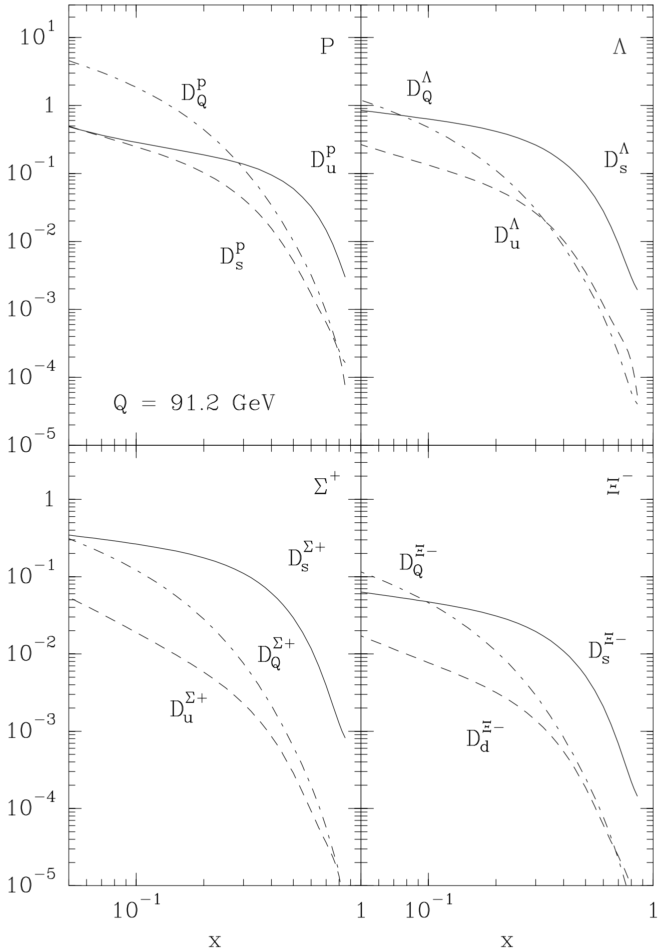

Figure 34: The quark to octet baryons fragmentation functions $D_q^B(x, Q^2)$ and $D_Q^B(x, Q^2)$ ($B = p, \Lambda, \Sigma^{\pm}, \Xi^-$, $q = u, d, s$ and $Q = c, b, t$), as a function of x at $Q = 91.2$GeV. Note that we used different vertical scales in the upper and lower parts of the figure.

4 Unpolarized experiments

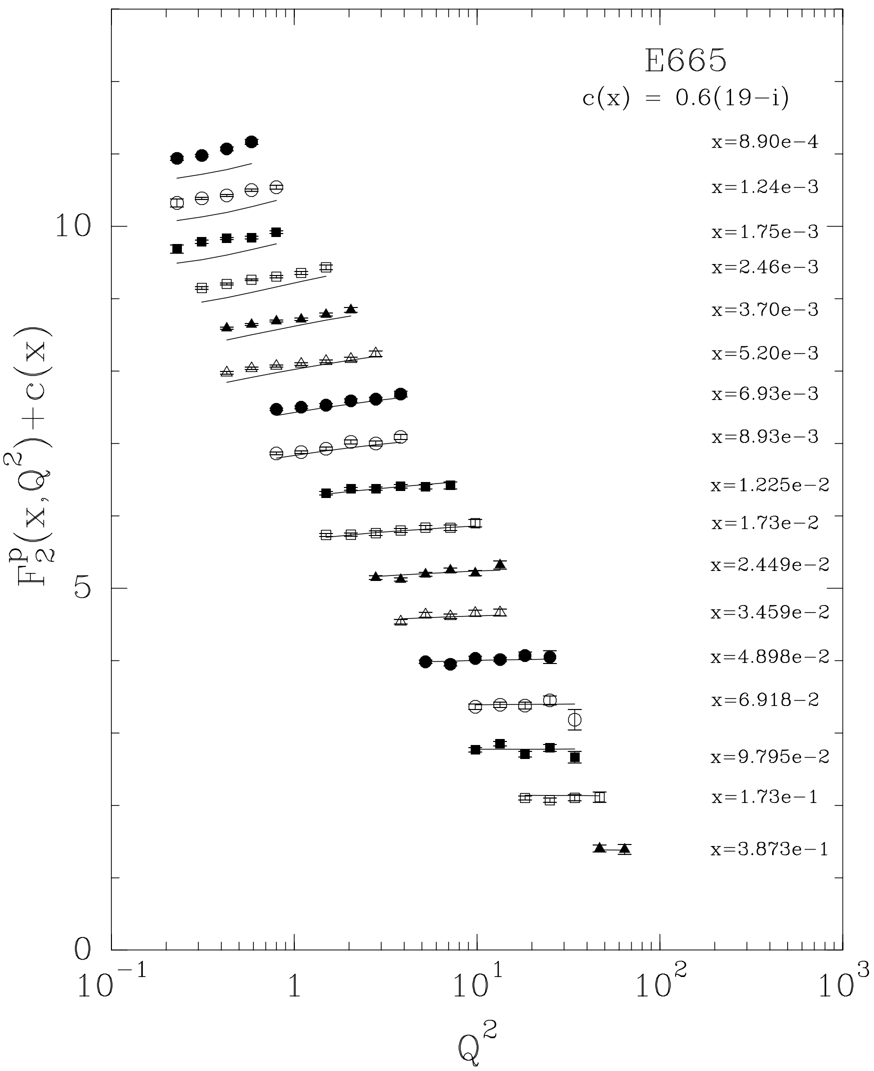

Figure 35: $F_2^p(x, Q^2)$ as function of Q^2 for fixed x, E665 data [23]. The function $c(x_i) = 0.6(19 - i)$, $i = 1$ corresponds to $x = 8.9\ 10^{-4}$.

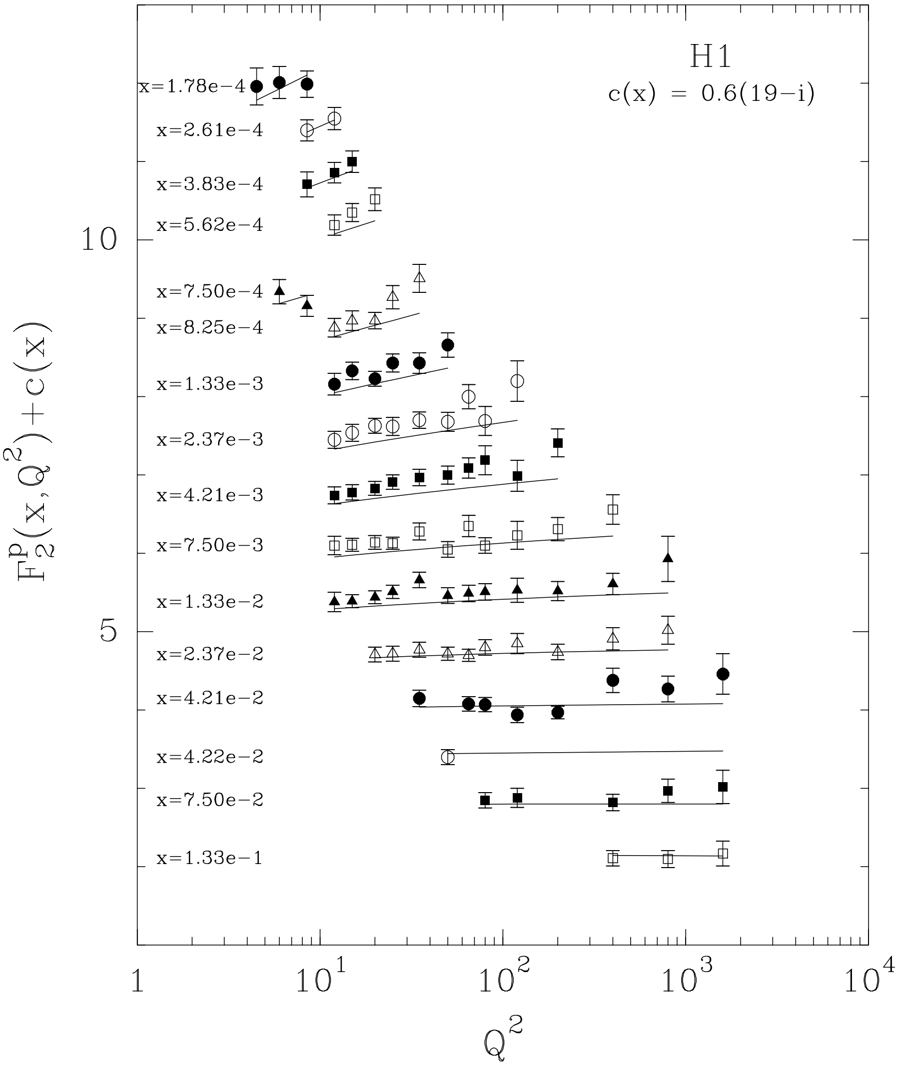

Figure 36: $F_2^p(x, Q^2)$ as function of Q^2 for fixed x, H1 data [37, 38]. The function $c(x_i) = 0.6(19 - i)$, $i = 1$ corresponds to $x = 1.78\ 10^{-4}$.

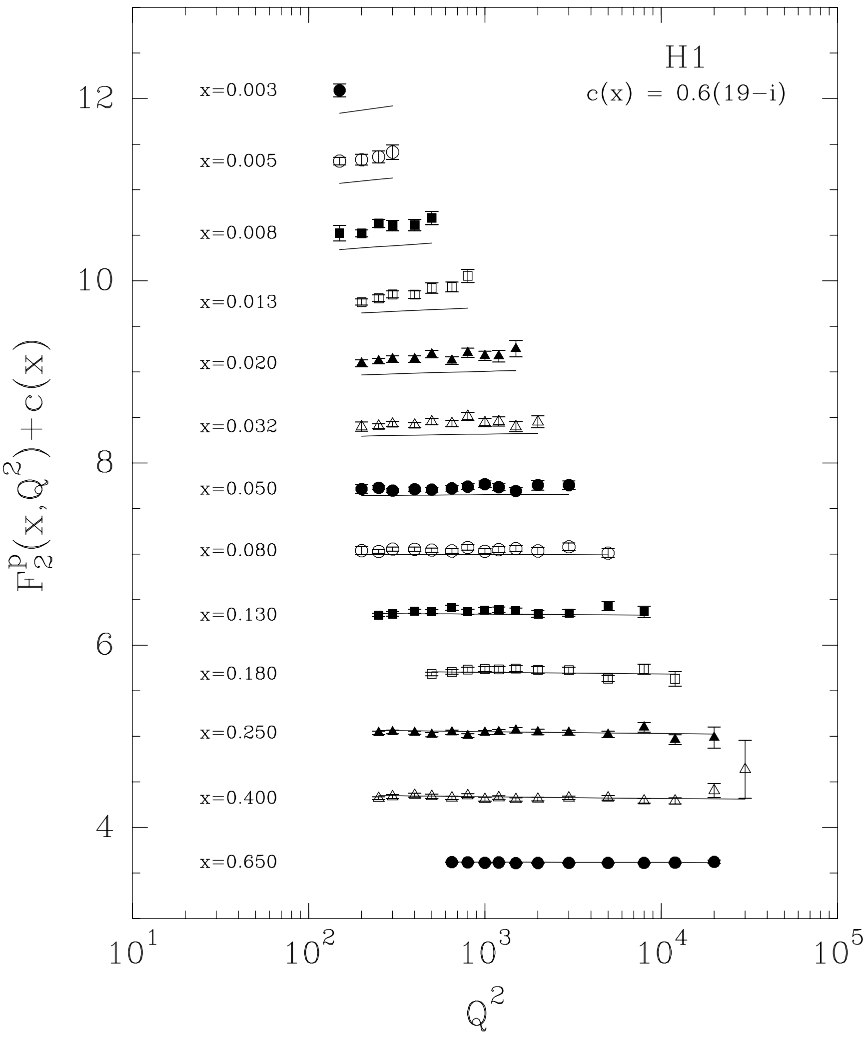

Figure 37: $F_2^p(x, Q^2)$ as function of Q^2 for fixed x, H1 Coll. The function $c(x_i) = 0.6(19 - i)$, $i = 1$ corresponds to $x = 0.003$.

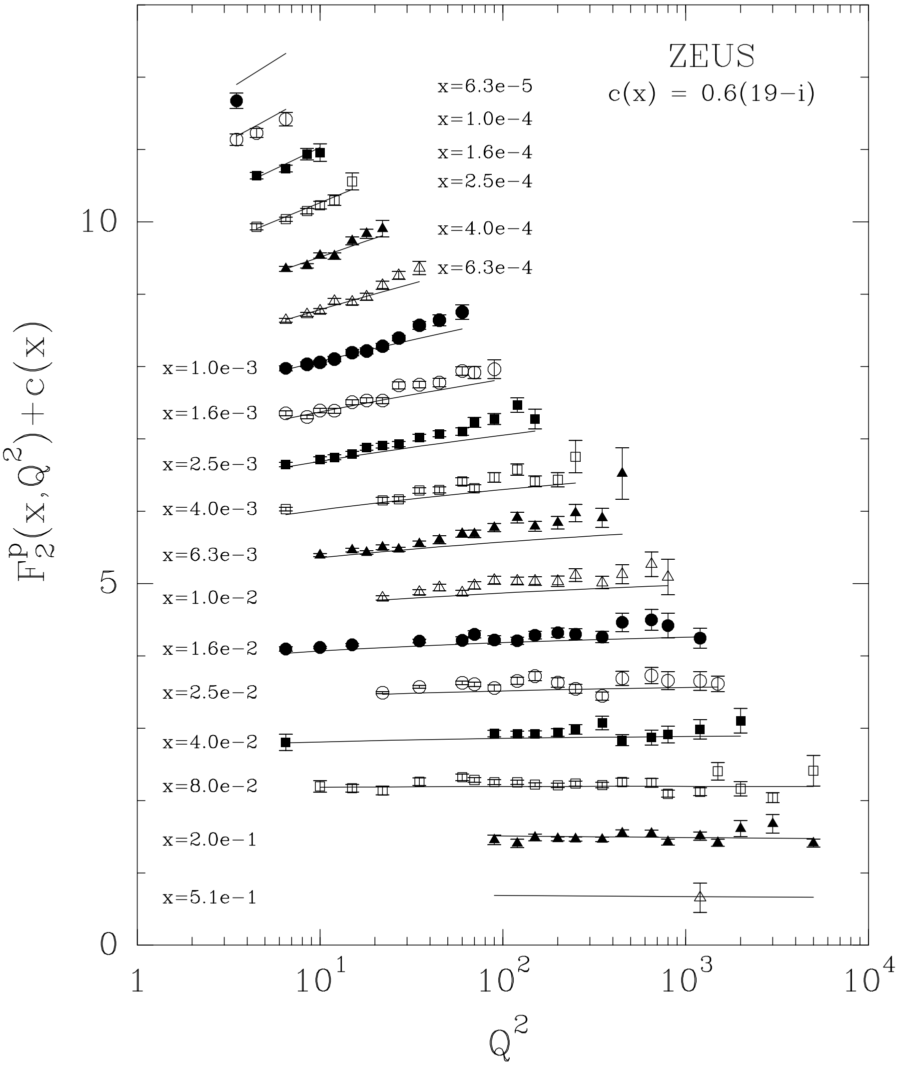

Figure 38: $F_2^p(x,Q^2)$ as function of Q^2 for fixed x, ZEUS data [92, 93]. The function $c(x_i) = 0.6(19-i)$, $i = 1$ corresponds to $x = 6.3\ 10^{-5}$.

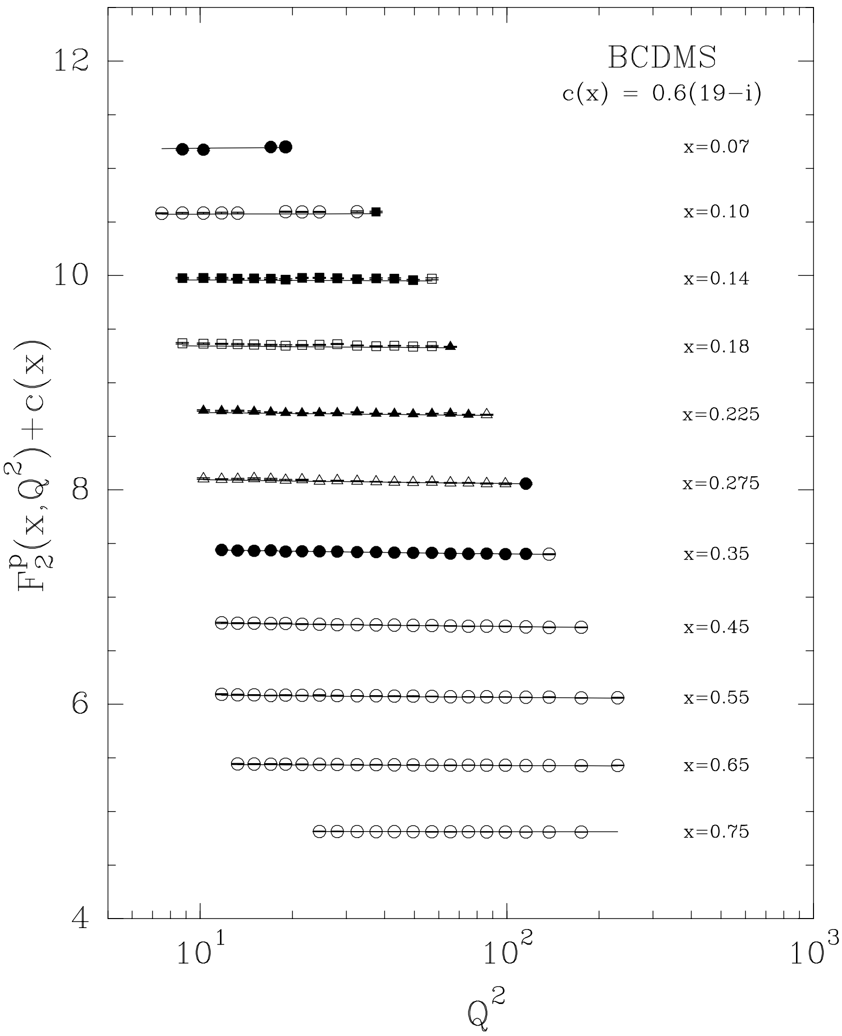

Figure 39: $F_2^p(x, Q^2)$ as function of Q^2 for fixed x, BCDMS Coll. [11, 12]. The function $c(x_i) = 0.6(19 - i)$, $i = 1$ corresponds to $x = 0.07$

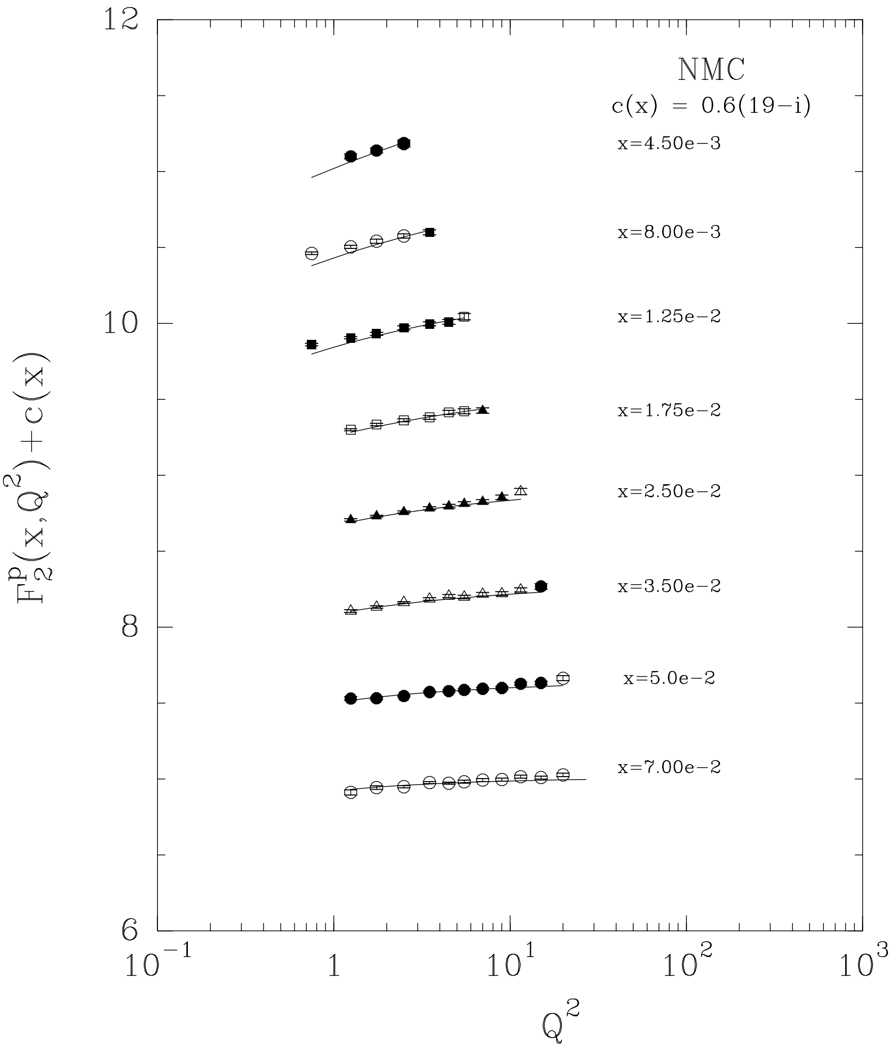

Figure 40: $F_2^p(x, Q^2)$ as function of Q^2 for fixed x, NMC Coll. The function $c(x_i) = 0.6(19 - i)$, $i = 1$ corresponds to $x = 4.5\ 10^{-3}$.

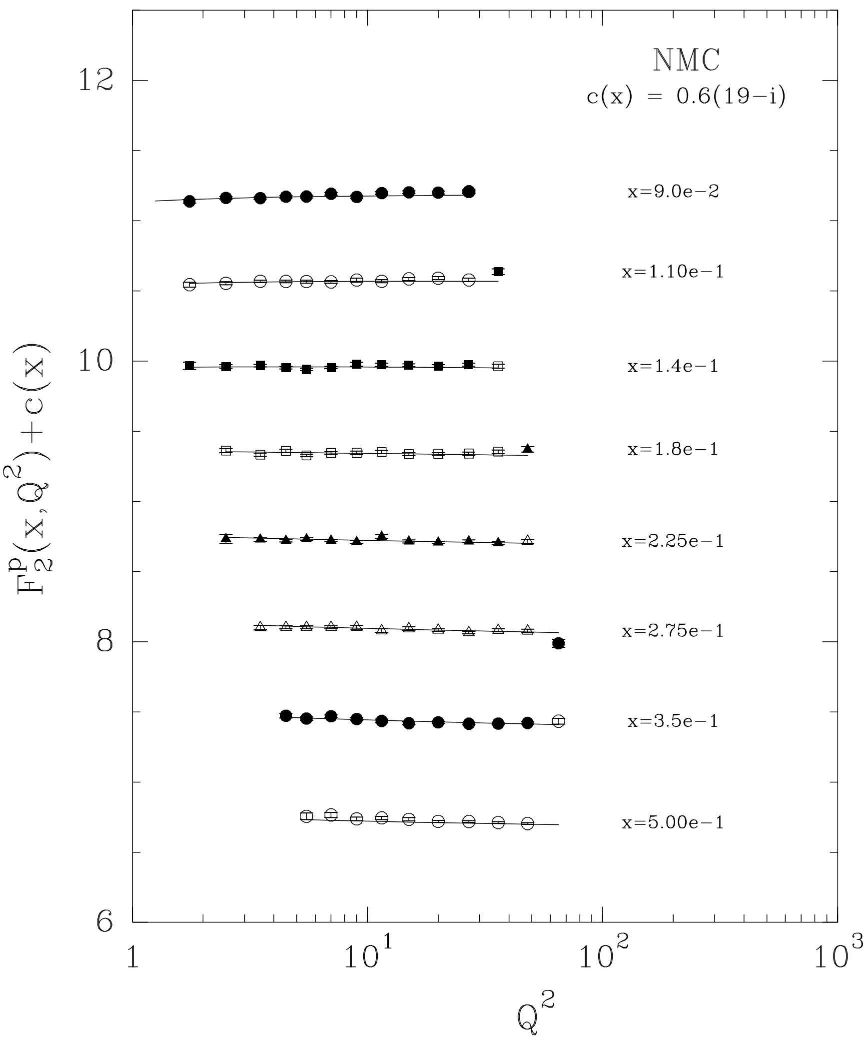

Figure 41: $F_2^p(x, Q^2)$ as function of Q^2 for fixed x, NMC Coll. The function $c(x_i) = 0.6(19 - i)$, $i = 1$ corresponds to $x = 9\ 10^{-2}$.

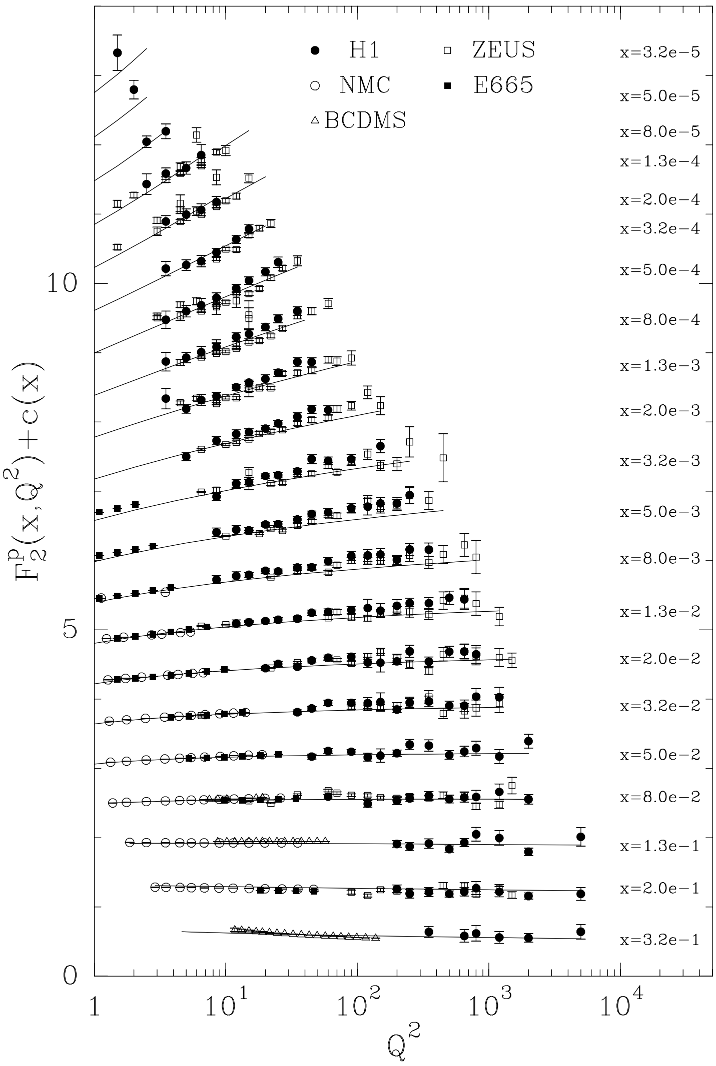

Figure 42: $F_2^p(x, Q^2)$ as function of Q^2 for fixed x, $c(x) = 0.6(i_x - 0.4)$, $i_x = 1 \rightarrow x = 0.32$, rebinned data H1, ZEUS, E665, NMC, BCDMS. (Presentation of data, courtesy of R. Voss).

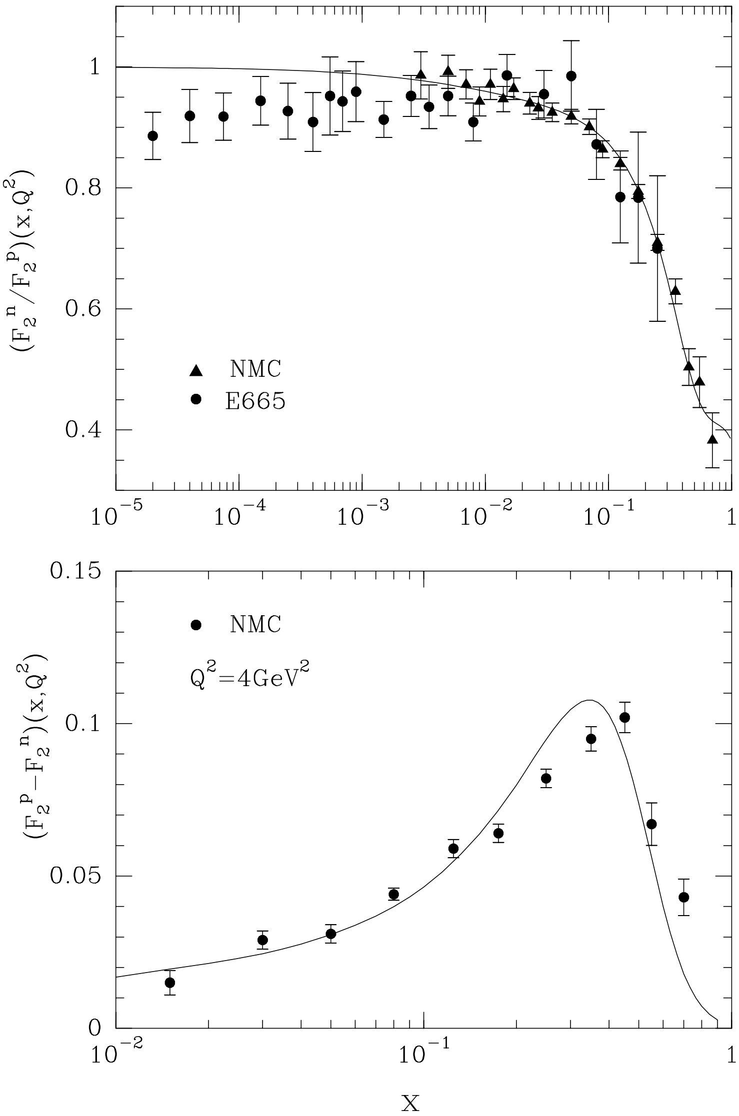

Figure 43: Ratio F_2^n/F_2^p as a function of x for differents Q^2 values, data are from NMC and E665 Coll. Difference $F_2^p - F_2^n$ as a function of x for $Q^2 = 4\mathrm{GeV}^2$, data are from NMC Coll.. The curves are shown for $Q^2 = 4\mathrm{GeV}^2$.

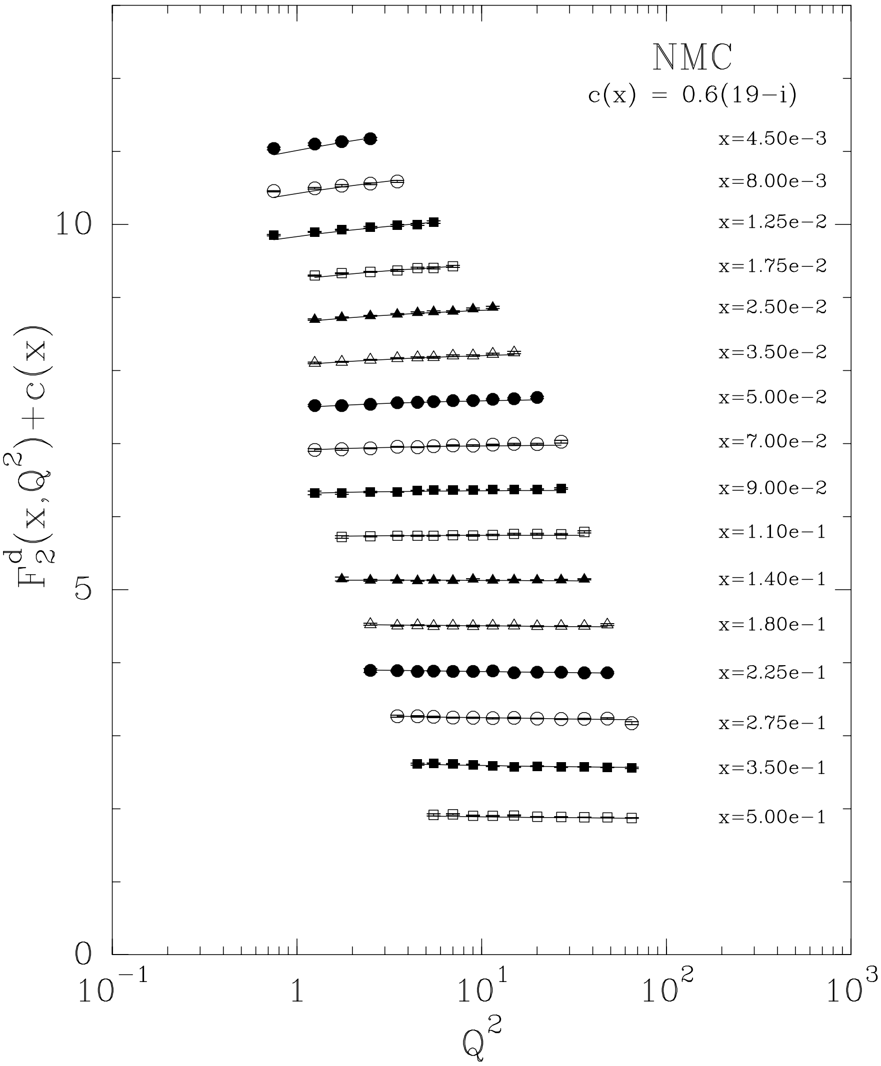

Figure 44: $F_2^d(x,Q^2)$ as function of Q^2 for fixed x, NMC data [58]. The function $c(x_i) = 0.6(19-i)$, $i=1$ corresponds to $x = 4.5\ 10^{-3}$.

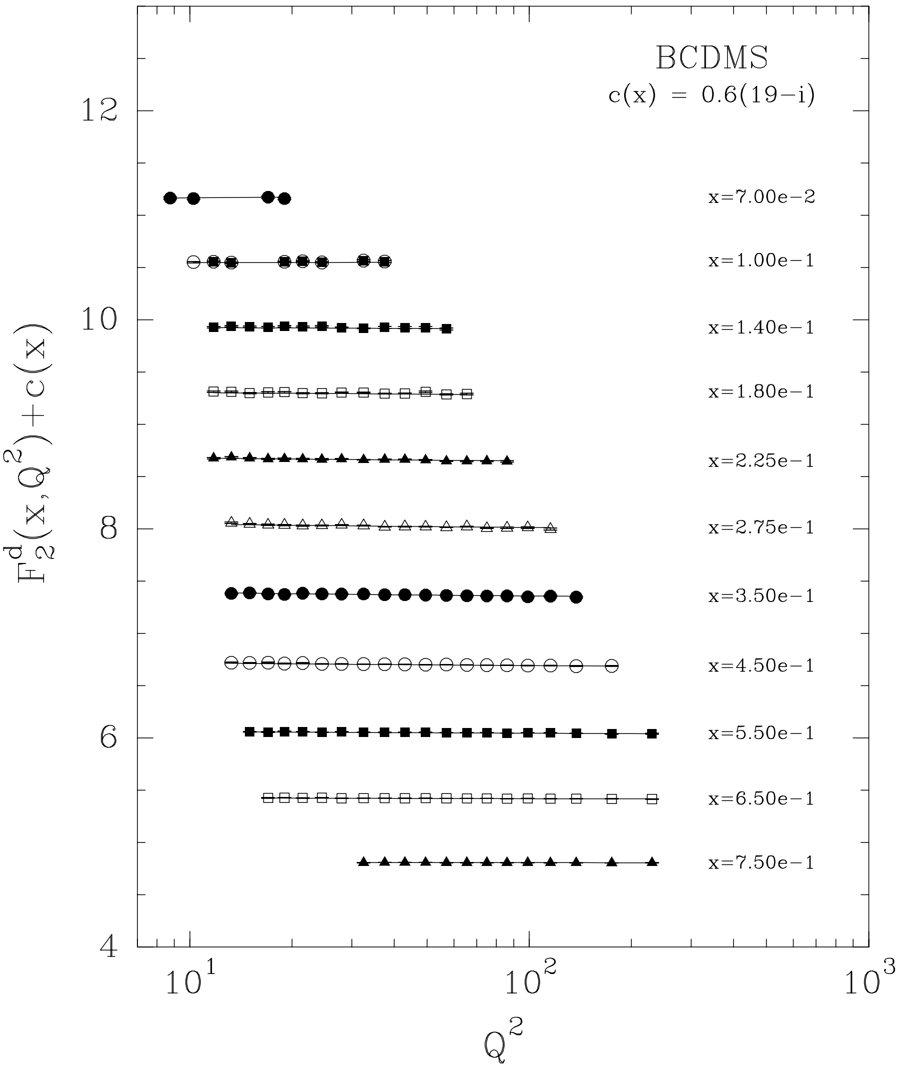

Figure 45: $F_2^d(x, Q^2)$ as function of Q^2 for fixed x, BCDMS data [12]. The function $c(x_i) = 0.6(19 - i)$, $i = 1$ corresponds to $x = 7\ 10^{-2}$.

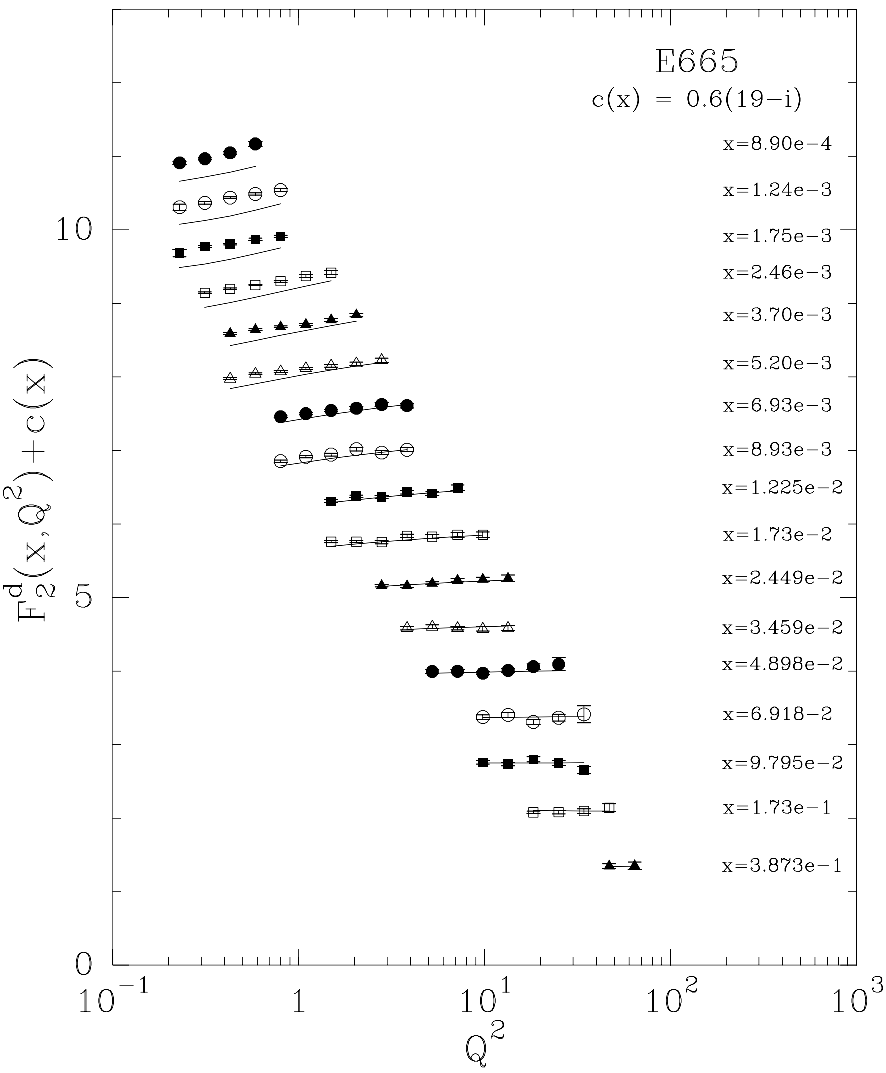

Figure 46: $F_2^d(x, Q^2)$ as function of Q^2 for fixed x, E665 data [23]. The function $c(x_i) = 0.6(19 - i)$, $i = 1$ corresponds to $x = 8.9\ 10^{-4}$.

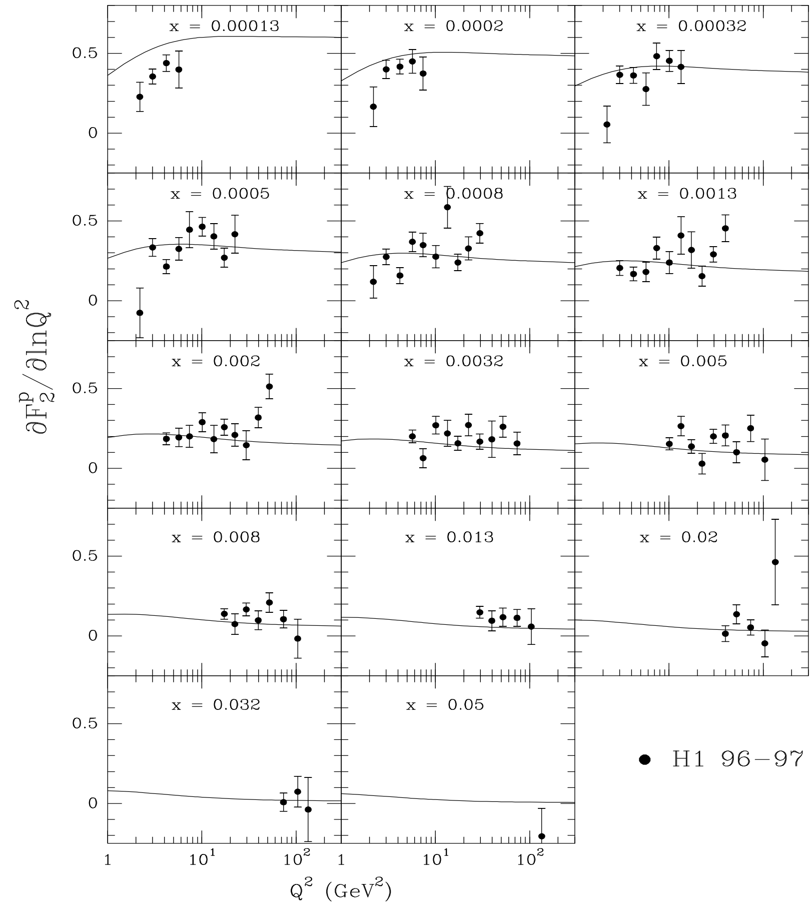

Figure 47: Prediction of the partial derivative $\partial F_2^p(x, Q^2)/\partial \ln(Q^2)$ for fixed x as a function of Q^2. Data from H1 Collaboration [111].

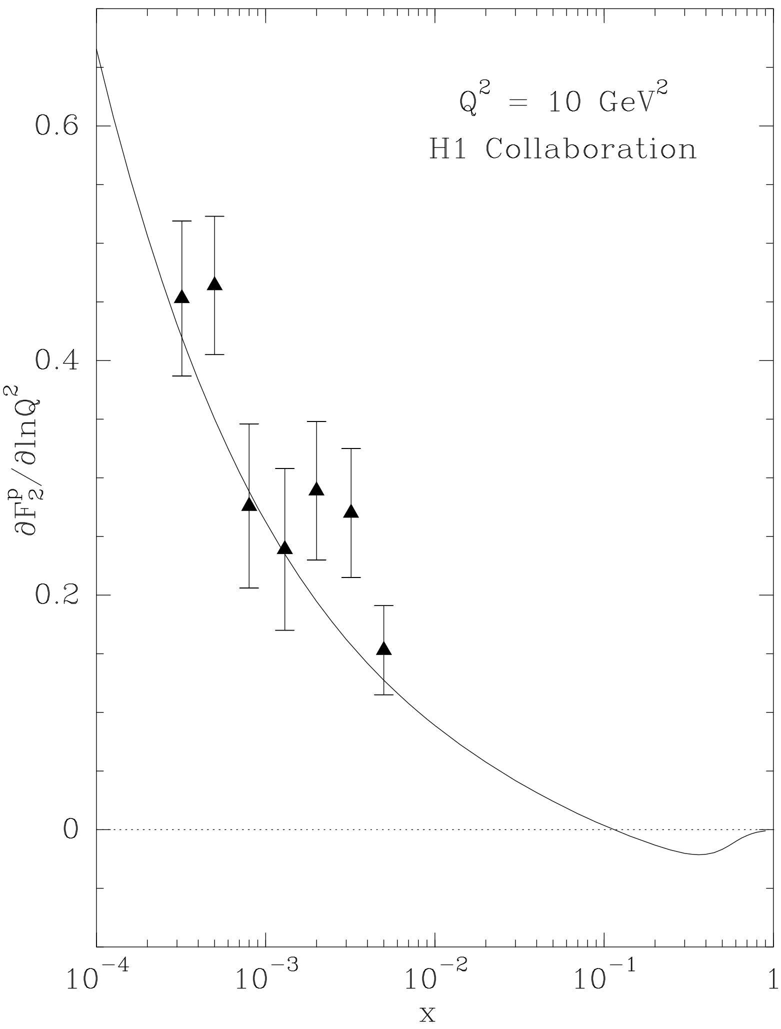

Figure 48: Prediction of the partial derivative $\partial F_2^p(x, Q^2)/\partial \ln(Q^2)$ for $Q^2 = 10\mathrm{GeV}^2$ as a function of x. Data from H1 Collaboration [111].

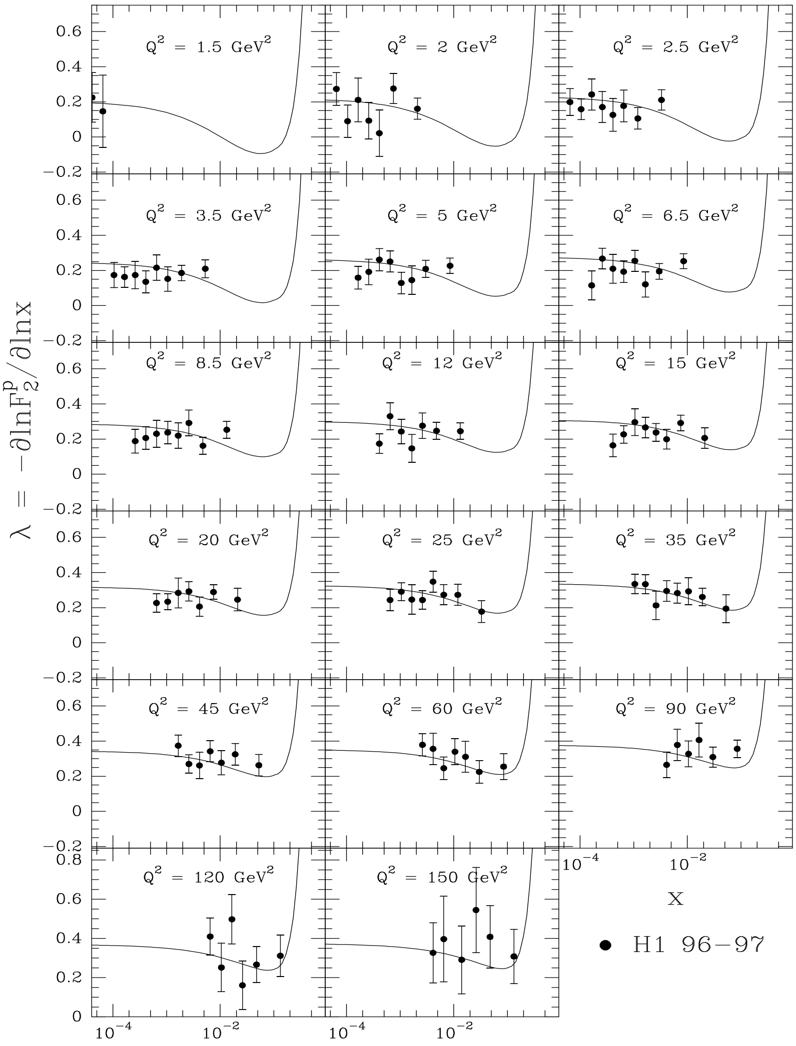

Figure 49: Prediction of the partial derivative $-\partial \ln F_2^p(x, Q^2)/\partial \ln(x)$ for fixed Q^2 as a function of x. Data from H1 Collaboration [112].

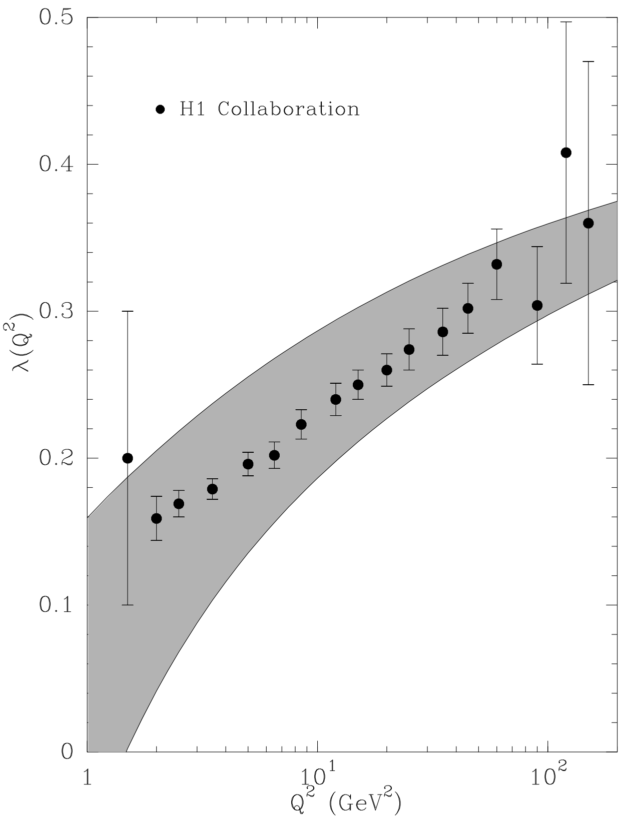

Figure 50: F_2^p partial derivative $\lambda(x, Q^2)$ as a function of Q^2, the shaded surface represents the allowed domain for $10^{-4} \leq x \leq 10^{-2}$, predicted by the statistical model. Data from H1 Collaboration [112].

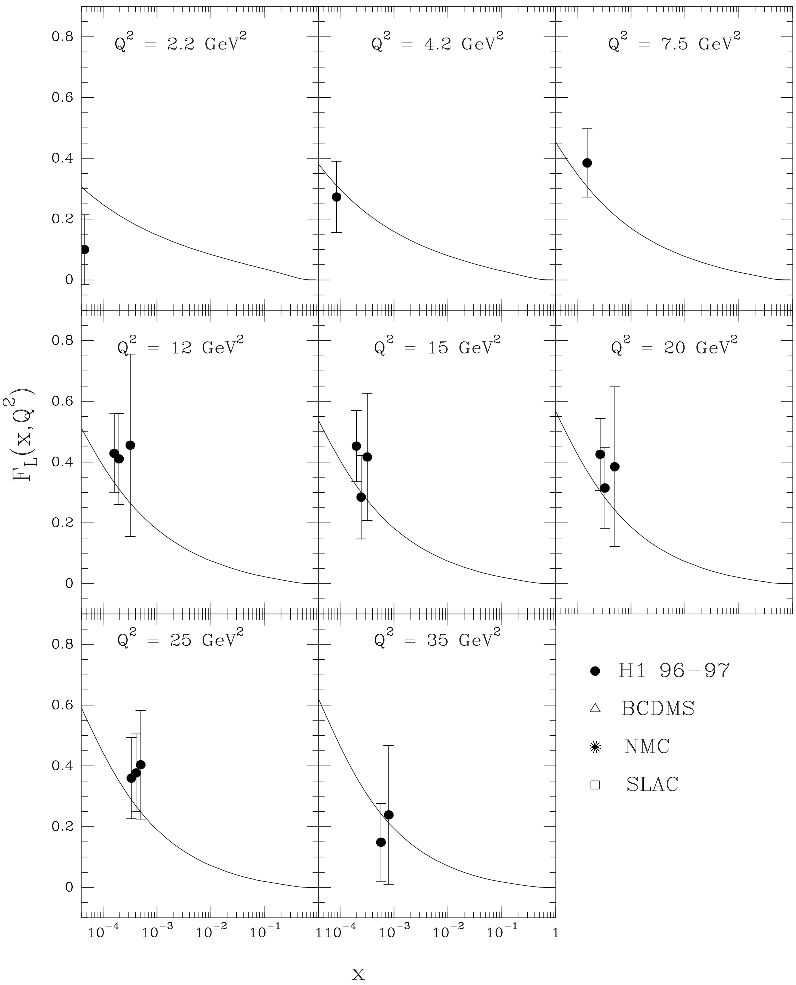

Figure 51: Prediction of the structure function F_L for different Q^2 as a function of x. Data from H1 Collaboration [111].

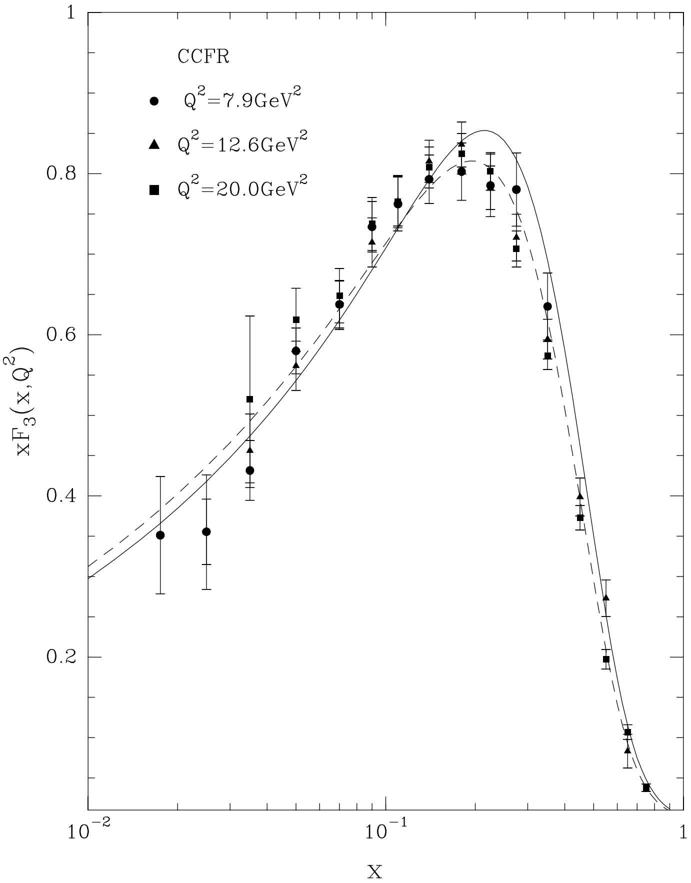

Figure 52: $xF_3^{\nu N}(x, Q^2)$ as function of x for low Q^2 values, CCFR Coll. The curves are for $Q^2 = 4, 12.6\text{GeV}^2$, solid, dashed respectively.

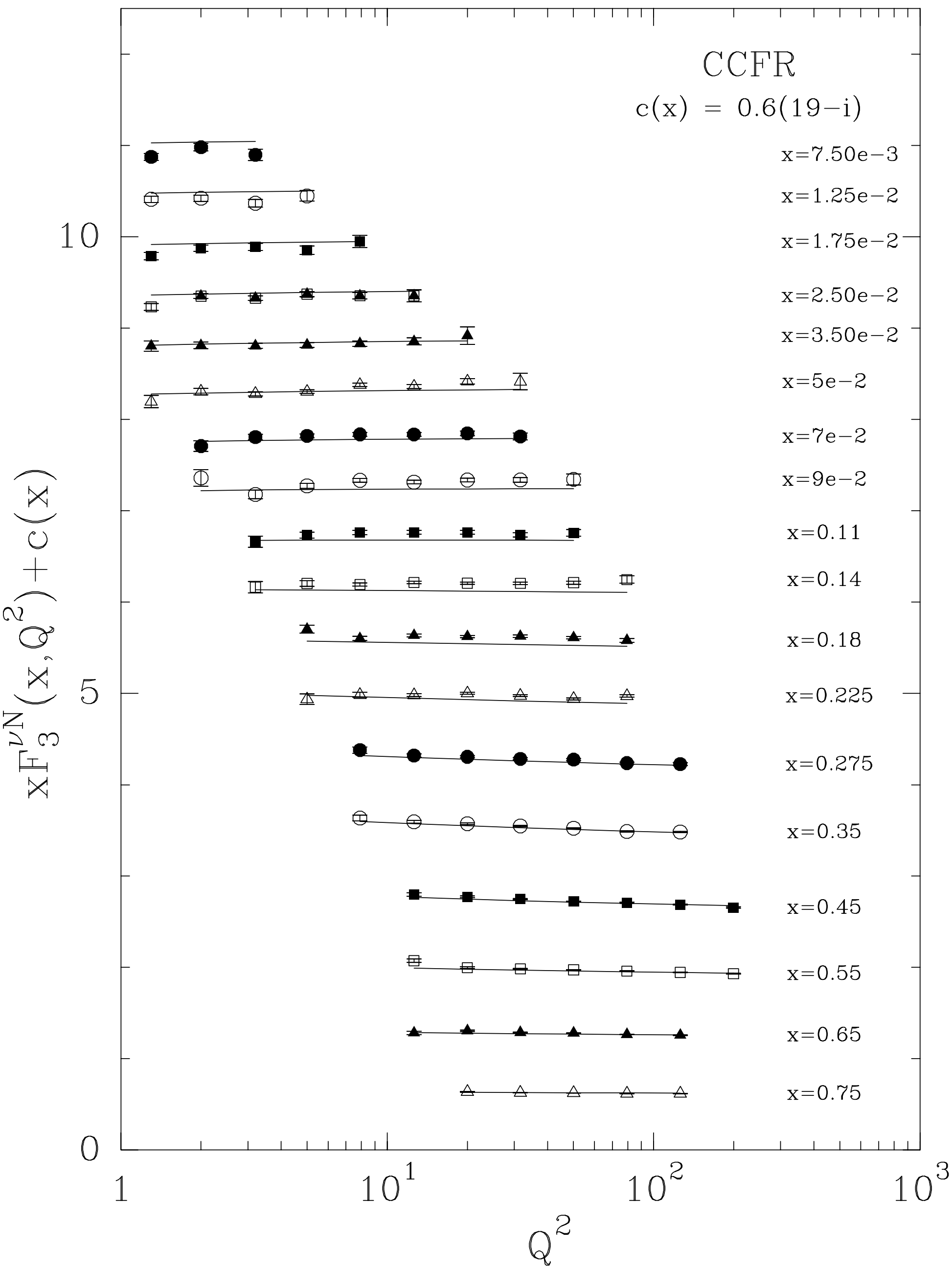

Figure 53: $xF_3^{\nu N}(x,Q^2)$ as function of Q^2 for fixed x, CCFR data [13]. The function $c(x_i) = 0.6(19 - i)$, $i = 1$ corresponds to $x = 7.5\ 10^{-3}$.

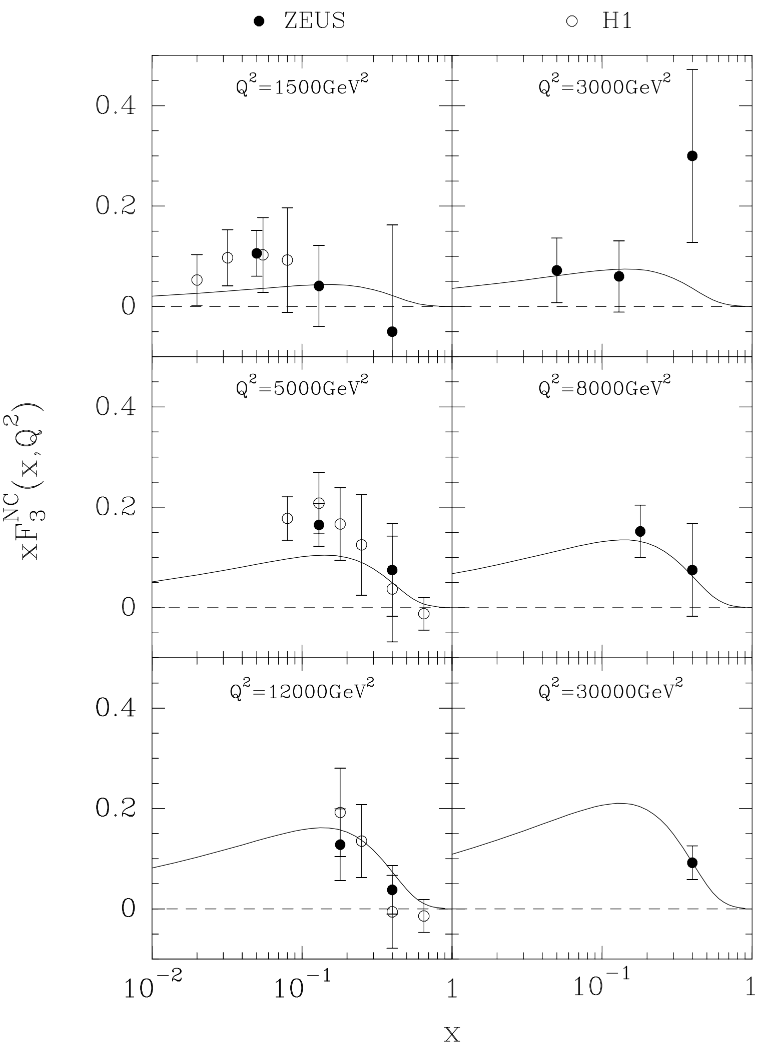

Figure 54: The structure function xF_3^{NC} as a function of x, for different Q^2. Data from ZEUS Coll. [95], H1 Coll. [40].

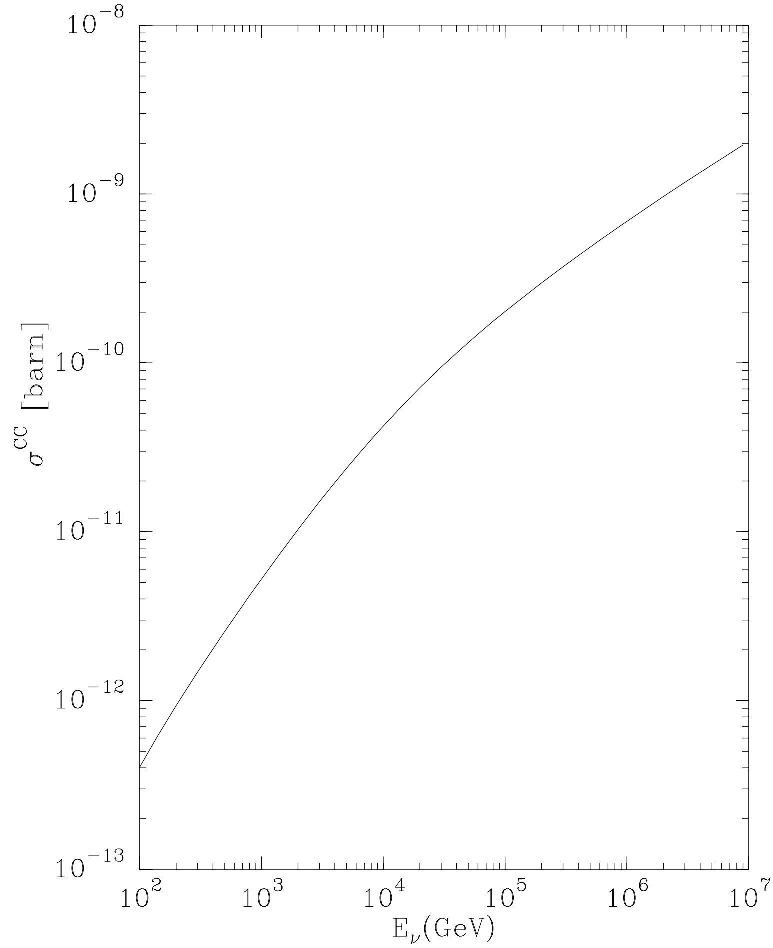

Figure 55: Charged-current total cross section νN for an isoscalar nucleon as a function of the neutrino energy.

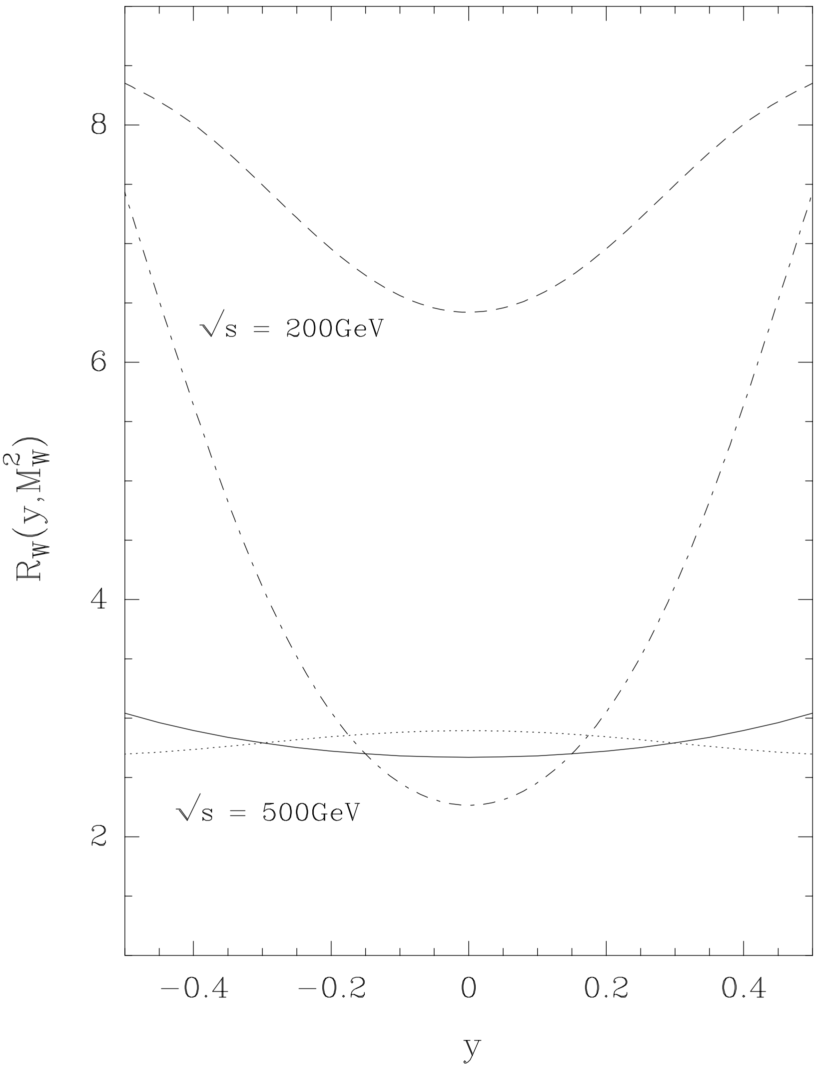

Figure 56: Theoretical calculations for the ratio $R_W(y) = (d\sigma^{W^+}/dy)$ $/(d\sigma^{W^-}/dy)$ for pp versus the W rapidity, at two RHIC-BNL energies. Solid curve ($\sqrt{s} = 500$GeV) and dashed curve ($\sqrt{s} = 200$GeV) are the statistical model predictions. Dotted curve ($\sqrt{s} = 500$GeV) and dashed-dotted curve ($\sqrt{s} = 200$GeV) are the predictions obtained using the $\bar{d}(x)/\bar{u}(x)$ ratio from Ref. [84].

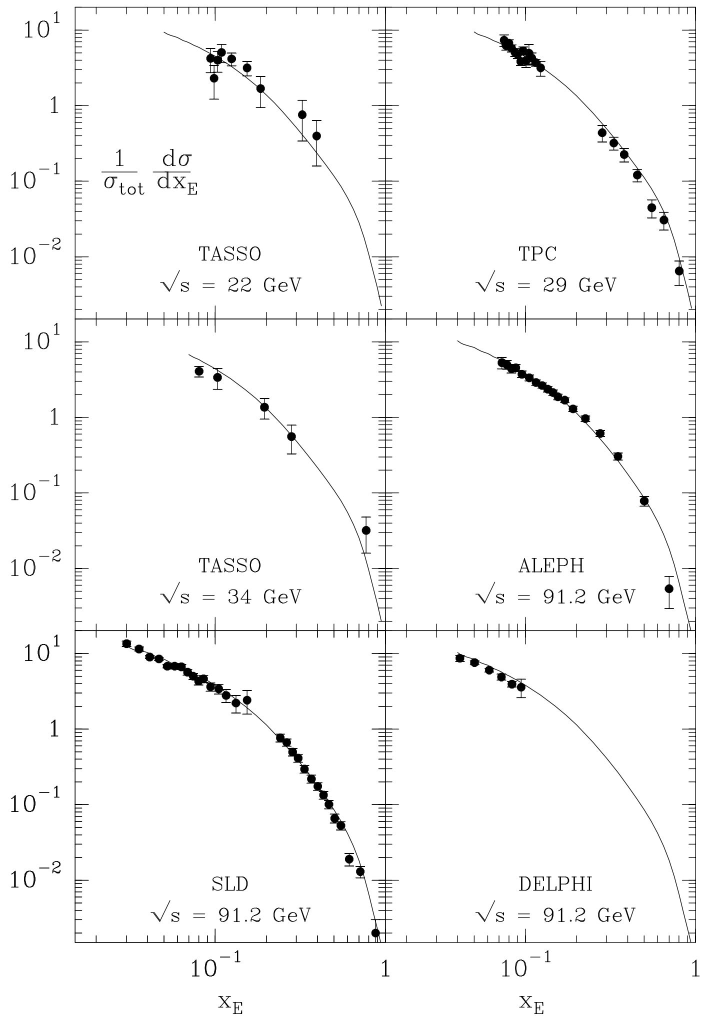

Figure 57: Cross sections for proton production in e^+e^- annihilation at several energies as function of x_E. The experimental data are from Refs. [8, 20, 79, 86, 90, 88].

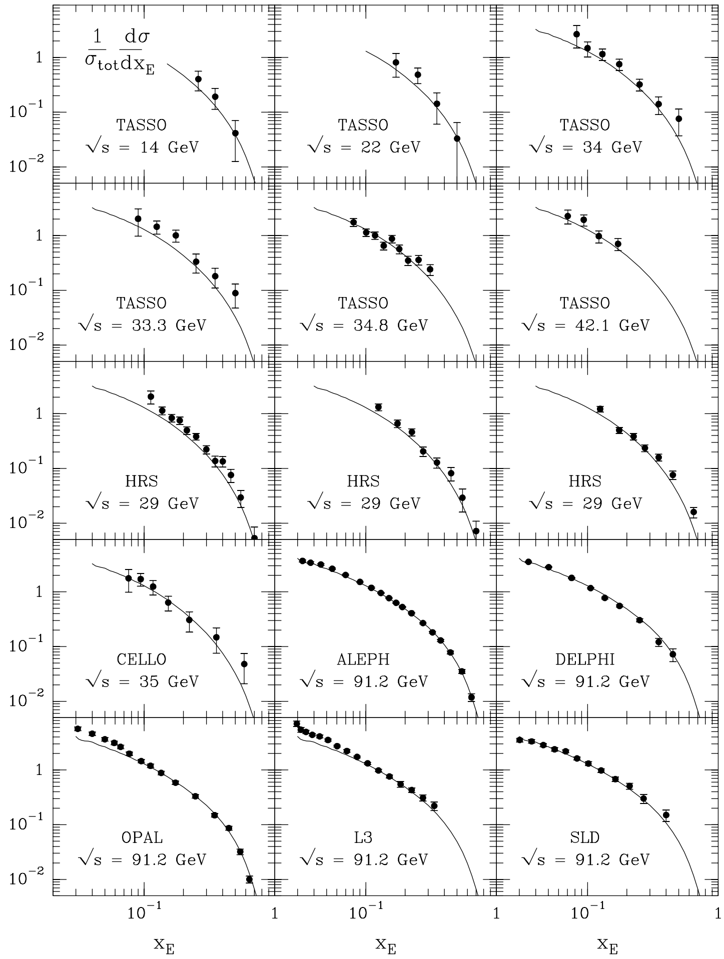

Figure 58: Cross sections for Λ production in e^+e^- annihilation at several energies, as function of x_E. The experimental data are from Refs. [15, 9, 21, 61, 55, 79, 85, 87, 89, 50, 51, 52].

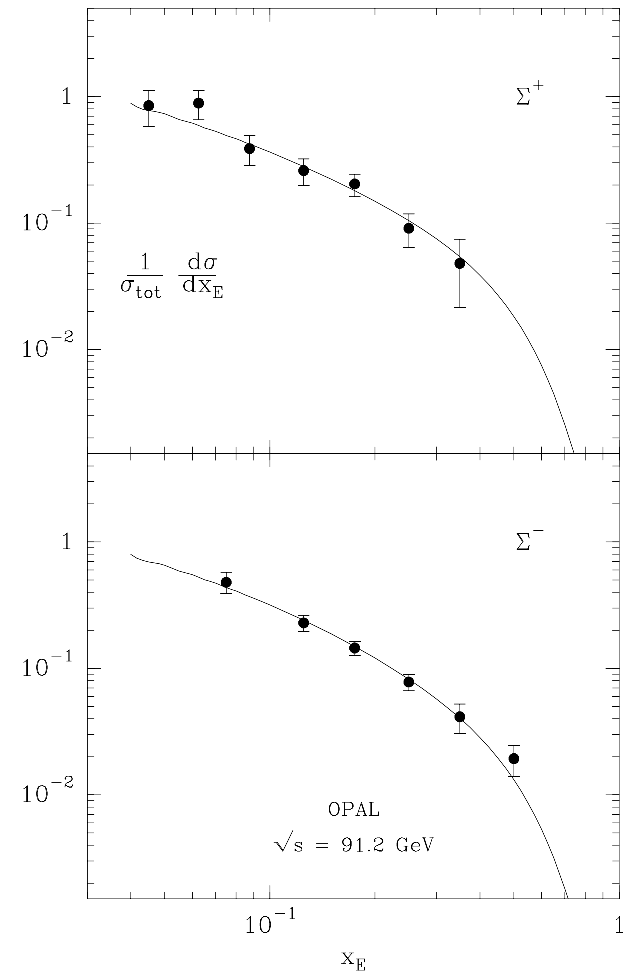

Figure 59: Cross sections for $\Sigma^{\pm}$ production in e^+e^- annihilation at the Z-pole as function of x_E. The experimental data are from Ref. [61].

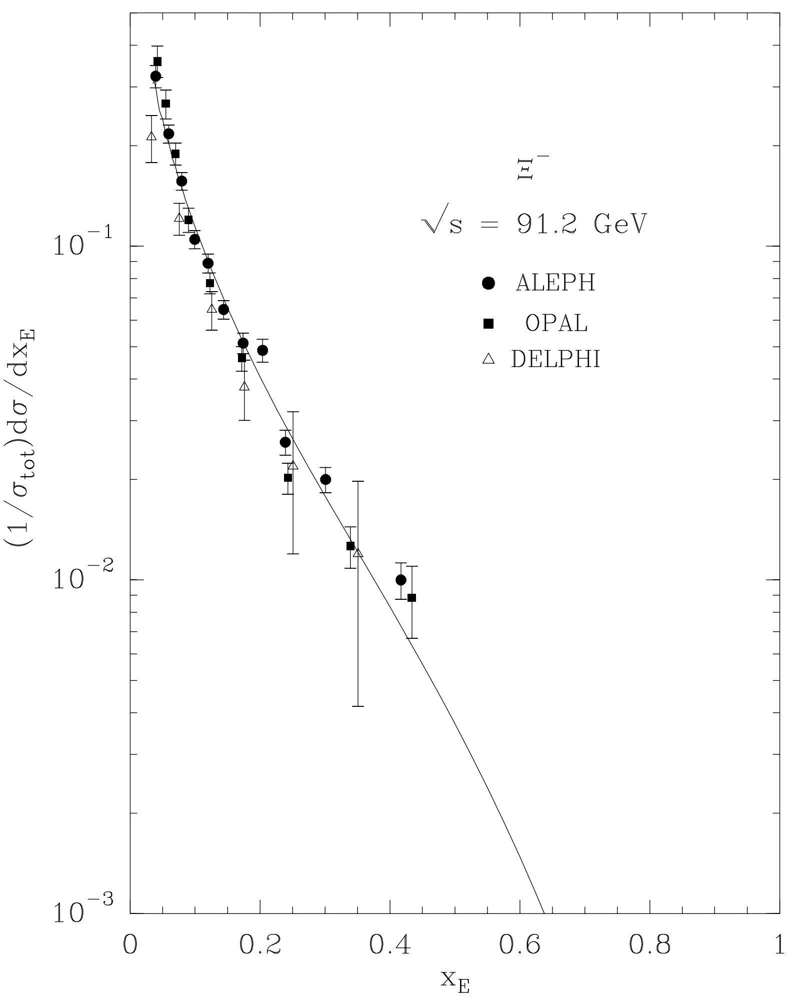

Figure 60: Cross sections for Ξ^- production in e^+e^- annihilation at the Z-pole as function of x_E. The experimental data are from Refs. [9, 61, 22].

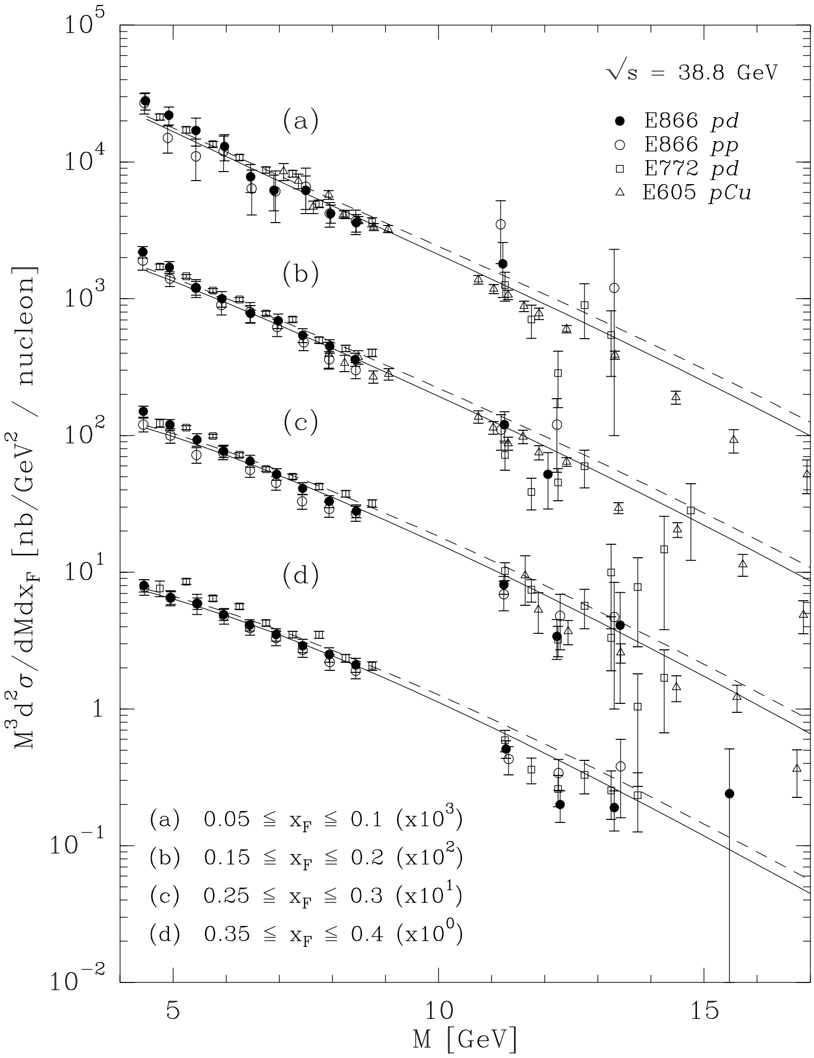

Figure 61: Drell-Yan cross sections per nucleon at $\sqrt{s} = 38.8$GeV for pp, pd, and pCu as a function of M for selected x_F bins. Experimental data are from Refs. [26, 27, 28].

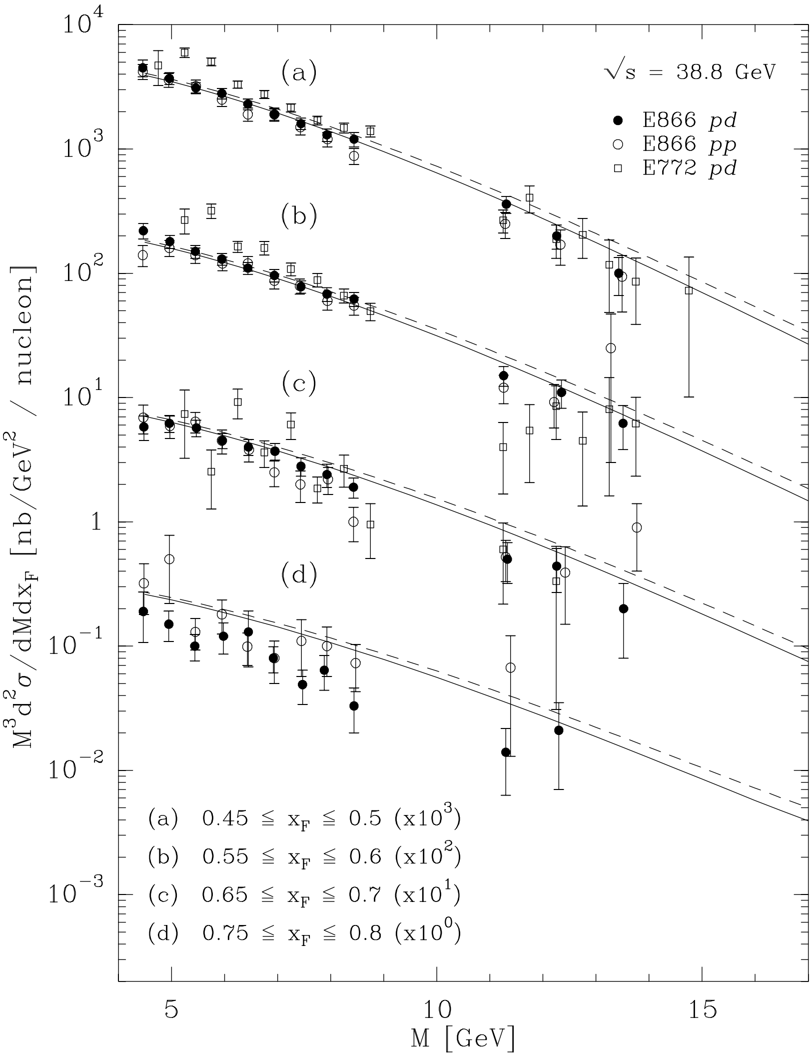

Figure 62: Drell-Yan cross sections per nucleon at $\sqrt{s} = 38.8$GeV for pp and pd as a function of M for selected x_F bins. Experimental data are from Refs. [26, 27].

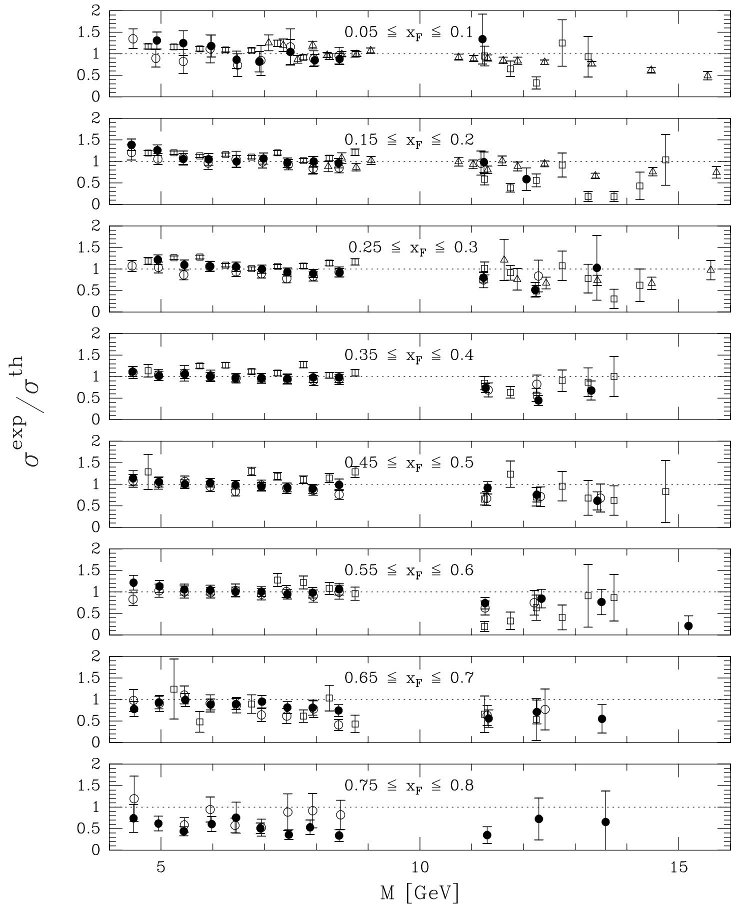

Figure 63: Drell-Yan cross sections ratios experiment vs theory at $\sqrt{s} = 38.8$GeV for pp, pd, and pCu as a function of M for selected x_F bins. Experimental data are from Refs. [26, 27, 28].

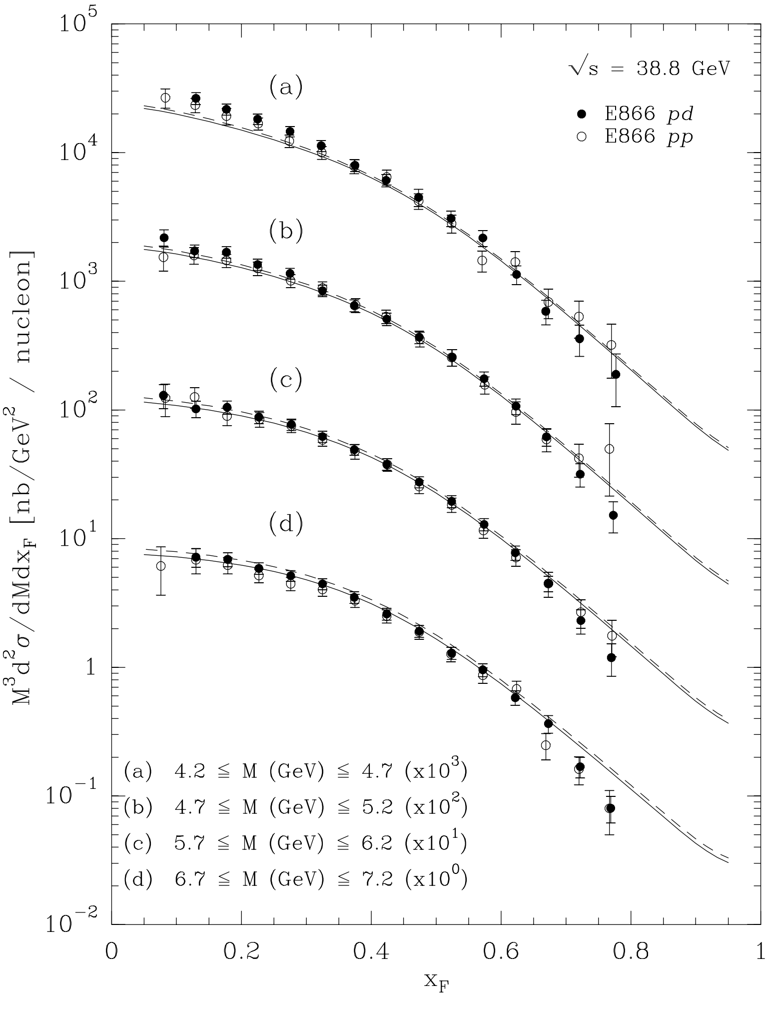

Figure 64: Drell-Yan cross sections per nucleon at $\sqrt{s} = 38.8$GeV for pp and pd as a function of x_F for selected M bins. Experimental data are from Ref. [26].

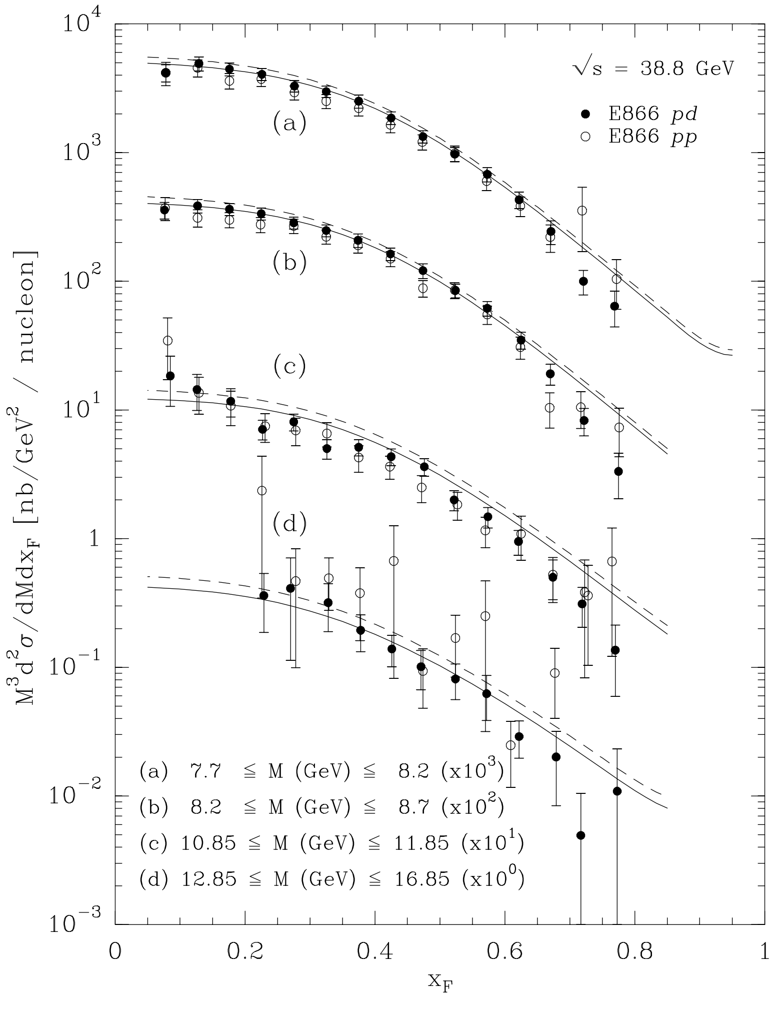

Figure 65: Drell-Yan cross sections per nucleon at $\sqrt{s} = 38.8$GeV for pp and pd as a function of x_F for selected M bins. Experimental data are from Ref. [26].

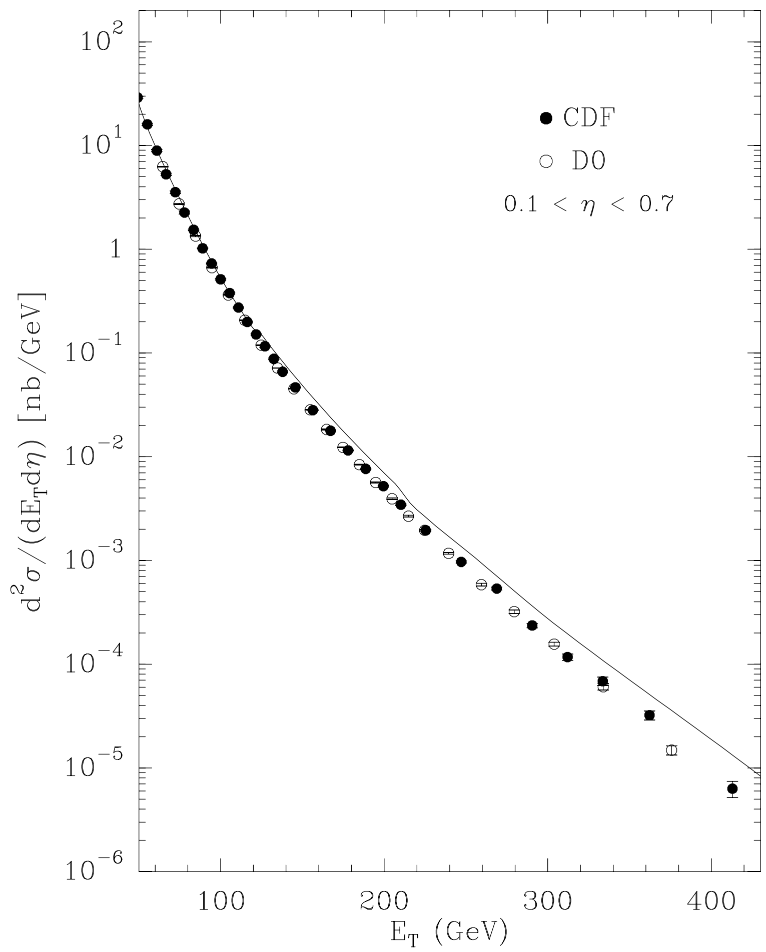

Figure 66: Cross section for single jet production in $\bar{p}p$ at $\sqrt{s} = 1.8$TeV as a function of E_T. Data from CDF [17] and D0 [18] collaborations.

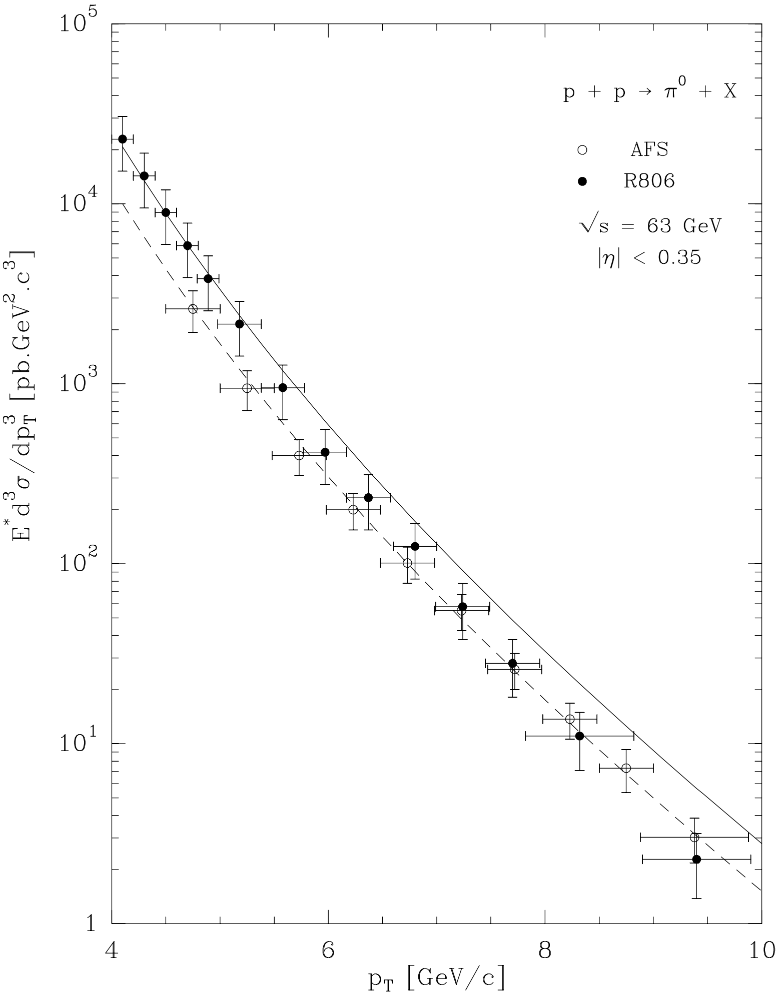

Figure 67: Inclusive π^0 production in pp reaction at $\sqrt{s} = 63$GeV as a function of p_T. Data from AFS [7] and R806 [63] Collaborations. Solid curve scale $\mu = p_T/2$, dashed $\mu = p_T$, fragmentation functions from KKP [100].

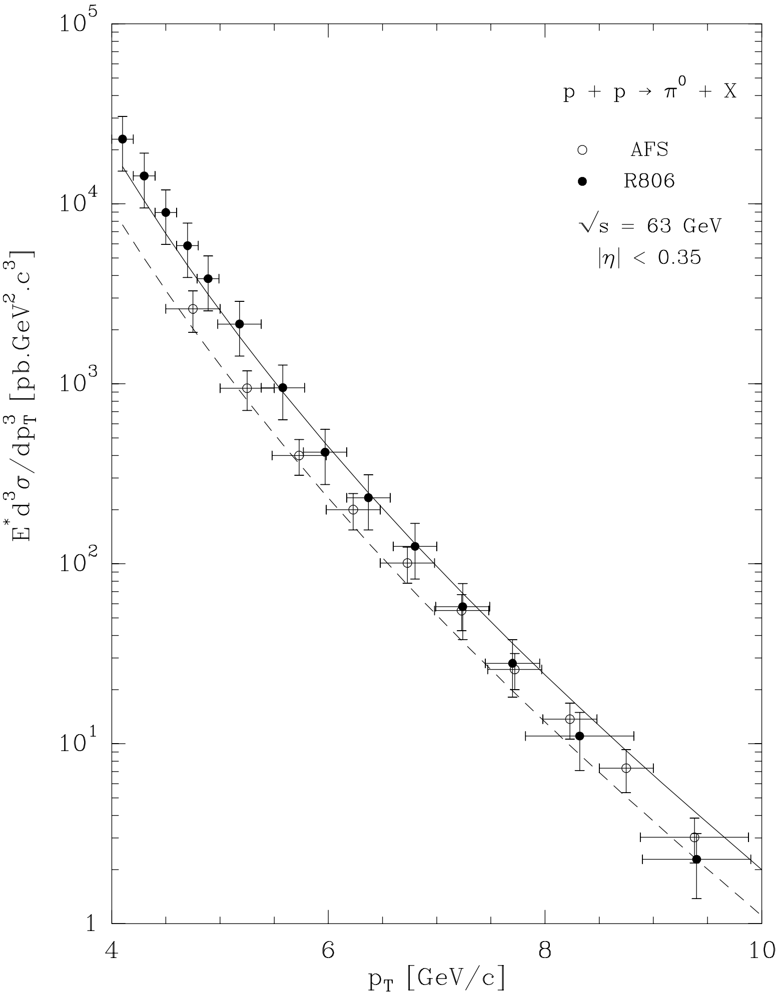

Figure 68: Inclusive π^0 production in pp reaction at $\sqrt{s} = 63$GeV as a function of p_T. Data from AFS [7] and R806 [63] Collaborations. Solid curve scale $\mu = p_T/2$, dashed $\mu = p_T$, fragmentation functions BKP [101].

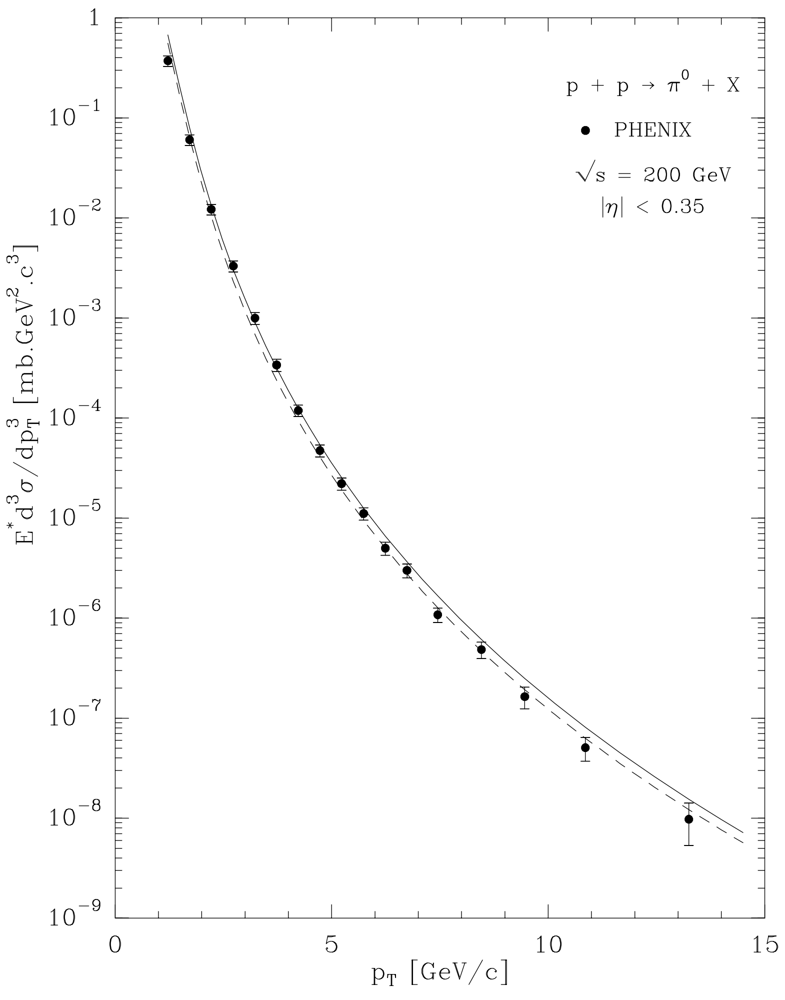

Figure 69: Inclusive π^0 production in pp reaction at $\sqrt{s} = 200$GeV as a function of p_T, scale $\mu = p_T$. Data from Phenix Collaboration [62]. Solid curve fragmentation functions from KKP [100], dashed curve BKP [101].

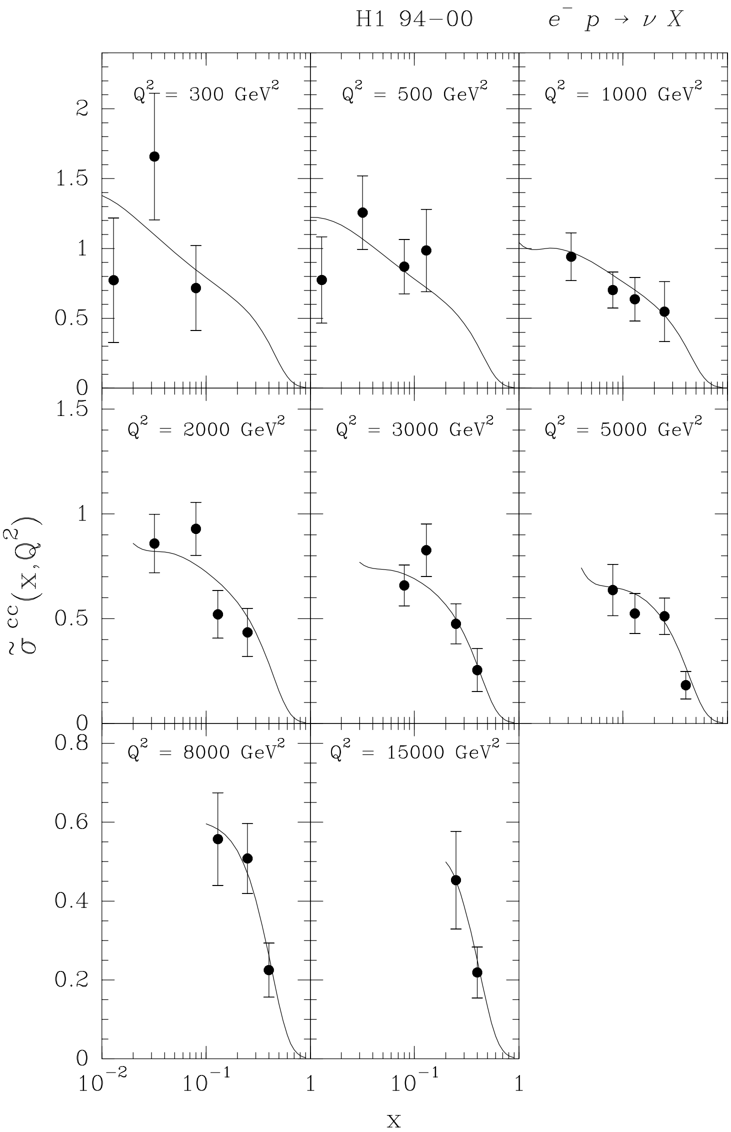

Figure 70: The reduced charged current cross section, $\tilde{\sigma}$, in e^-p reaction as a function of x, for different fixed values of Q^2. Data from H1 Coll. [40].

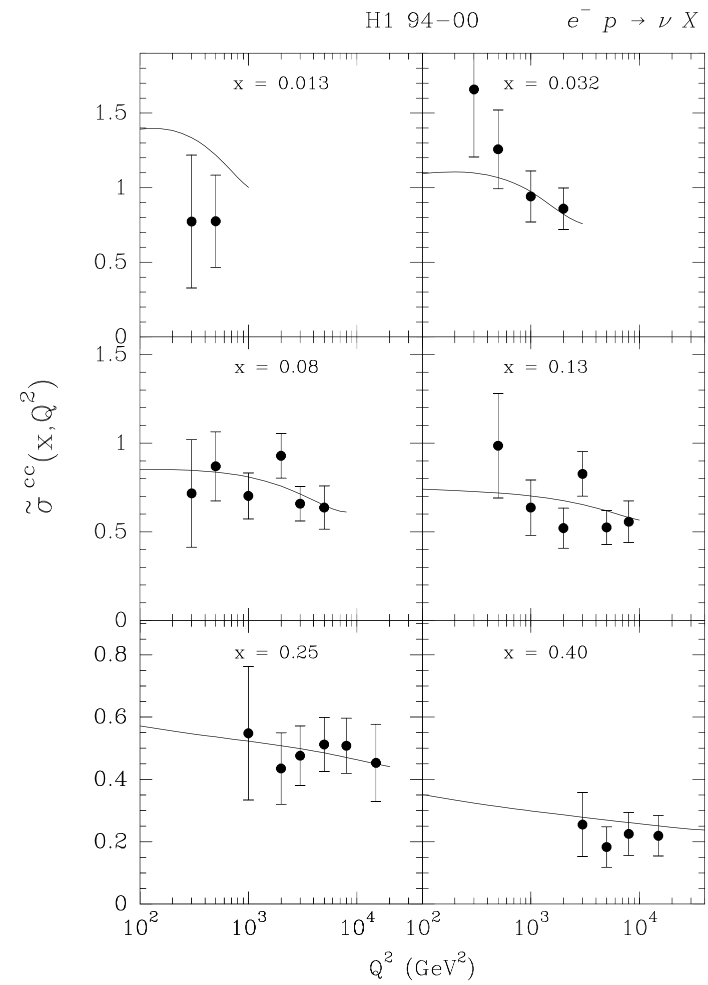

Figure 71: The reduced charged current cross section, $\tilde{\sigma}$, in e^-p reaction as a function of Q^2, for different fixed values of x. Data from H1 Coll. [40].

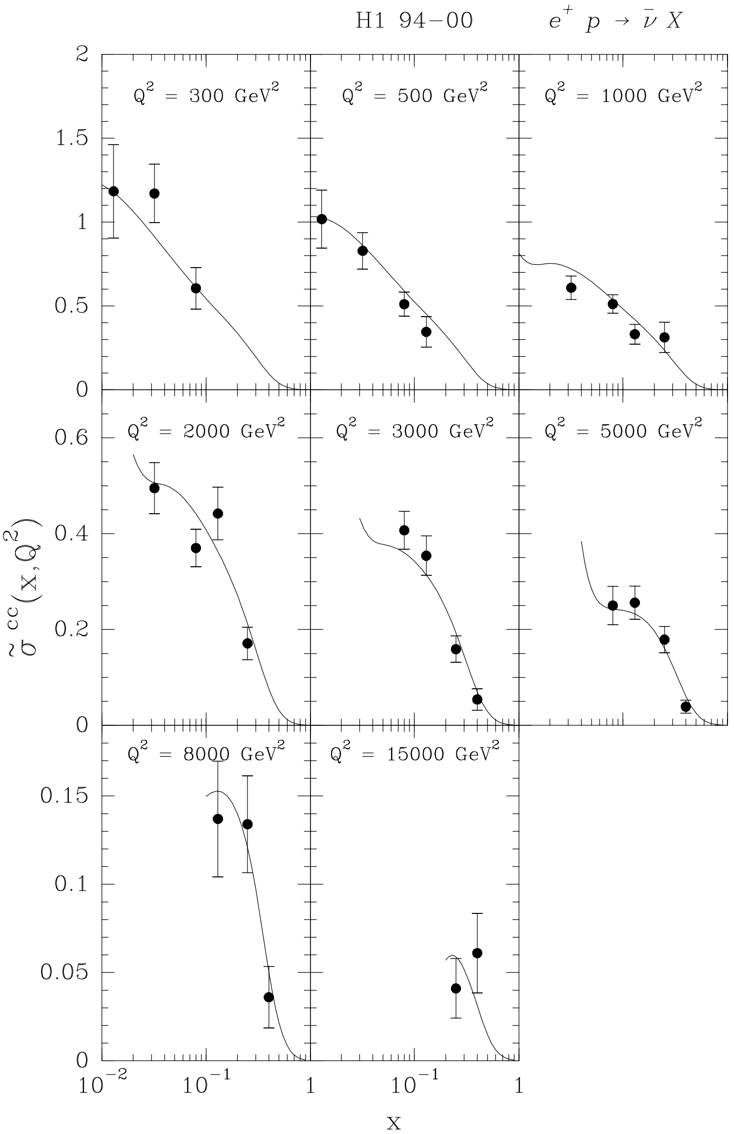

Figure 72: The reduced charged current cross section, $\tilde{\sigma}$, in e^+p reaction as a function of x, for different fixed values of Q^2. Data from H1 Coll. [41].

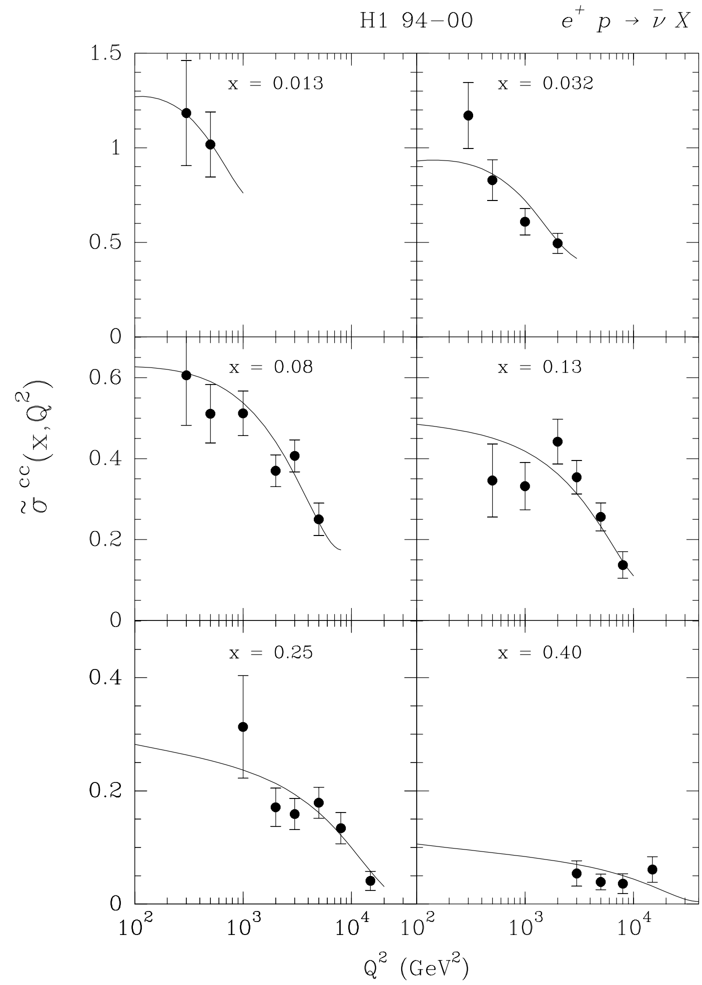

Figure 73: The reduced charged current cross section, $\tilde{\sigma}$, in e^+p reaction as a function of Q^2, for different fixed values of x. Data from H1 Coll. [41].

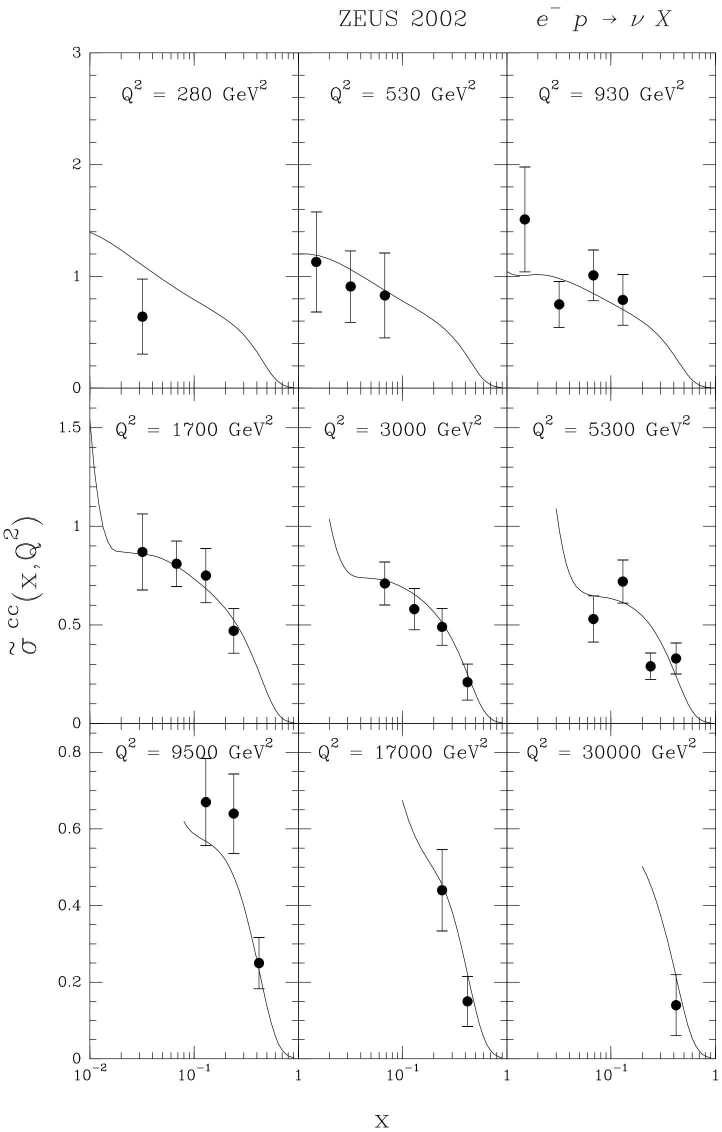

Figure 74: The reduced charged current cross section, $\tilde{\sigma}$, in e^-p reaction as a function of x, for different fixed values of Q^2. Data from ZEUS Coll. [96].

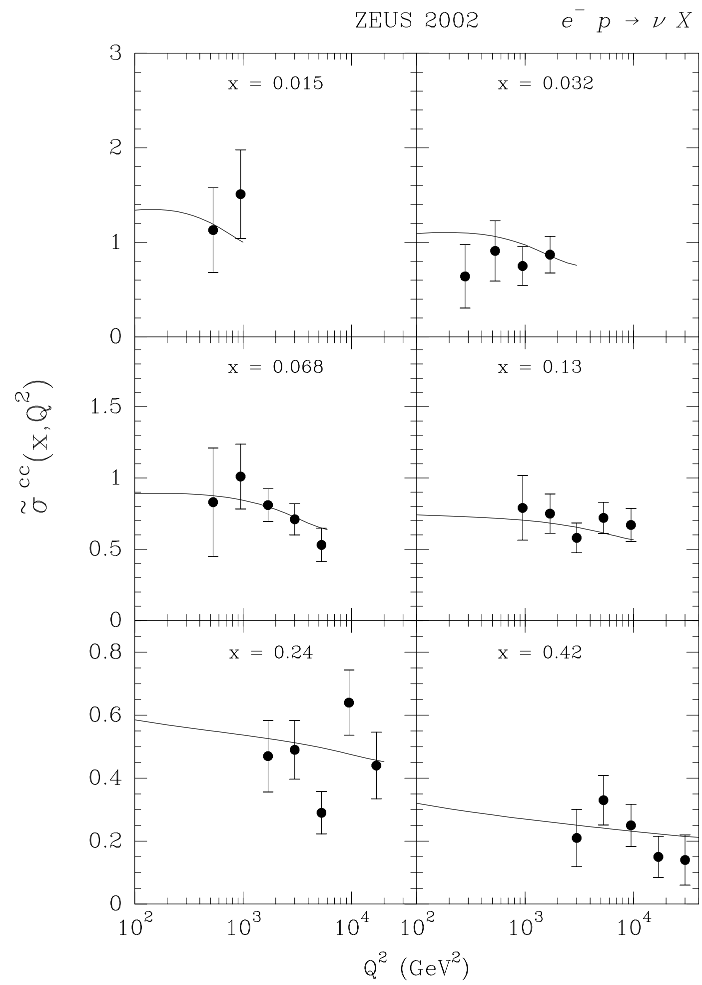

Figure 75: The reduced charged current cross section, $\tilde{\sigma}$, in e^-p reaction as a function of Q^2, for different fixed values of x. Data from ZEUS Coll. [96].

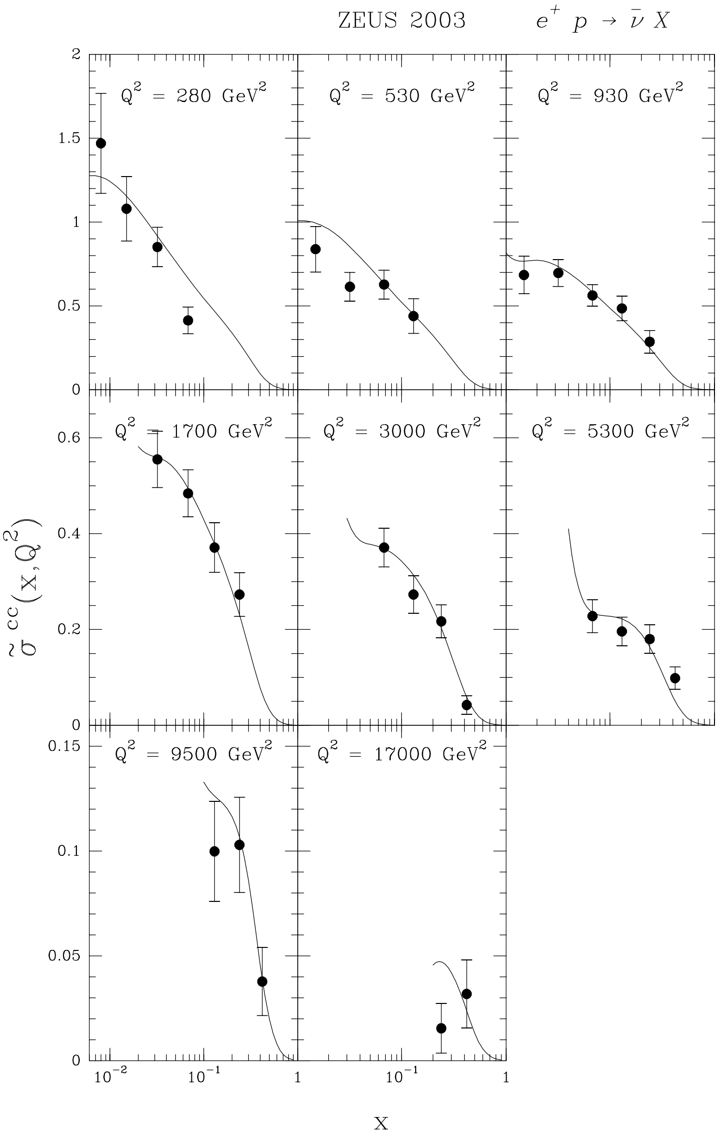

Figure 76: The reduced charged current cross section, $\tilde{\sigma}$, in e^+p reaction as a function of x, for different fixed values of Q^2. Data from ZEUS Coll. [97].

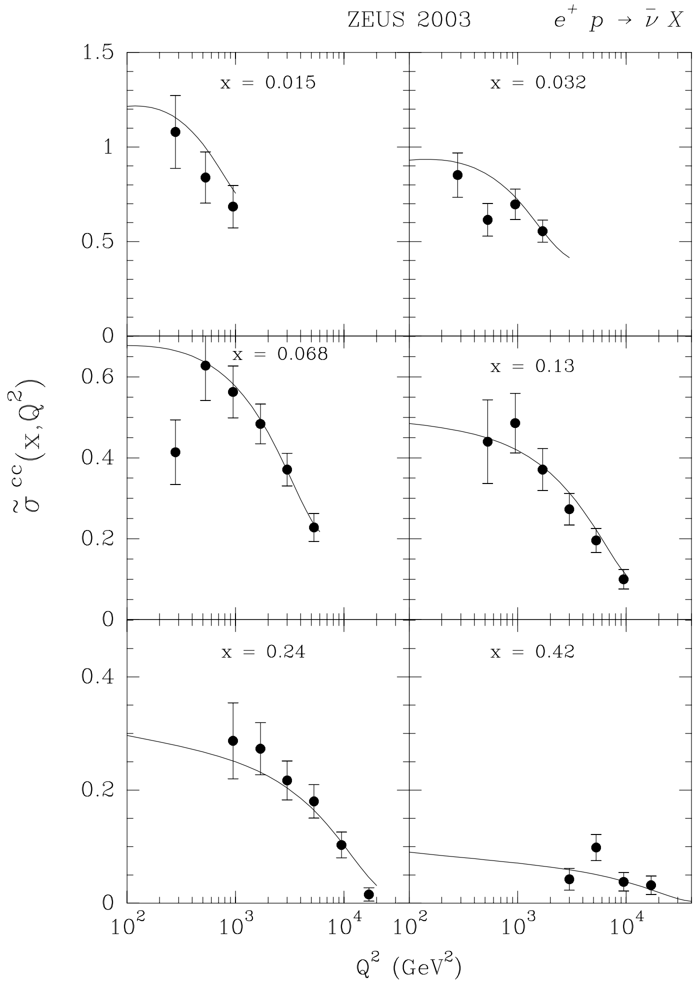

Figure 77: The reduced charged current cross section, $\tilde{\sigma}$, in e^+p reaction as a function of Q^2, for different fixed values of x. Data from ZEUS Coll. [97].

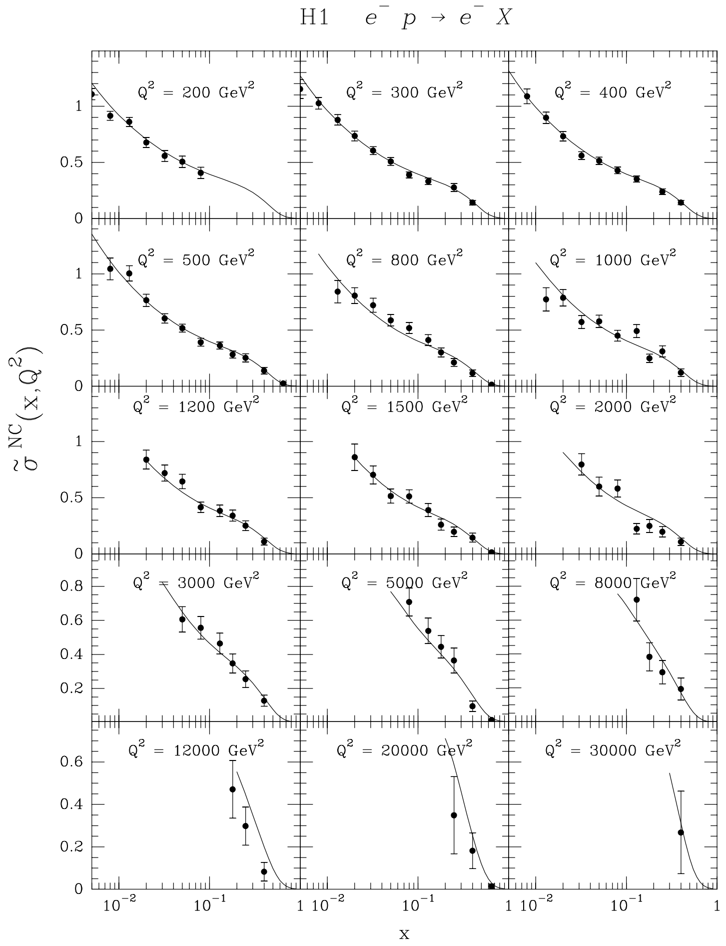

Figure 78: The reduced neutral current cross section $\tilde{\sigma}$, in e^-p reaction as a function of x, for different fixed values of Q^2 and $\sqrt{s} = 320$GeV. Data from H1 Coll [40]

.

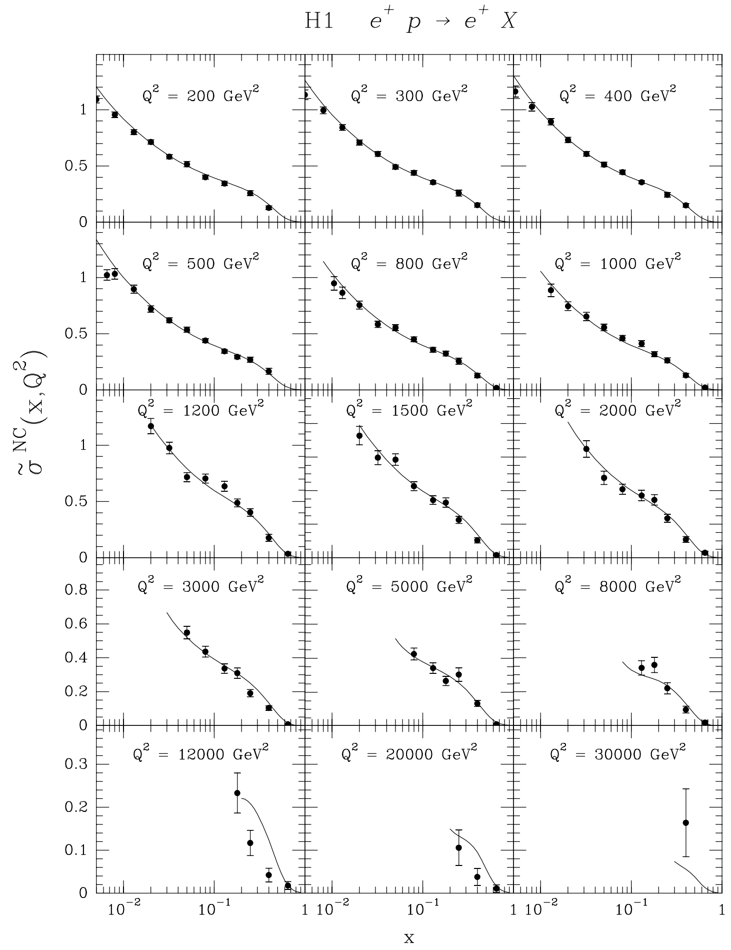

Figure 79: The reduced neutral current cross section $\tilde{\sigma}$, in e^+p reaction as a function of x, for different fixed values of Q^2 and $\sqrt{s} = 319$GeV. Data from H1 Coll [40]

.

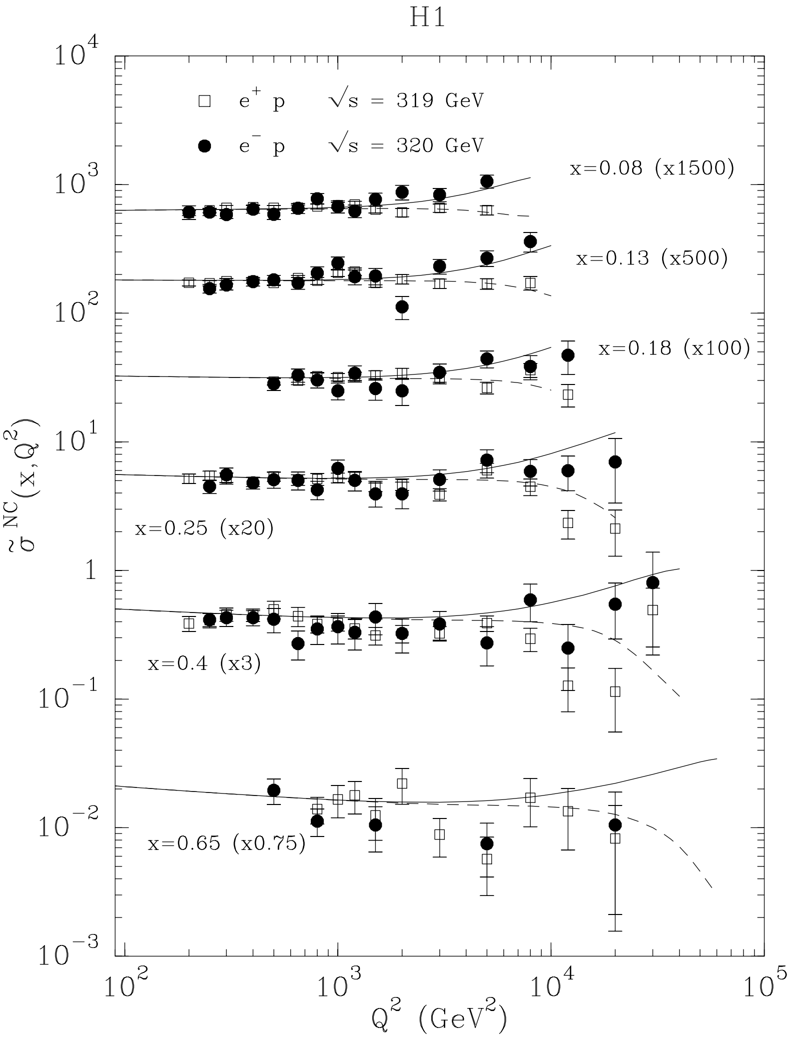

Figure 80: The reduced neutral current cross section $\tilde{\sigma}$, in $e^{\pm}p$ reaction as a function of Q^2, for different fixed values of x. Solid line e^-p, dashed line e^+p. Data from H1 Coll [40]

.

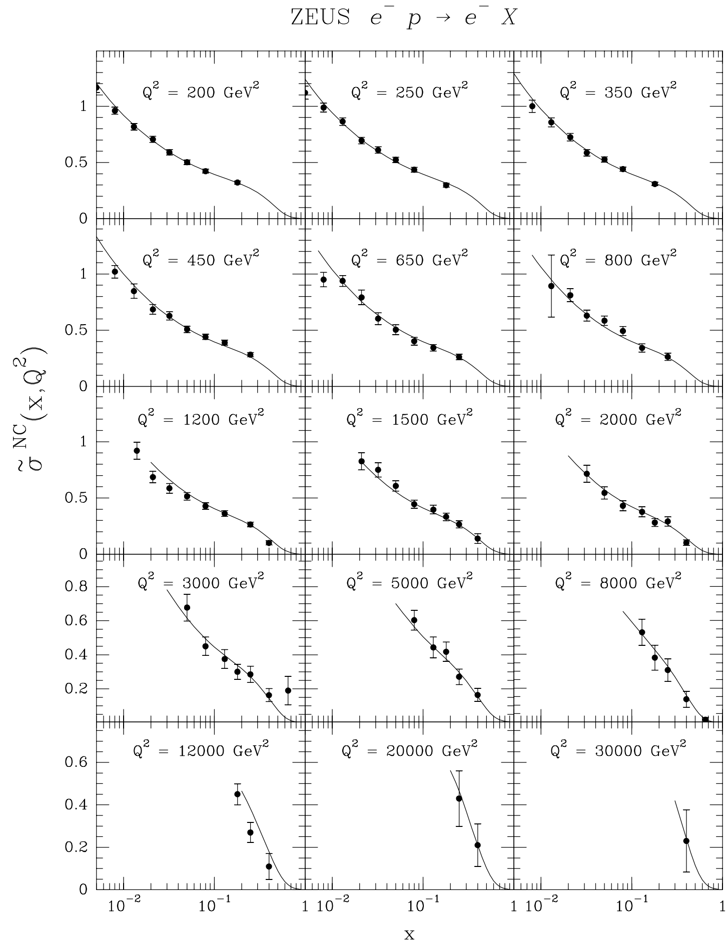

Figure 81: The reduced neutral current cross section $\tilde{\sigma}$, in e^-p reaction as a function of x, for different fixed values of Q^2 and $\sqrt{s} = 318$GeV. Data from Zeus Coll [97]

.

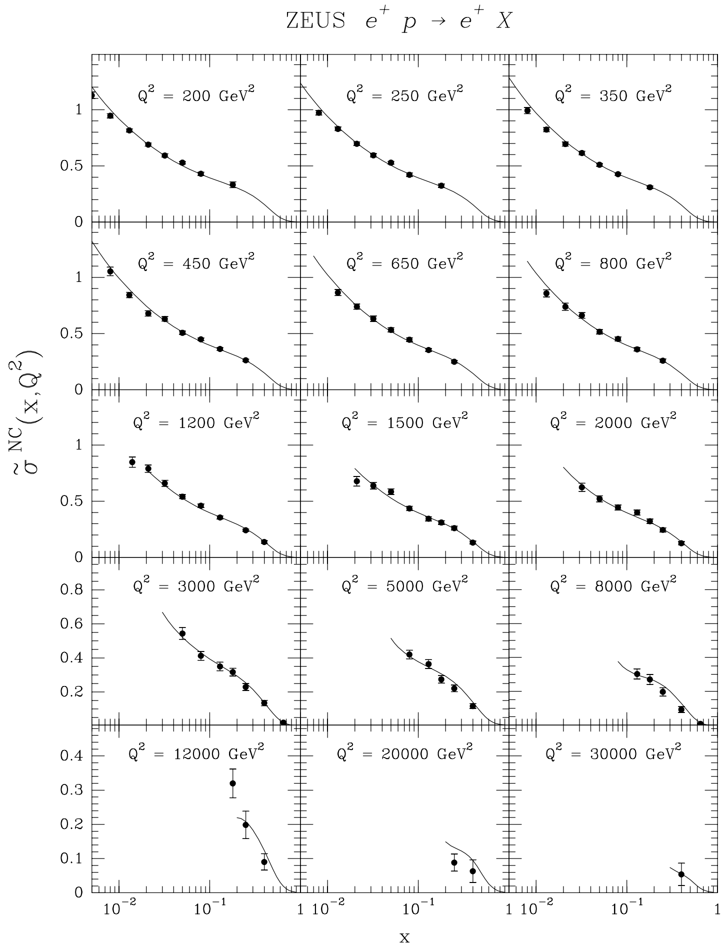

Figure 82: The reduced neutral current cross section $\tilde{\sigma}$, in e^+p reaction as a function of x, for different fixed values of Q^2 and $\sqrt{s} = 318$GeV. Data from Zeus Coll [97]

.

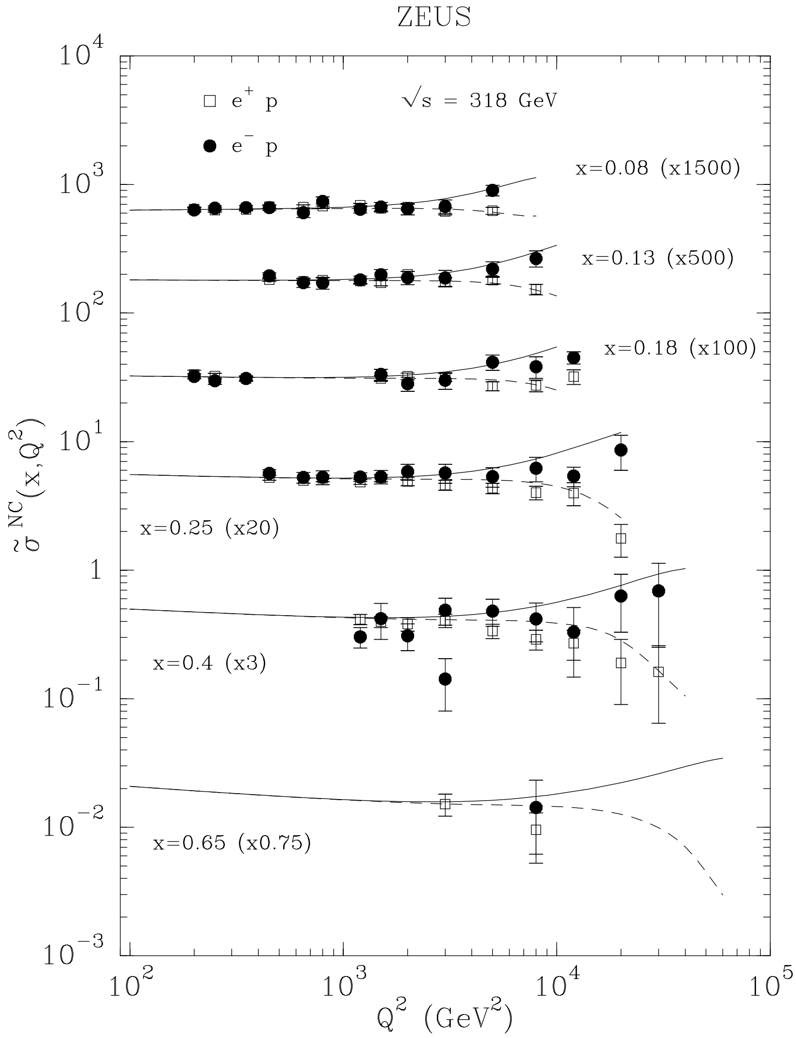

Figure 83: The reduced neutral current cross section $\tilde{\sigma}$, in $e^{\pm}p$ reaction as a function of Q^2, for different fixed values of x. Solid line e^-p, dashed line e^+p. Data from Zeus Coll [97]
.

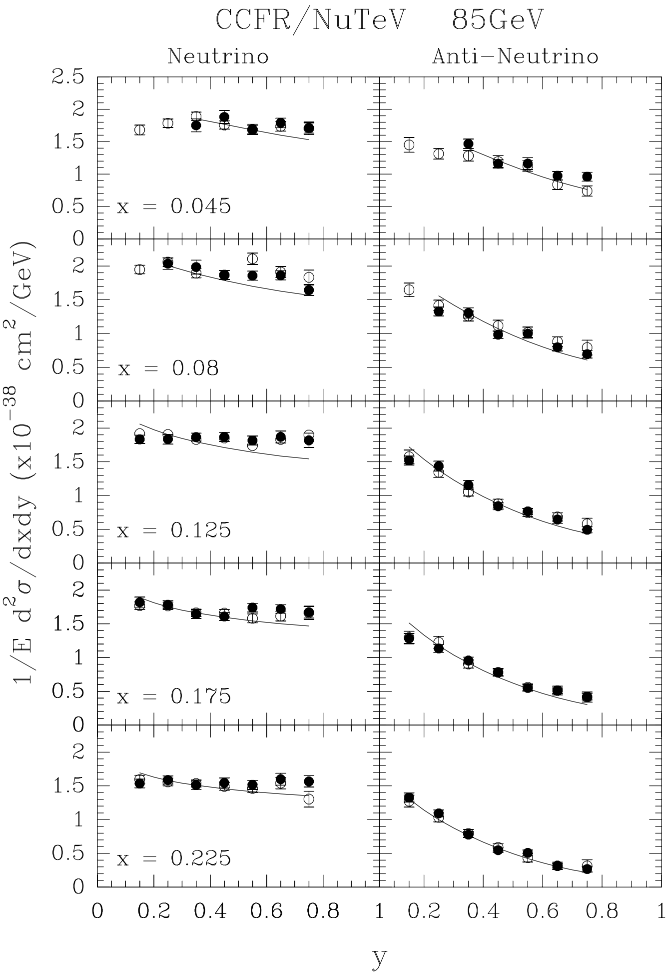

Figure 84: Differential cross section νN proton for $E_\nu = 85$GeV as a function of y for different x bins. Data from CCFR [29] and NuTeV collaboration [31, 30].

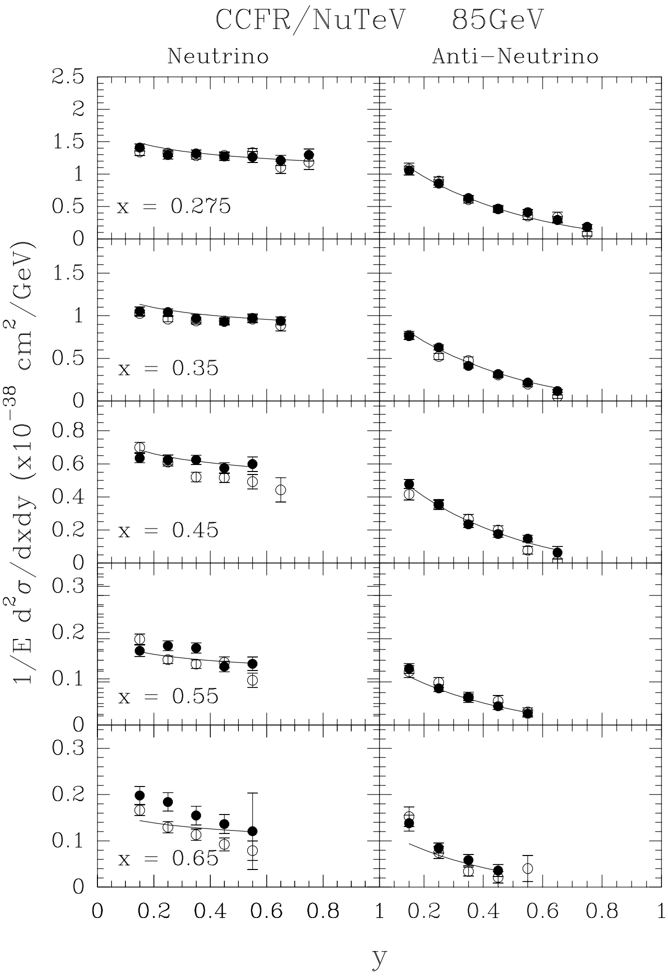

Figure 85: Differential cross section νN proton for $E_\nu = 85$GeV as a function of y for different x bins. Data from CCFR [29] and NuTeV collaboration [31, 30].

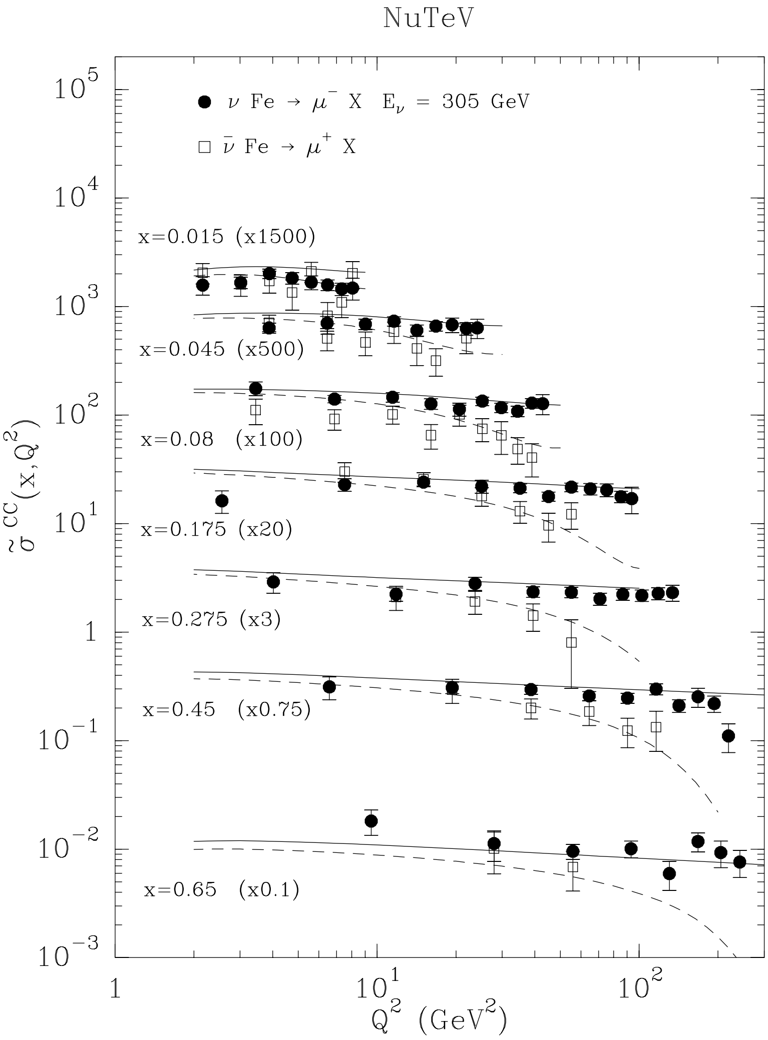

Figure 86: The reduced harged current cross section νN, for different x bins as a function of Q^2. The data points are obtained from the differential cross section [31, 30], they are not a direct measurement

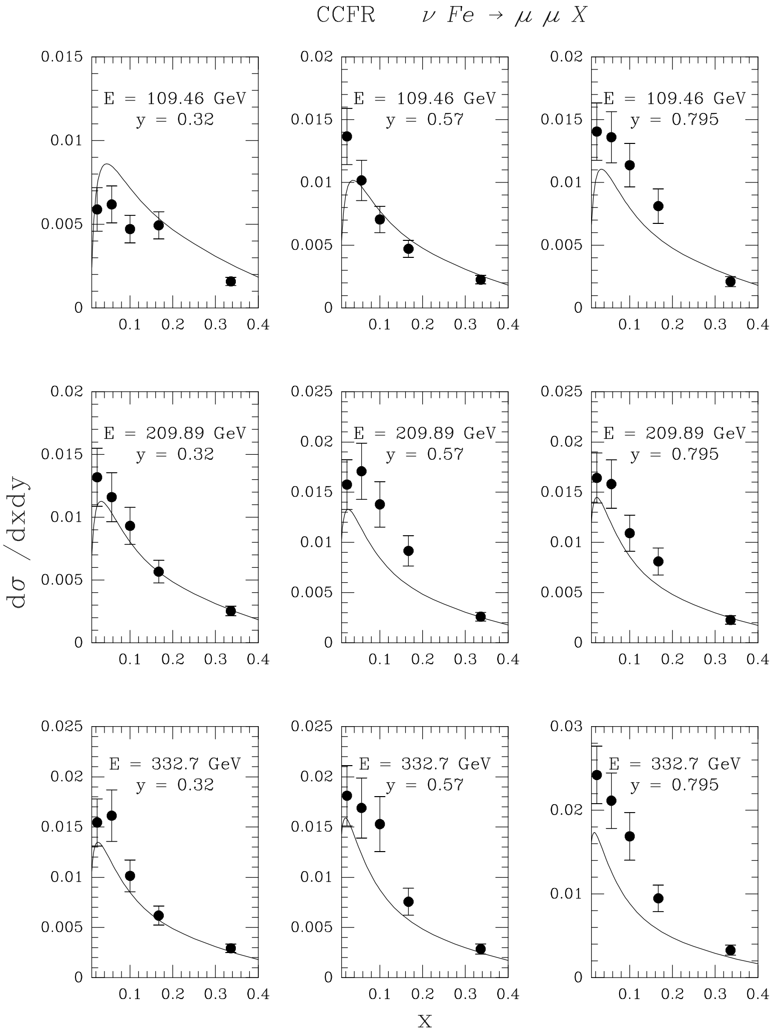

Figure 87: Comparison of the CCFR ν data [103] to the result of the fit for $d\sigma/dxdy$, in units of charged-current σ, for various kinematic ranges in energy, x and y.

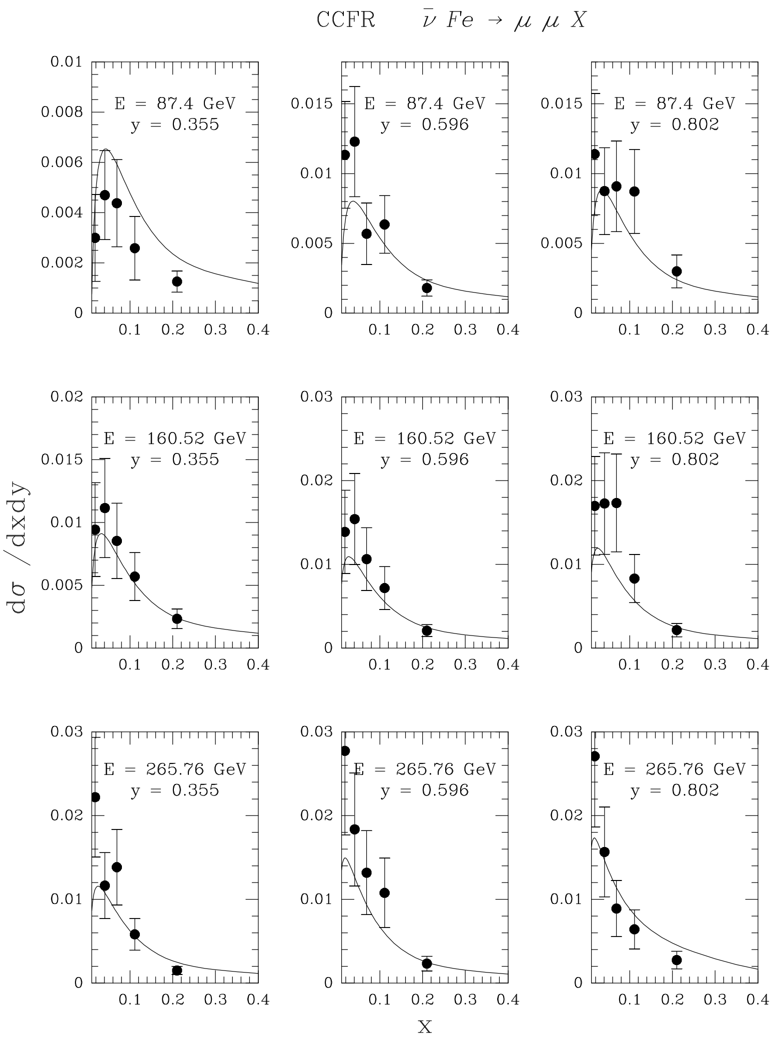

Figure 88: Comparison of the CCFR $\bar{\nu}$ data [103] to the result of the fit for $d\sigma/dxdy$ in units of charged-current σ, for various kinematic ranges in energy, x and y.

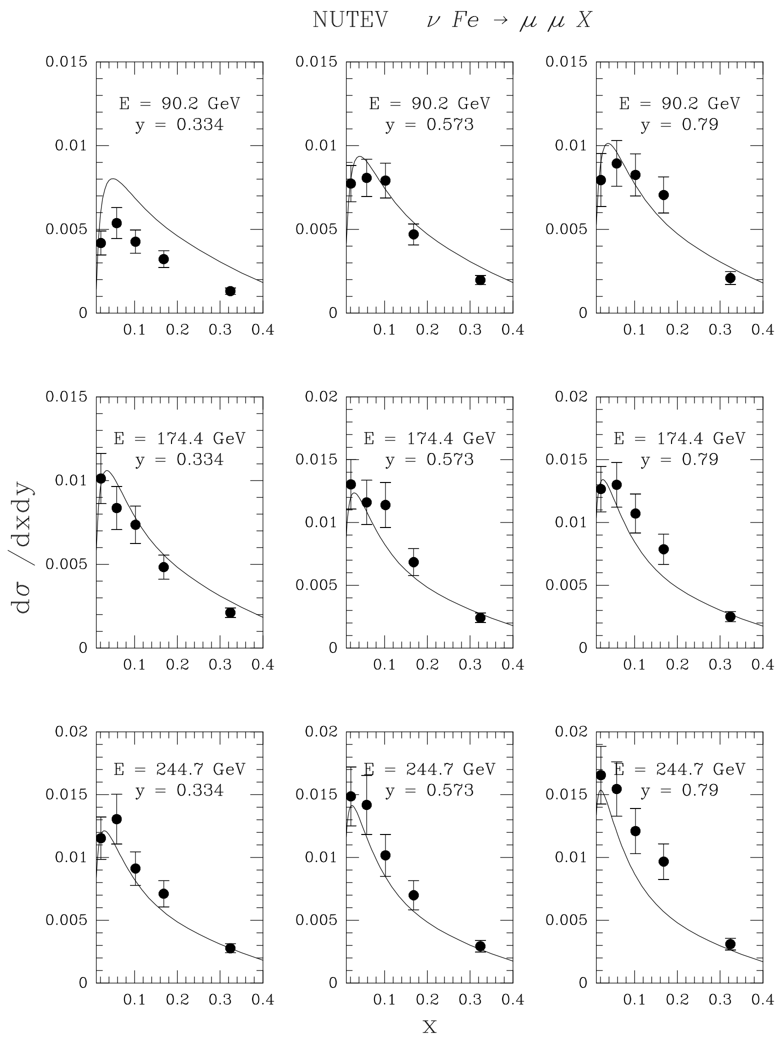

Figure 89: Comparison of the NuTeV ν data [103] to the result of the fit for $d\sigma/dxdy$, in units of charged-current σ, for various kinematic ranges in energy, x and y.

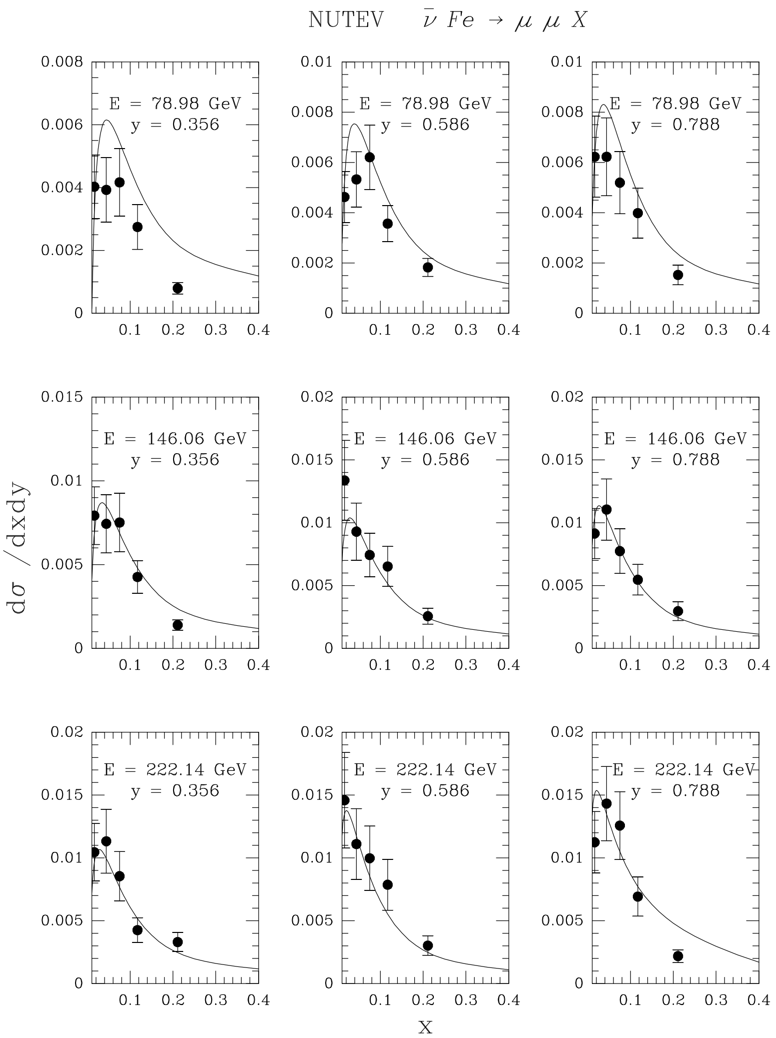

Figure 90: Comparison of the NuTeV $\bar{\nu}$ data [103] to the result of the fit for $d\sigma/dxdy$, in units of charged-current σ, for various kinematic ranges in energy, x and y.

5 Polarized experiments

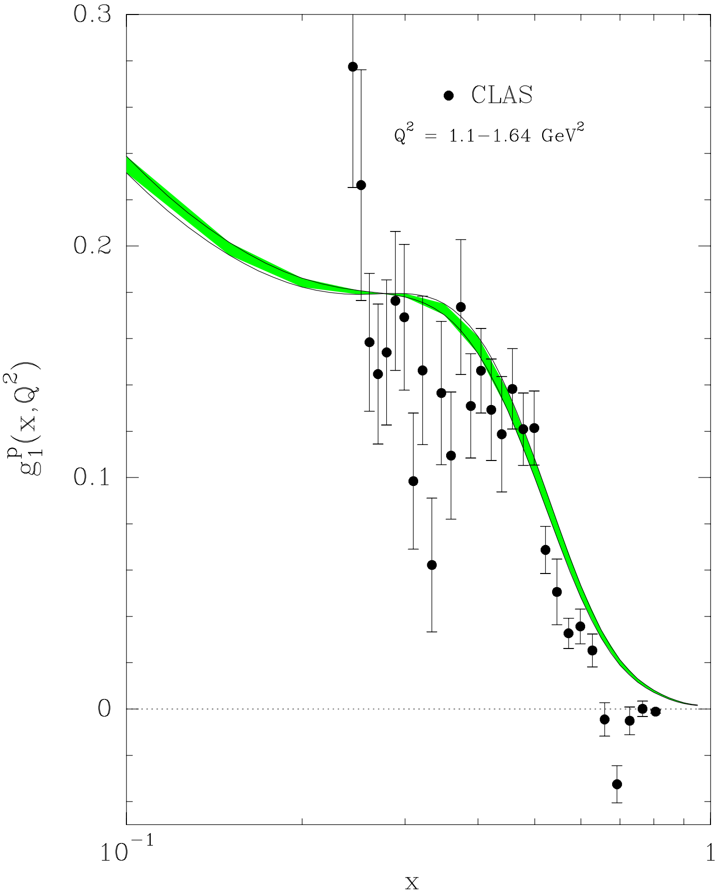

Figure 91: $g_1^p(x, Q^2)$ as function of x at for a range $1.1 \leq Q^2 \leq 1.64\mathrm{GeV}^2$, CLAS Coll [16]. The two curves represent the extreme Q^2 values.

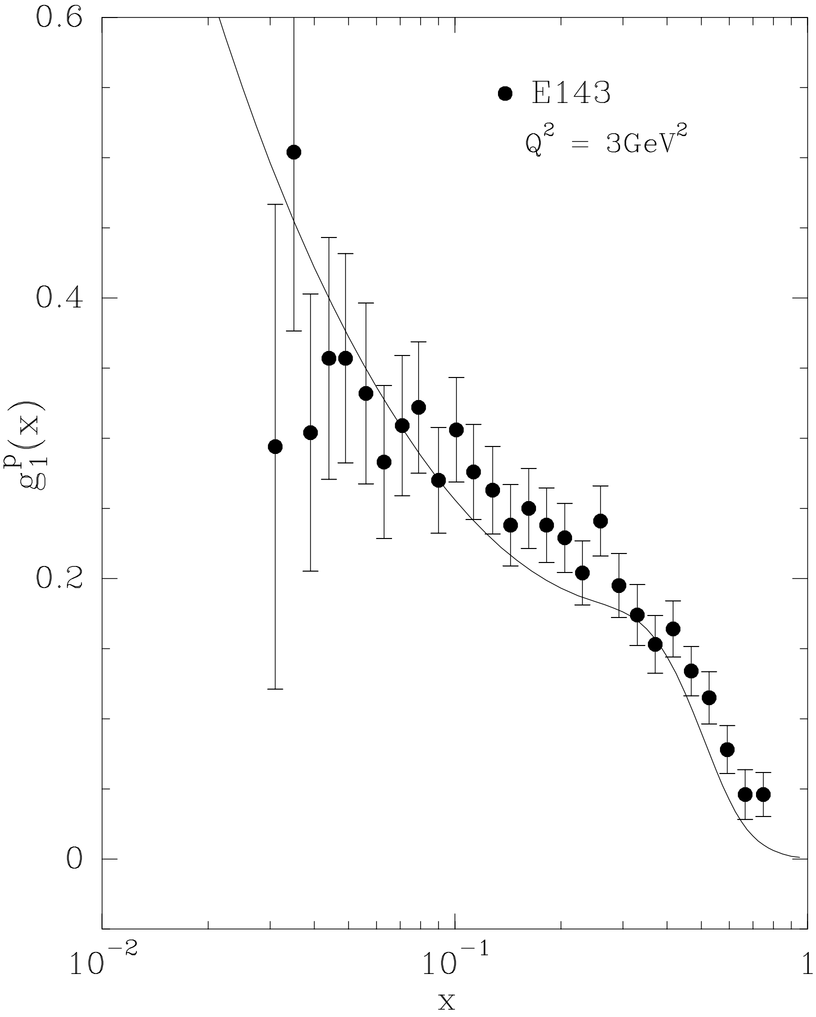

Figure 92: $g_1^p(x, Q^2)$ as function of x at fixed $Q^2 = 3\text{GeV}^2$, E143 Coll.

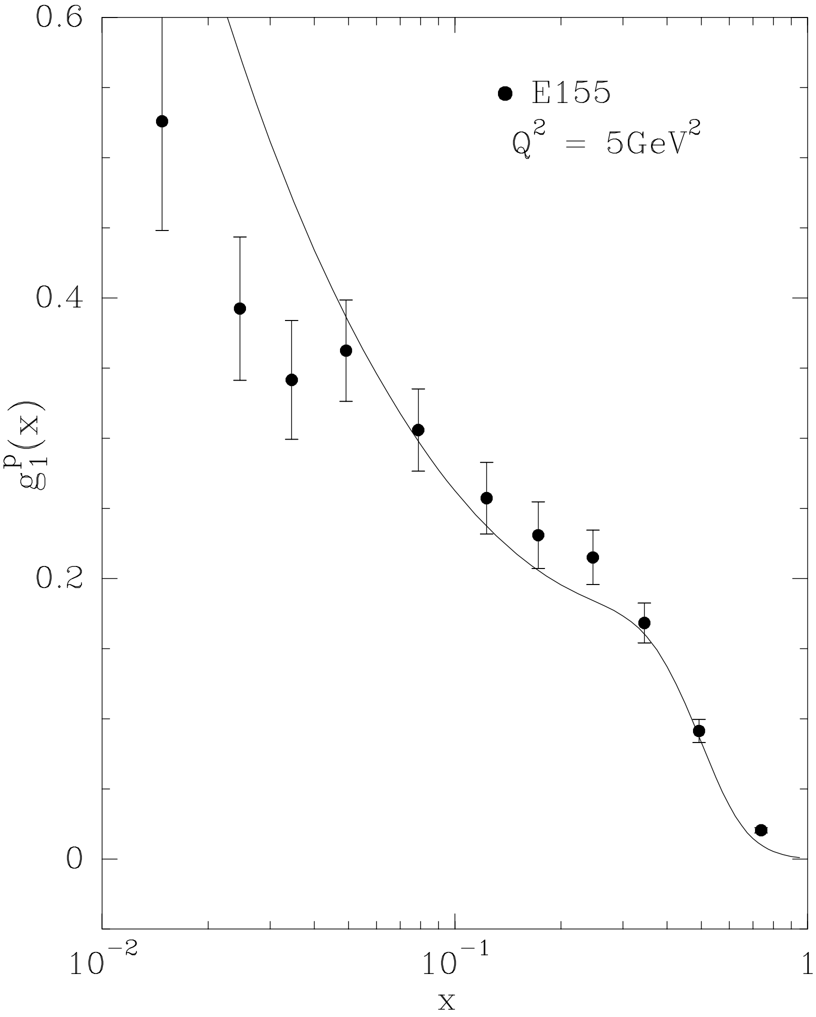

Figure 93: $g_1^p(x, Q^2)$ as function of x at fixed $Q^2 = 5\mathrm{GeV}^2$, E155 Coll.

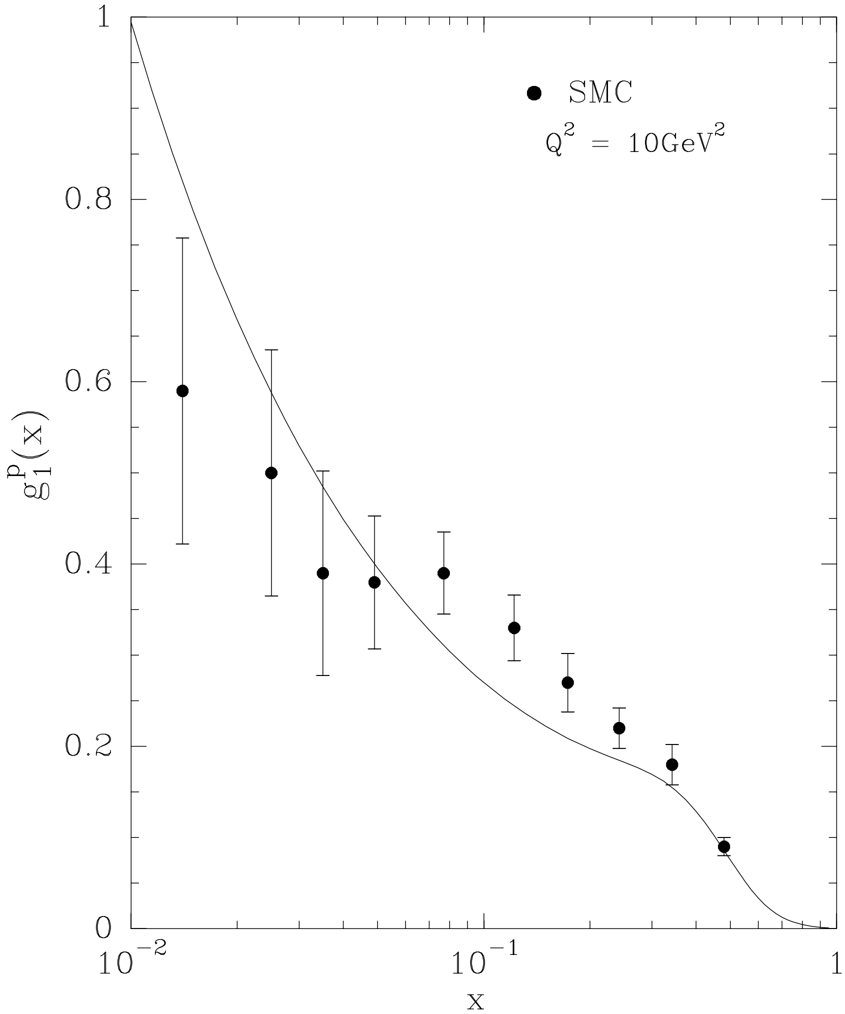

Figure 94: $g_1^p(x, Q^2)$ as function of x at fixed $Q^2 = 10\mathrm{GeV}^2$, evolved SMC data.

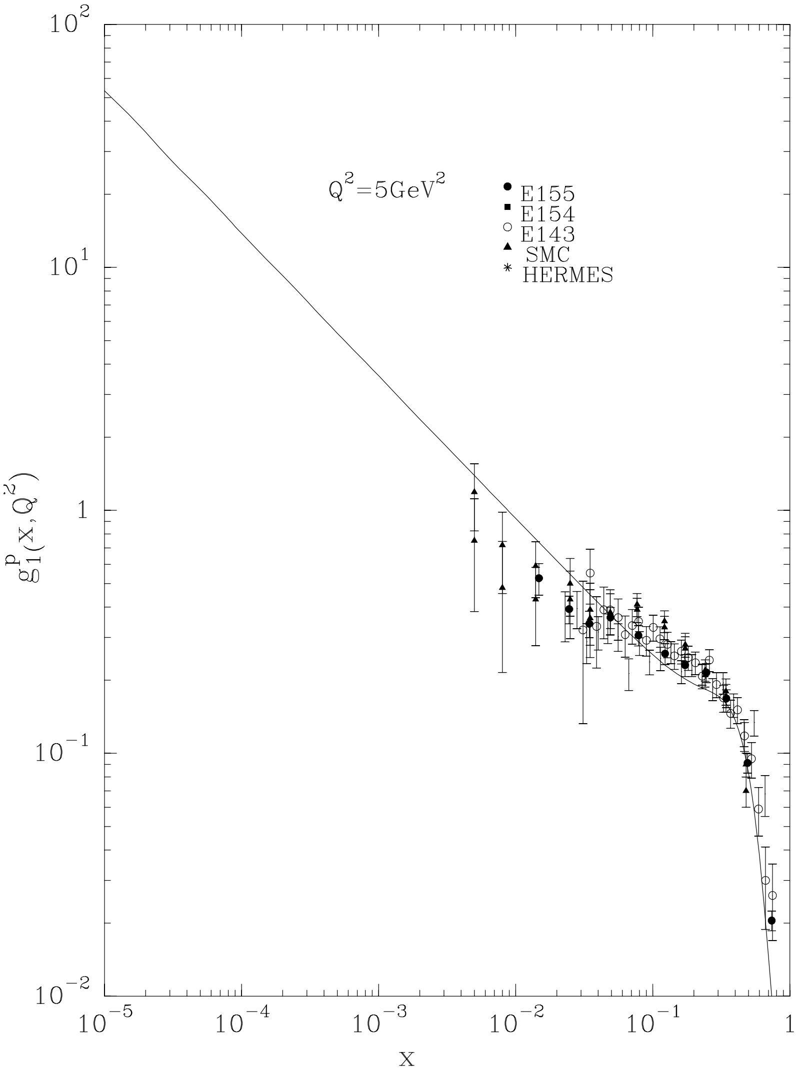

Figure 95: Behavior of $g_1^p(x, Q^2)$ at low x and fixed $Q^2 = 5\text{GeV}^2$,

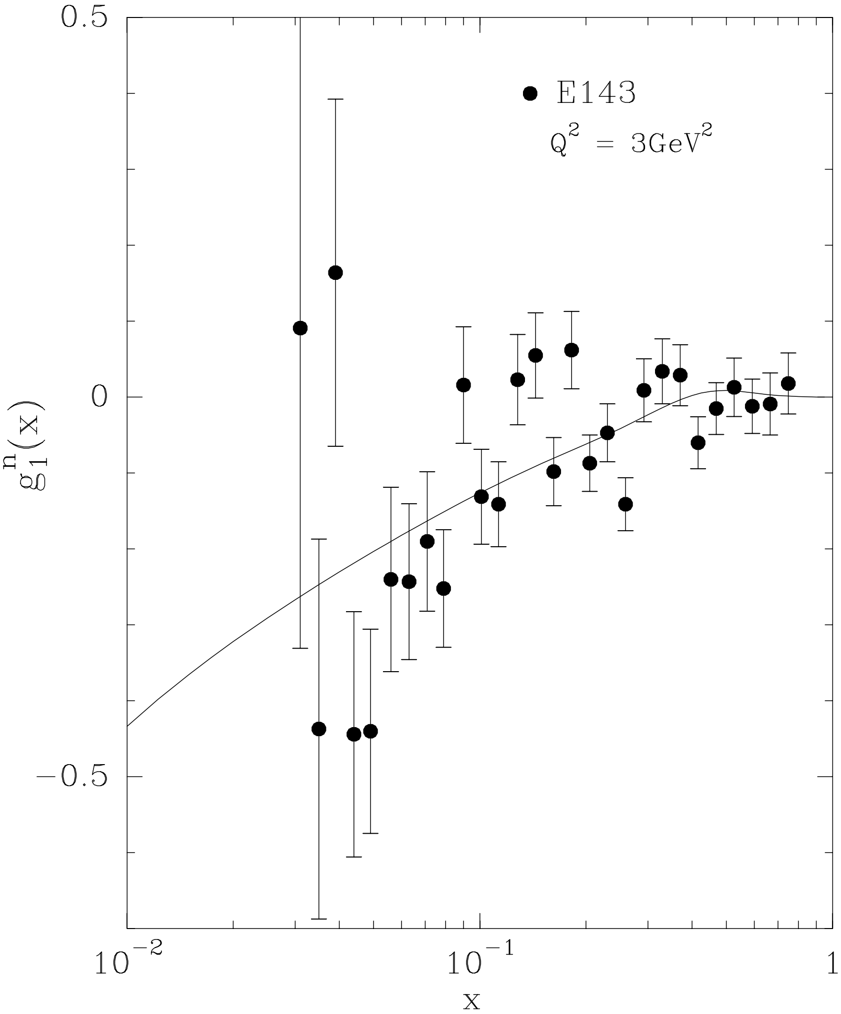

Figure 96: $g_1^n(x, Q^2)$ as function of x at fixed $Q^2 = 3\text{GeV}^2$, E143 Coll.

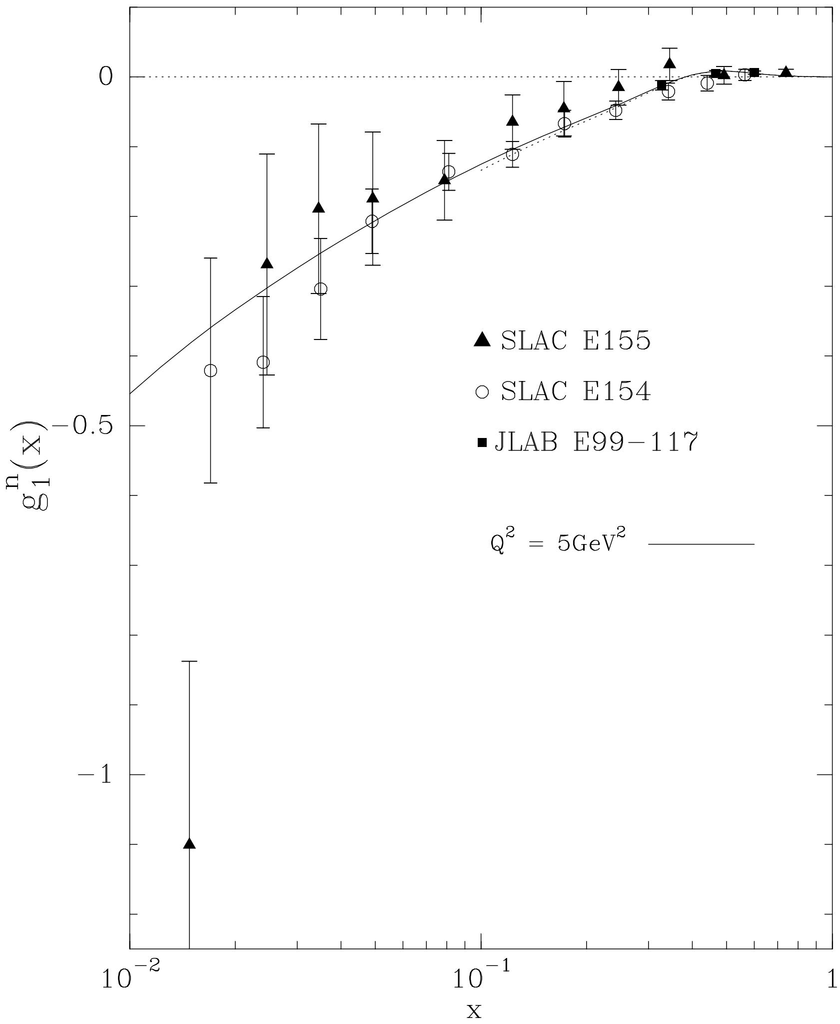

Figure 97: $g_1^n(x, Q^2)$ as function of x at fixed $Q^2 = 5\text{GeV}^2$, E154, E155, JLab Coll..

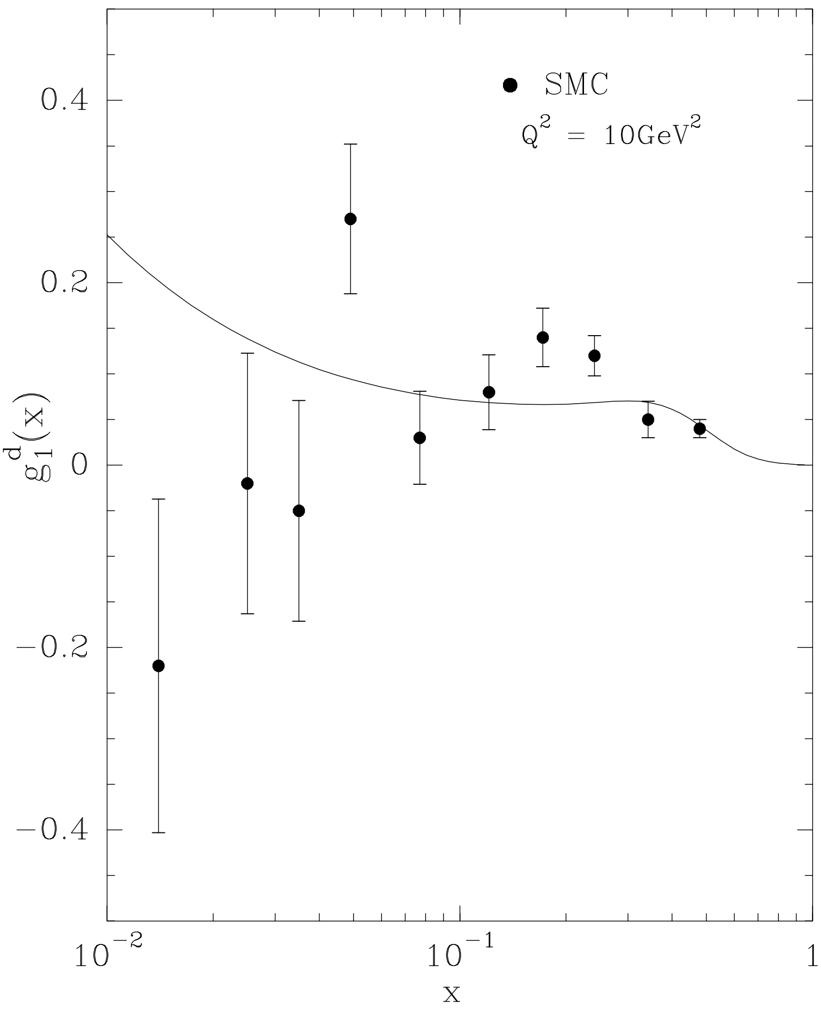

Figure 98: $g_1^d(x, Q^2)$ as function of x at fixed $Q^2 = 10\text{GeV}^2$, evolved SMC data.

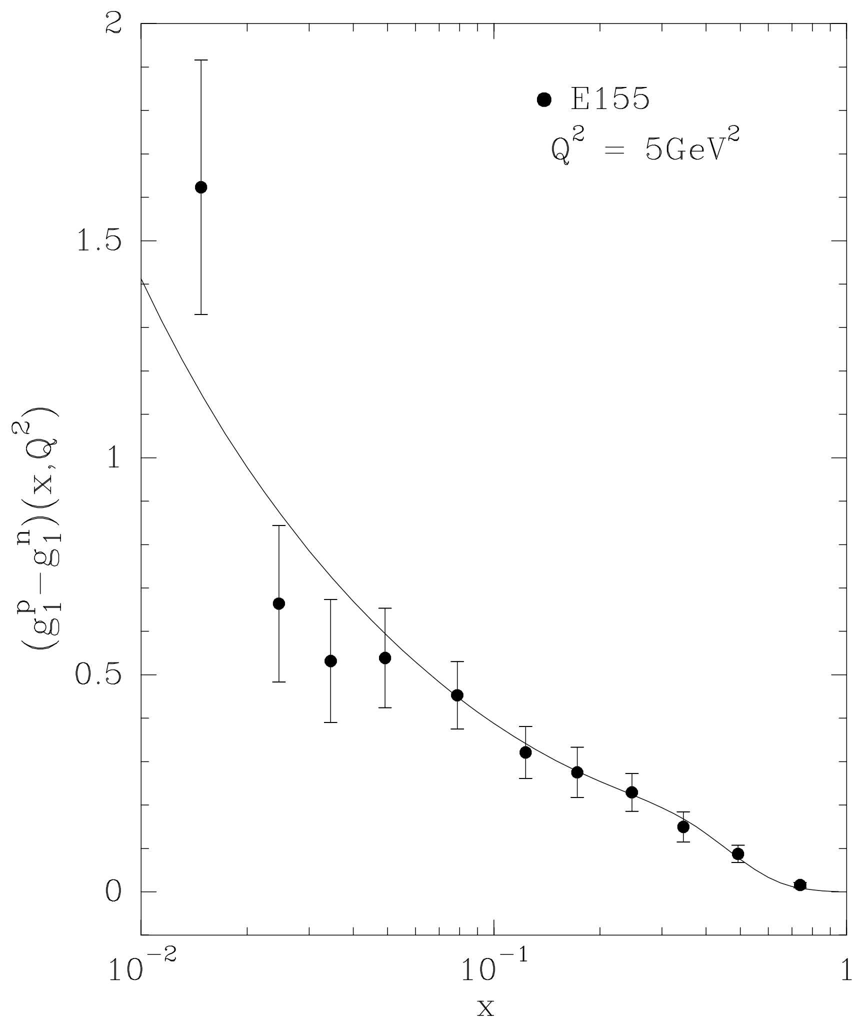

Figure 99: $g_1^p(x, Q^2) - g_1^n(x, Q^2)$ as function of x at fixed $Q^2 = 5\mathrm{GeV}^2$, E155 Coll..

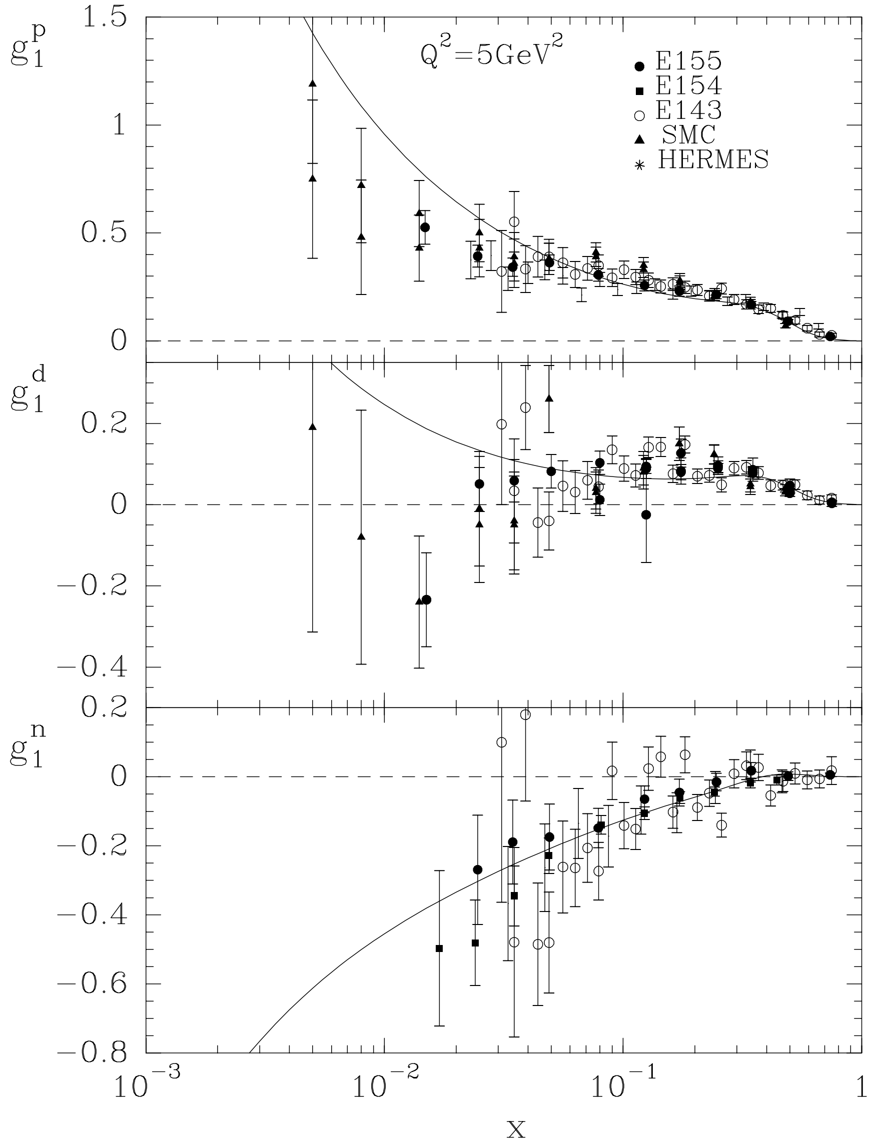

Figure 100: $g_1^{p,d,n}(x,Q^2)$ as function of x for different Q^2 values, from E155, E154, E143, SMC, HERMES experiments. The curves correspond to our model predictions at $Q^2 = 5\text{GeV}^2$.

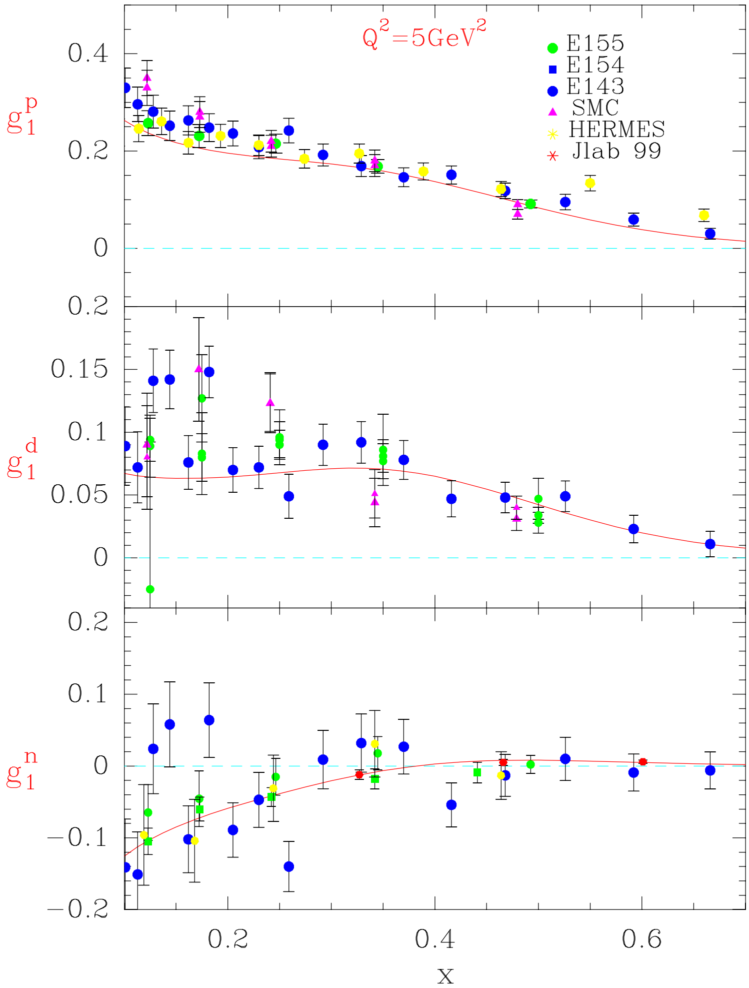

Figure 101: $g_1^{p,d,n}(x, Q^2)$ at large x values for different Q^2 values, from E155, E154, E143, SMC, HERMES, Jlab experiments. The curves correspond to our model predictions at $Q^2 = 5\mathrm{GeV}^2$.

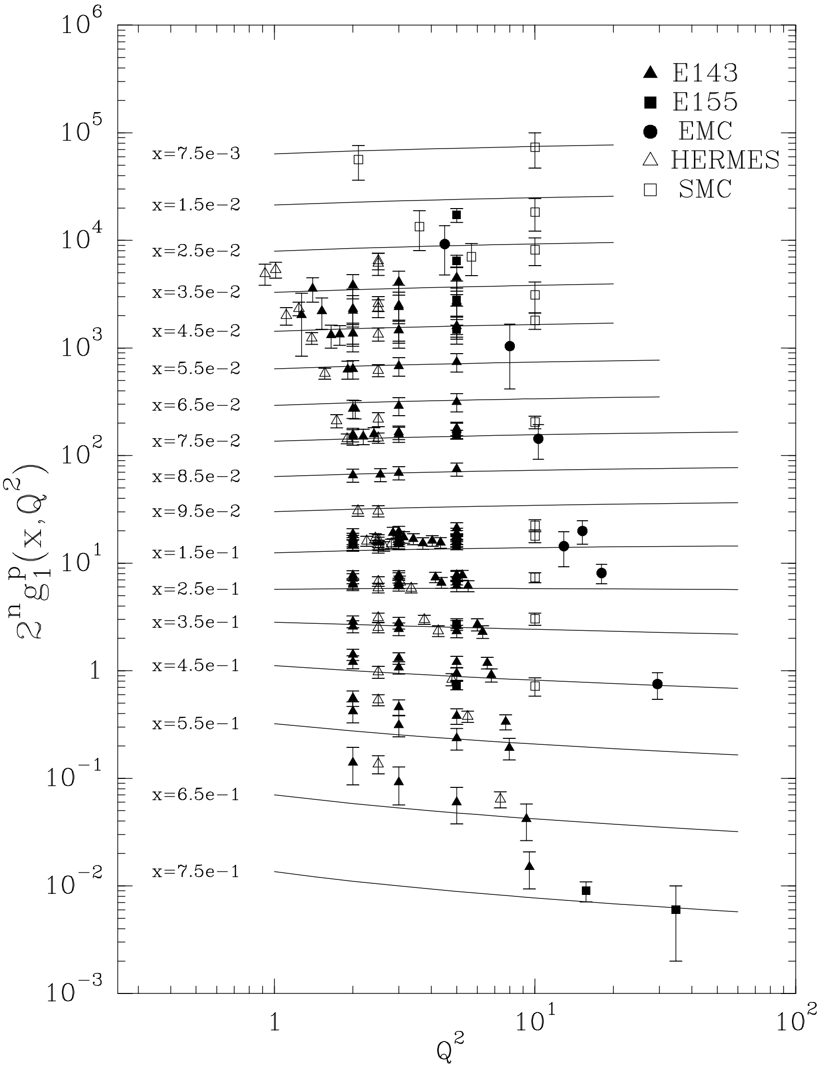

Figure 102: $2^n g_1^p(x, Q^2)$ as function of Q^2 for different x values. $n = 0$ corresponds to $x = 0.75$ and $n = 16$ to $x = 7.5\ 10^{-3}$. Experimental data are rebined to the nearest x values.

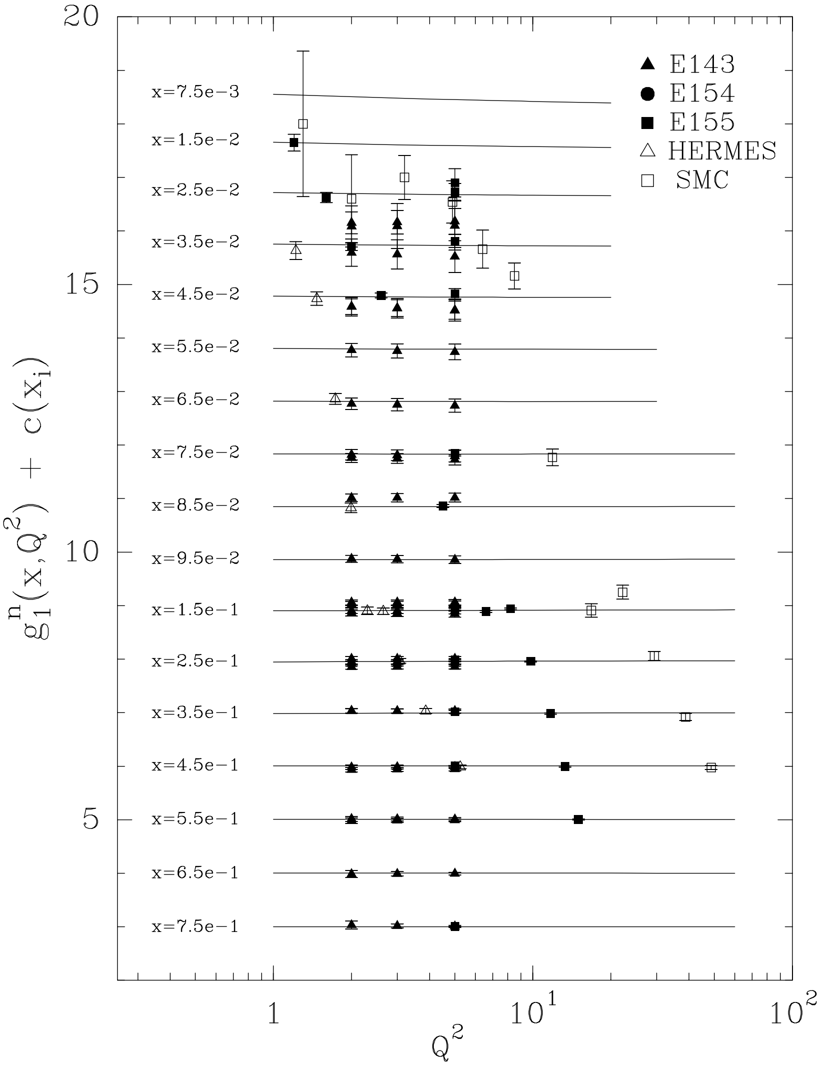

Figure 103: $g_1^n(x, Q^2)$ as function of Q^2 for different x values. The function $c(x_i) = 19 - i$, $i = 0$ corresponds to $x = 7.5\ 10^{-3}$. Experimental data are rebined to the nearest x values.

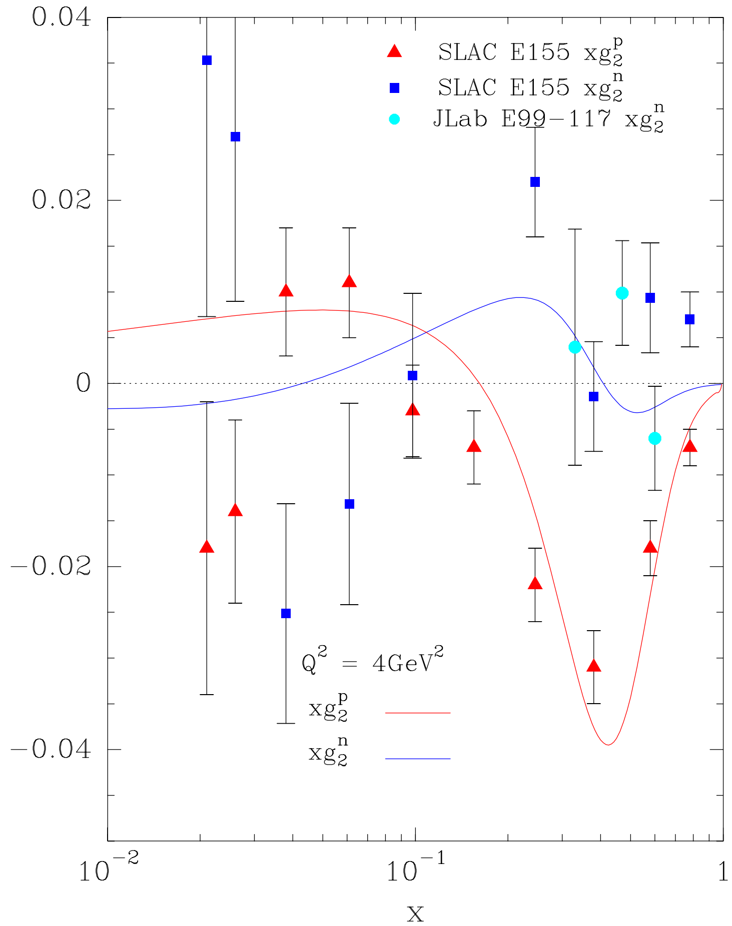

Figure 104: xg_2 for proton and neutron as a function of x, for $Q^2 = 4\text{GeV}^2$. Data from SLAC E155 [77], JLab E99-117 [54].

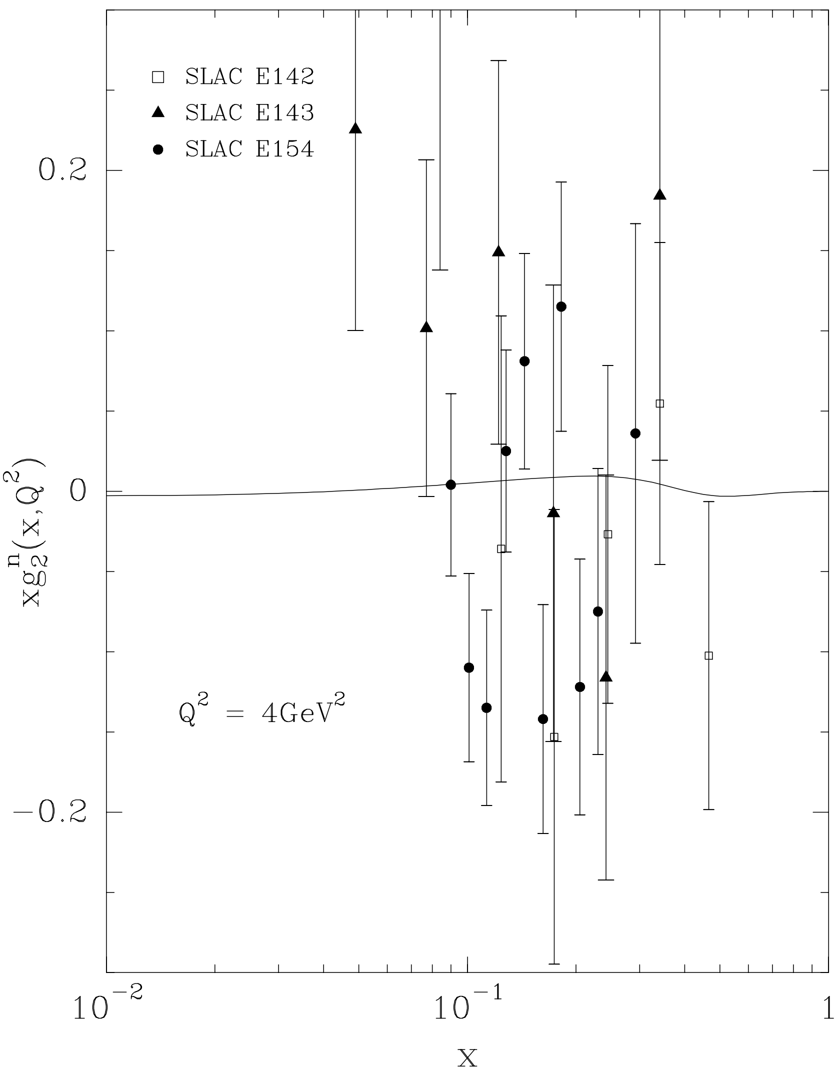

Figure 105: xg_2 for neutron as a function of x, for $Q^2 = 4\text{GeV}^2$. Data from E142, E143, E154 [66]-[72].

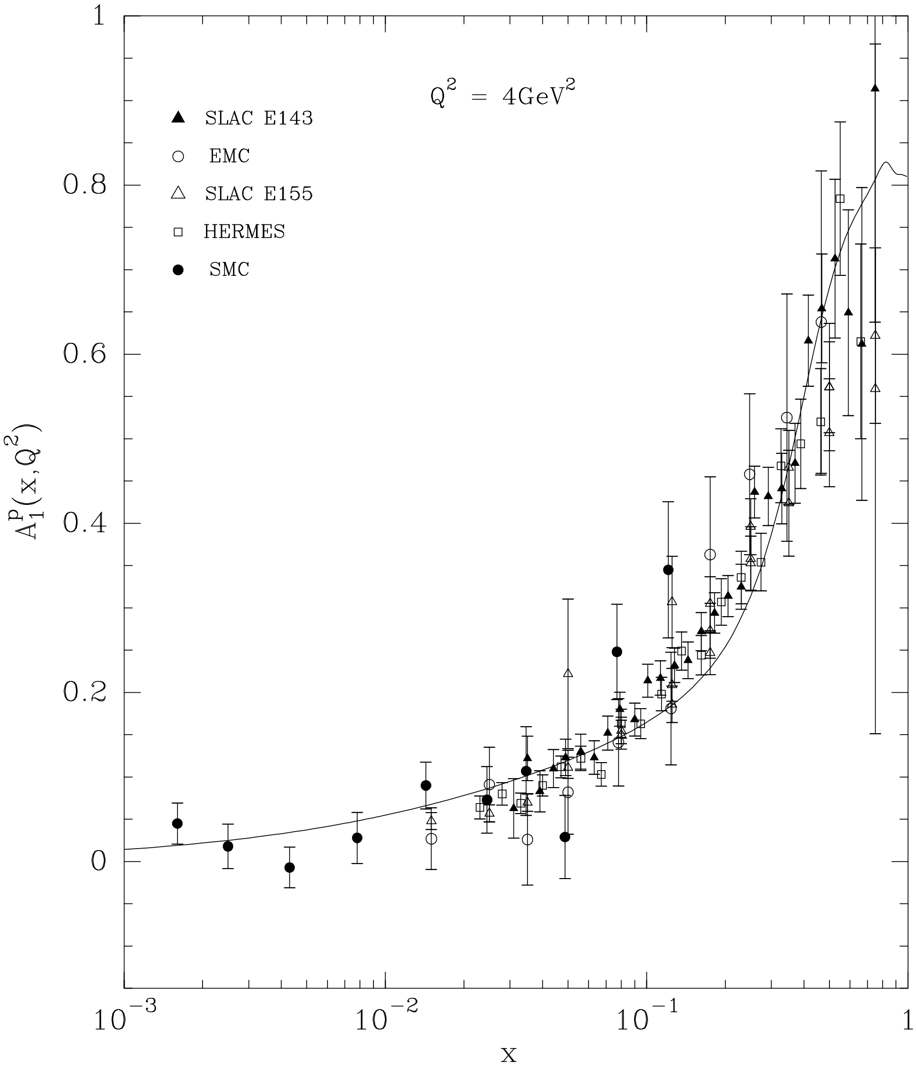

Figure 106: A_1^p as a function of x, for $Q^2 = 4\text{GeV}^2$. Data from E143[70], EMC[35], E155[76], HERMES[48], SMC[81].

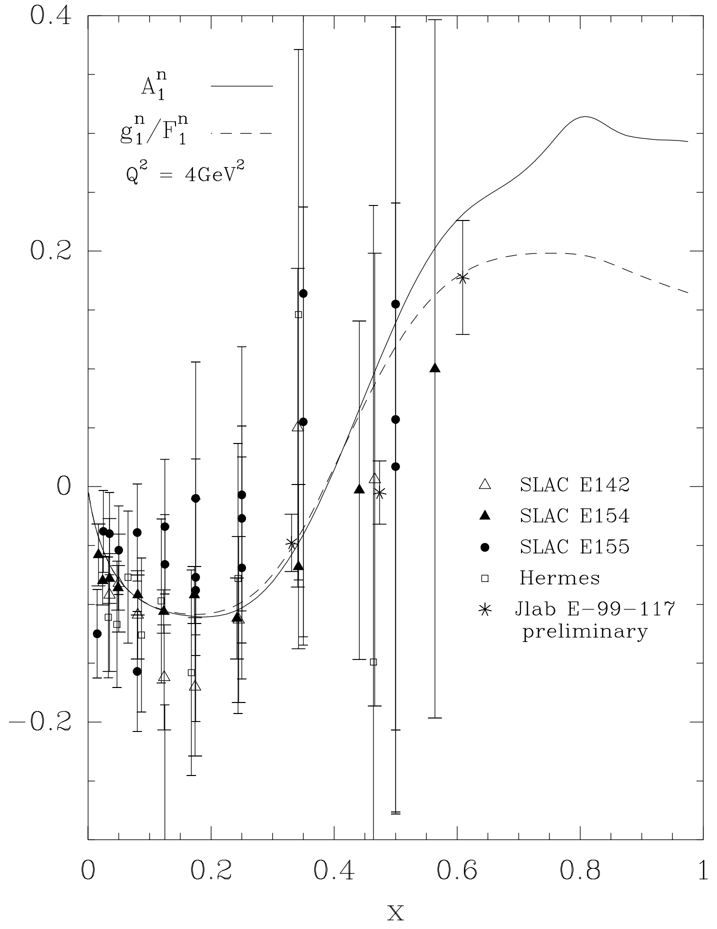

Figure 107: A_1^n as a function of x, for $Q^2 = 4\text{GeV}^2$ solid curve, g_1^n/F_1^n dashed curve. Data from E142[66], E155[76], E154[74], HERMES[49], Jlab E-99-117[53].

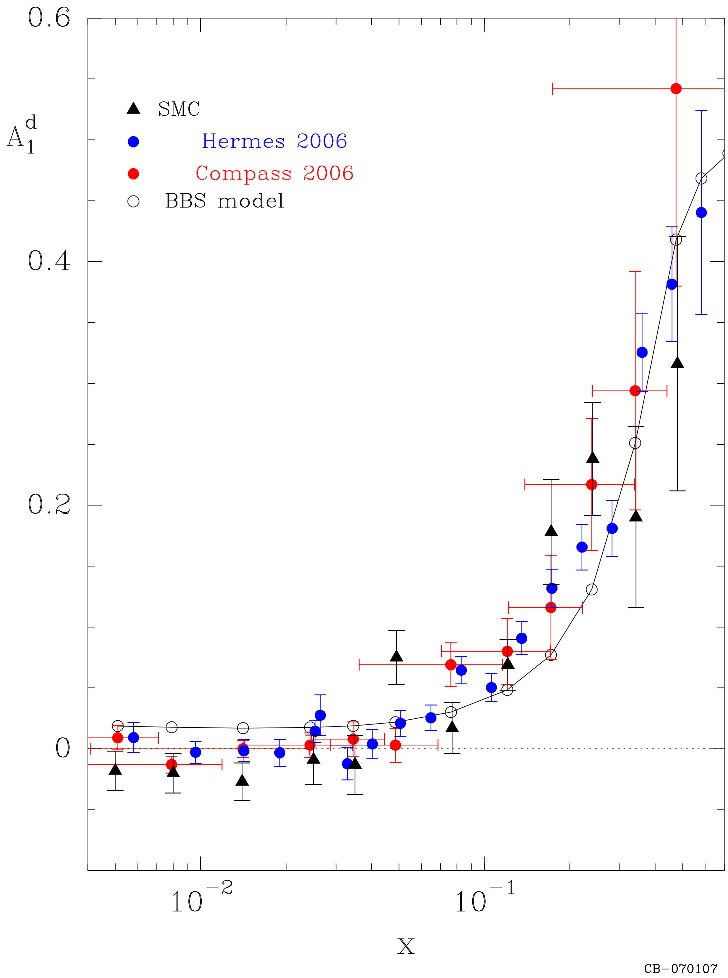

Figure 108: The longitudinal spin asymmetry A_1^d as a function of x. Data from Compass, Hermes, SMC Collaborations [113, 114, 115].

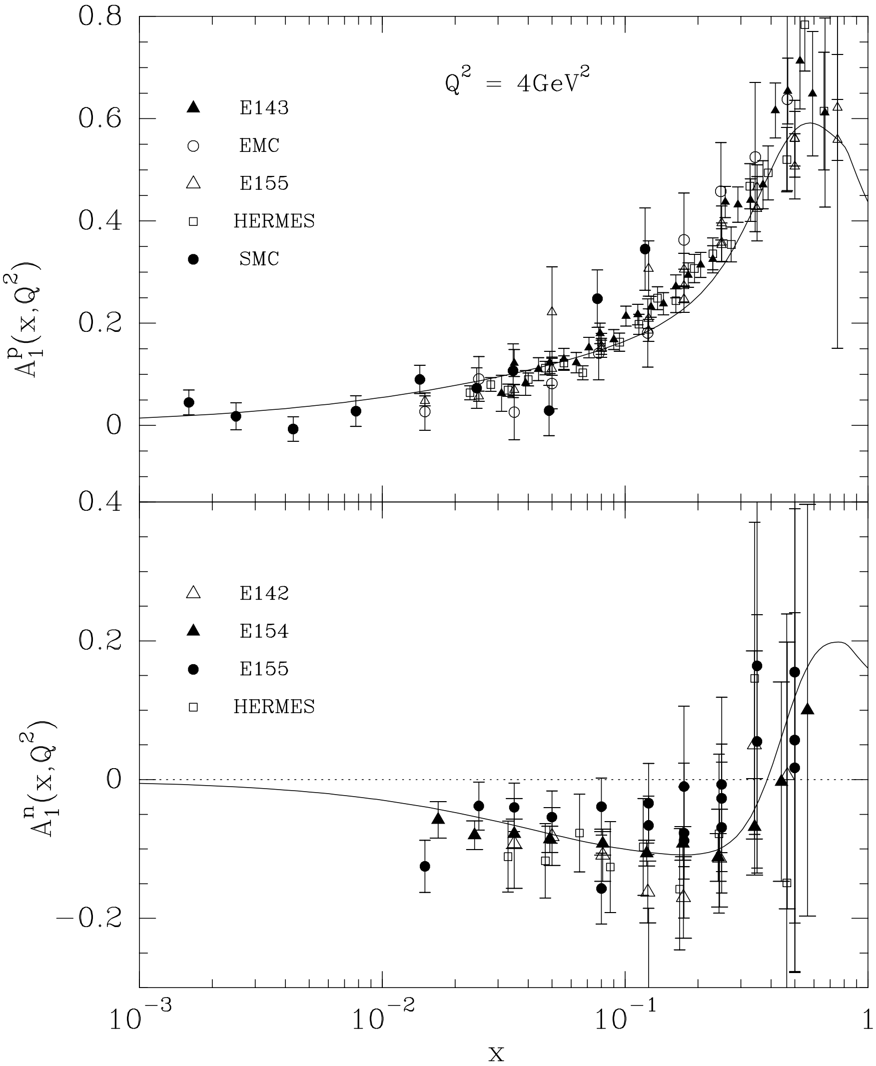

Figure 109: Compilation of the asymmetries A_1^p and A_1^n from E155, E154, E142, E143, EMC, SMC and HERMES experiments [33]-[69]. The curves correspond to our model predictions at $Q^2 = 4\text{GeV}^2$.

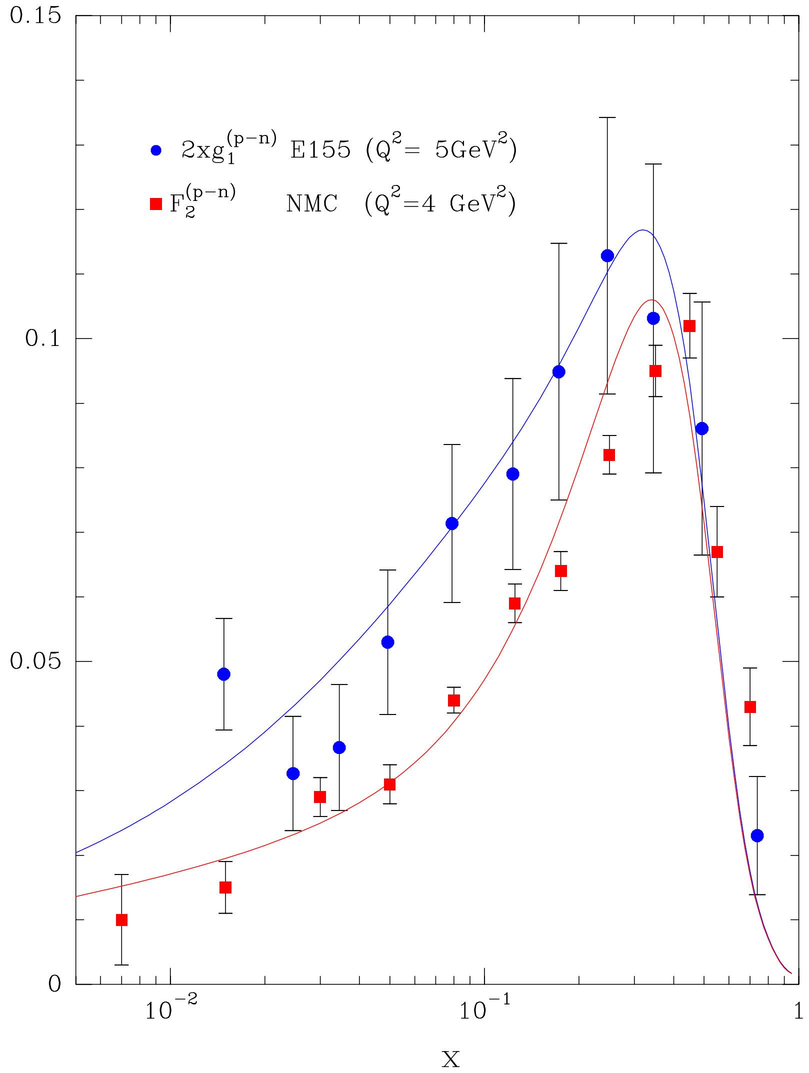

Figure 110: The quantities $2x(g_1^p - g_1^n)$ and $F_2^p - F_2^n$ as function of x at fixed $Q^2 = 4 - 5\text{GeV}^2$, calculated from E155, NMC Coll. Curves are model predictions.

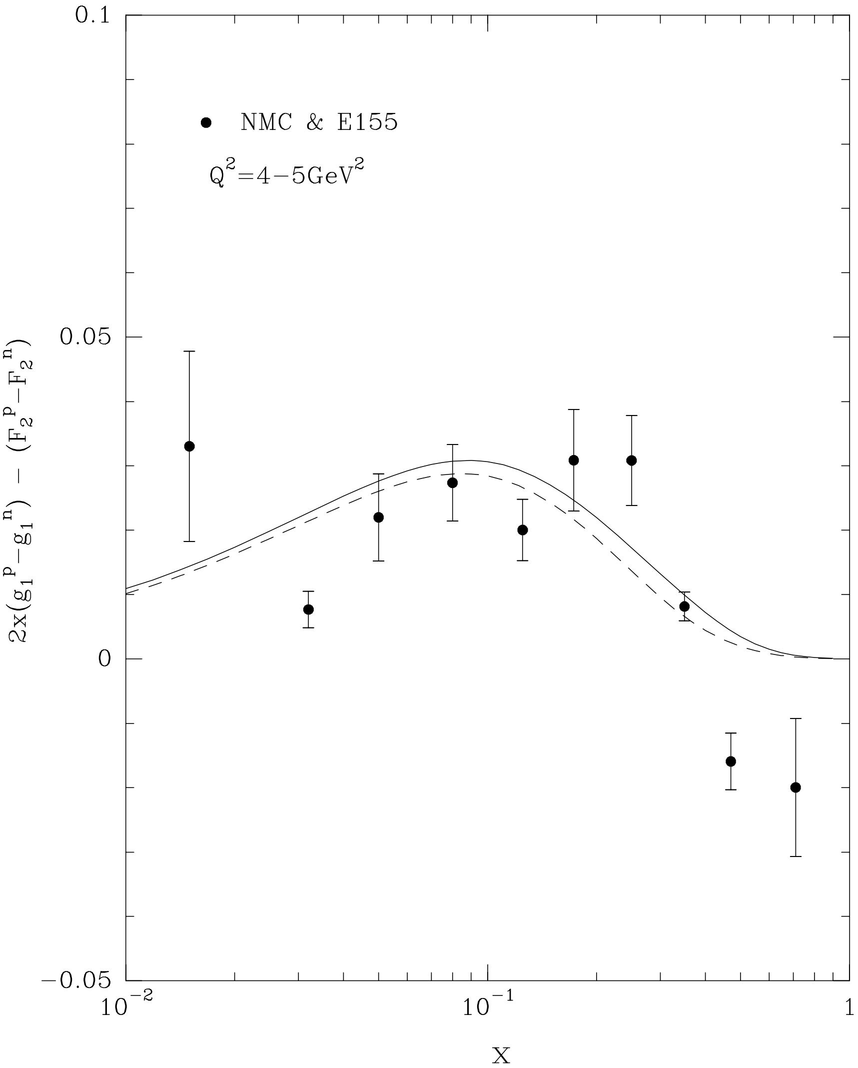

Figure 111: The quantity $2x(g_1^p - g_1^n) - (F_2^p - F_2^n)$ as function of x at fixed $Q^2 = 4 - 5\mathrm{GeV}^2$, calculated from E155, NMC Coll. Comparison with the difference $d^- - u^-$ as a function of x, $Q^2 = 4\mathrm{GeV}^2$. $2/3(d^- - u^- + \bar{d}^- - \bar{u}^-)$, solid curve, $2/3(\bar{d}^- - \bar{u}^-)$, dashed curve.

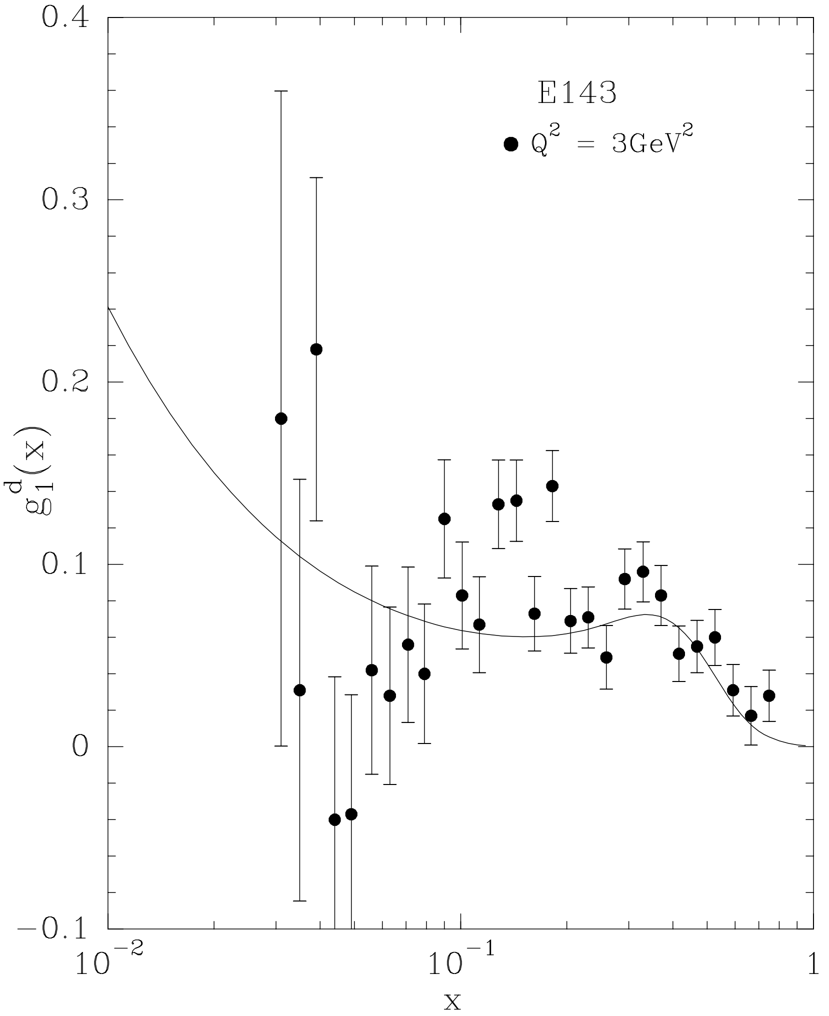

Figure 112: $g_1^d(x, Q^2)$ as function of x at fixed $Q^2 = 3\mathrm{GeV}^2$, E143 Coll.

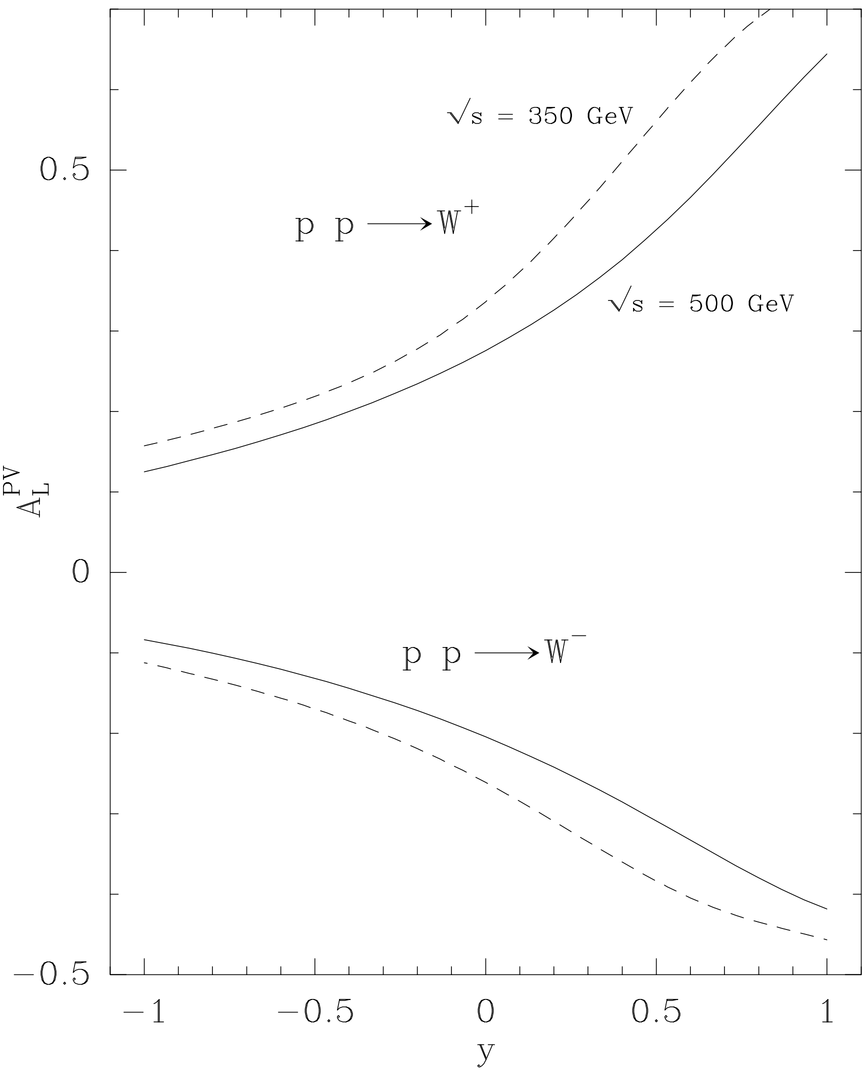

Figure 113: The parity violating asymmetry A_L^{PV} for $pp \to W^{\pm}$ production versus the rapidity y at $\sqrt{s} = 350, 500$GeV (dashed, solid).

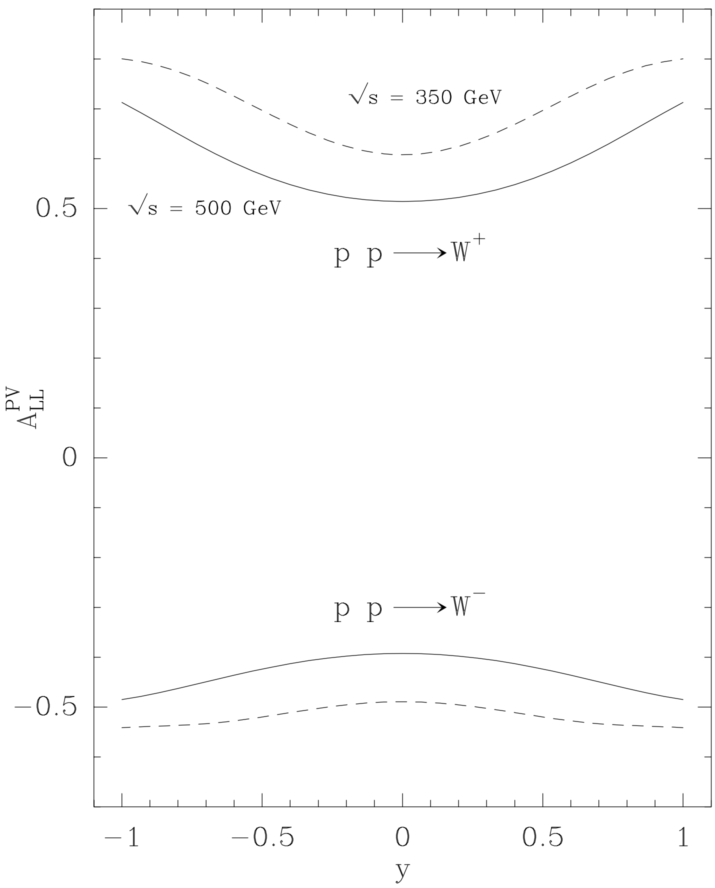

Figure 114: The parity violating asymmetry A_{LL}^{PV} versus the rapidity y for $pp \to W^{\pm}$ production at $\sqrt{s} = 350, 500\mathrm{GeV}$ (dashed, solid).

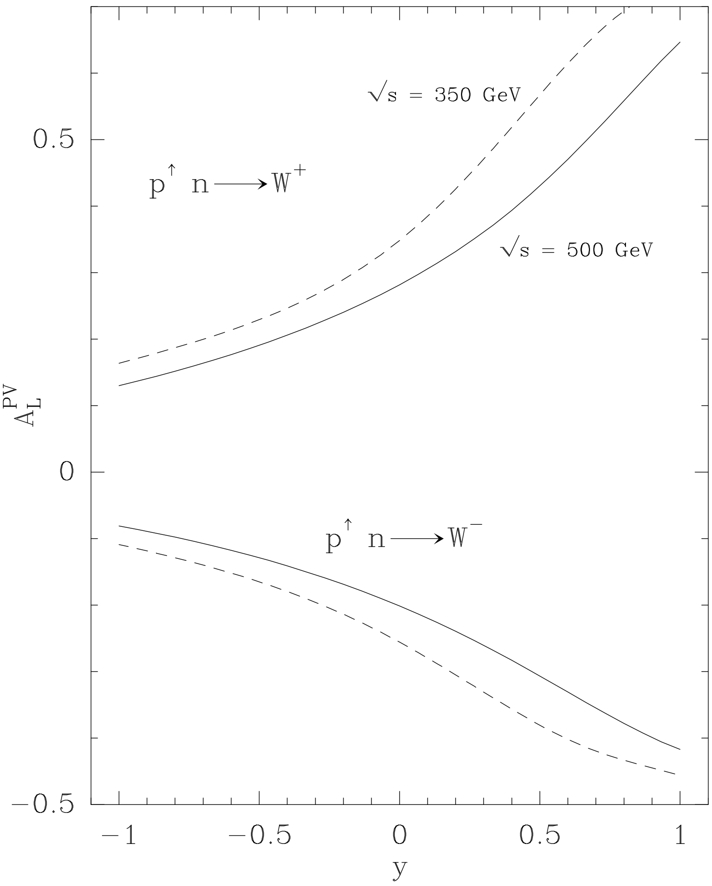

Figure 115: The parity violating asymmetry A_L^{PV} with polarized proton for $p^{\uparrow}n \to W^{\pm}$ production versus the rapidity y at $\sqrt{s} = 350, 500\text{GeV}$ (dashed, solid).

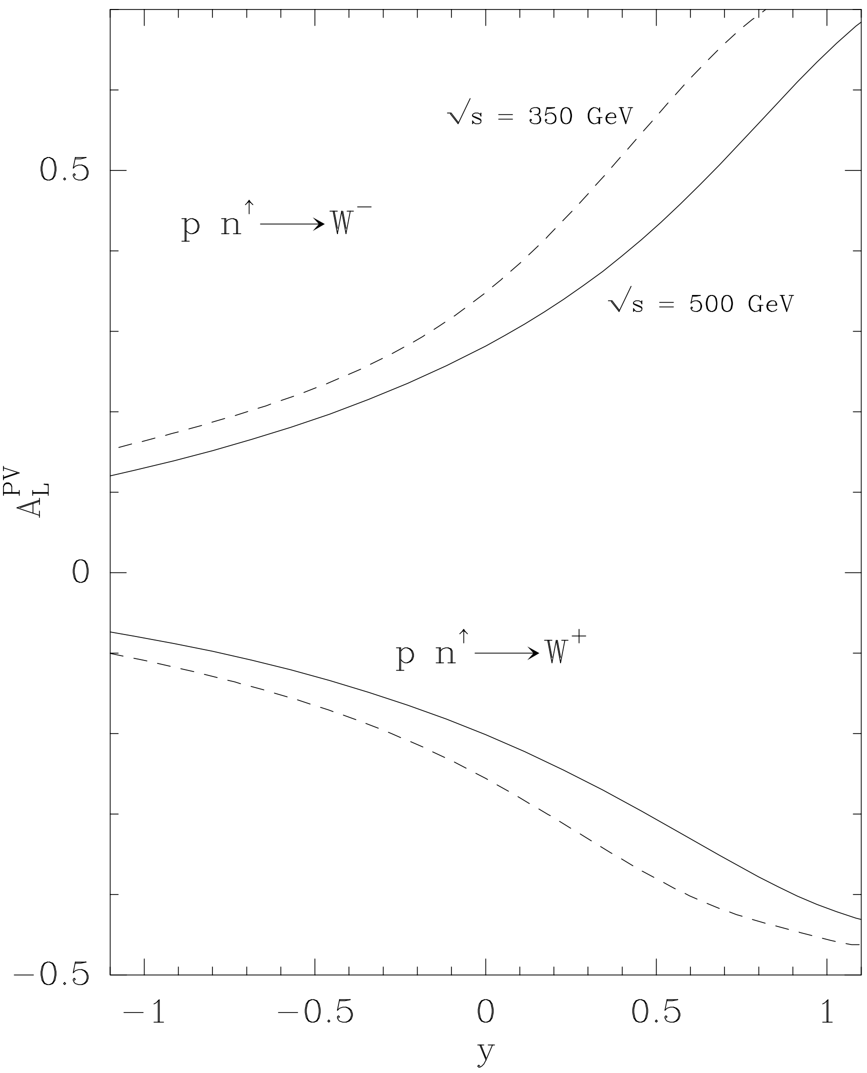

Figure 116: Parity violating asymmetry A_L^{PV} with a polarized neutron for $pn^{\uparrow} \to W^{\pm}$ production versus the rapidity y at $\sqrt{s} = 350, 500$GeV (dashed, solid) .

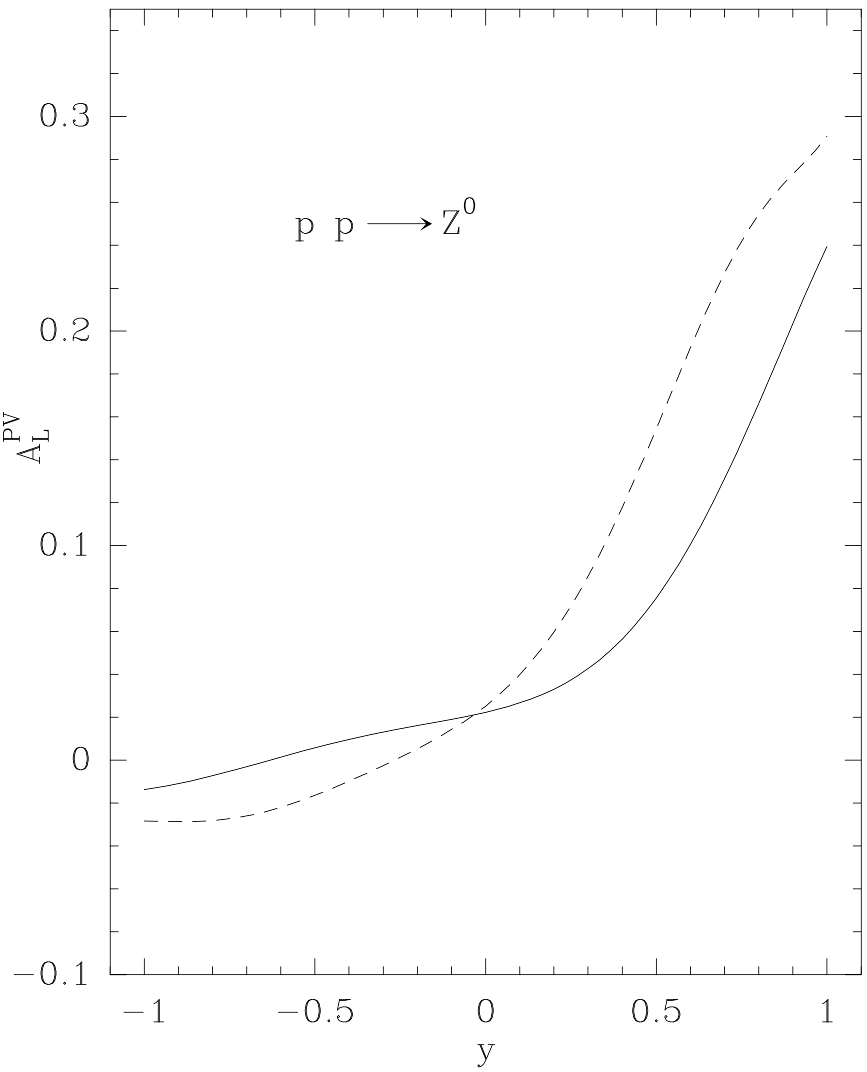

Figure 117: The parity violating asymmetry A_L^{PV} for $pp \to Z^0$ production versus the rapidity y at $\sqrt{s} = 350, 500$GeV (dashed, solid).

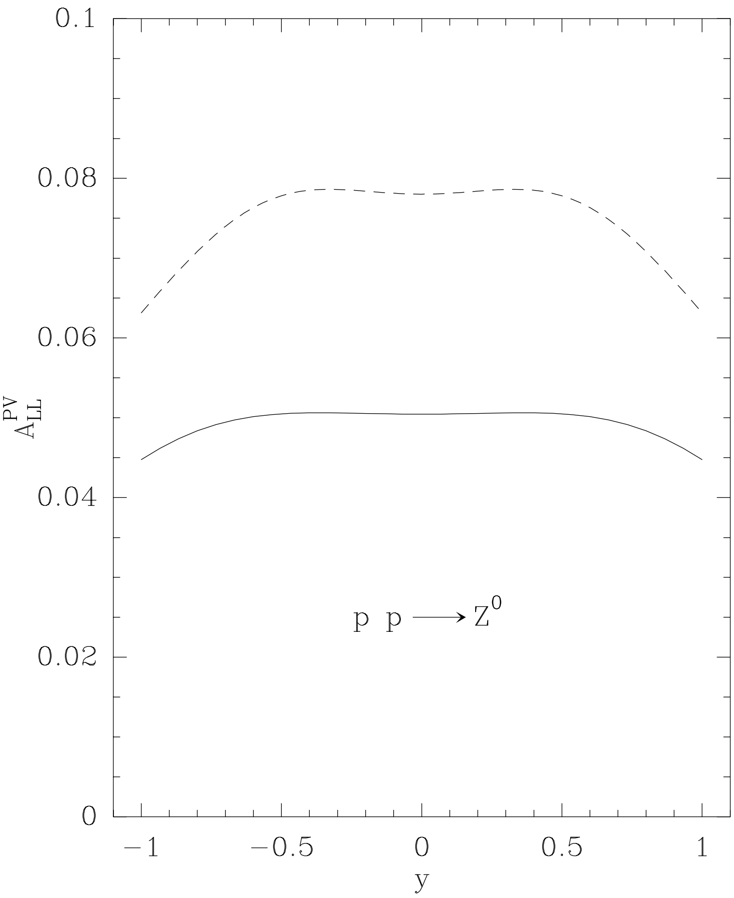

Figure 118: The parity violating asymmetry A_{LL}^{PV} versus the rapidity y for Z^0 production at $\sqrt{s} = 350, 500$GeV (dashed, solid).

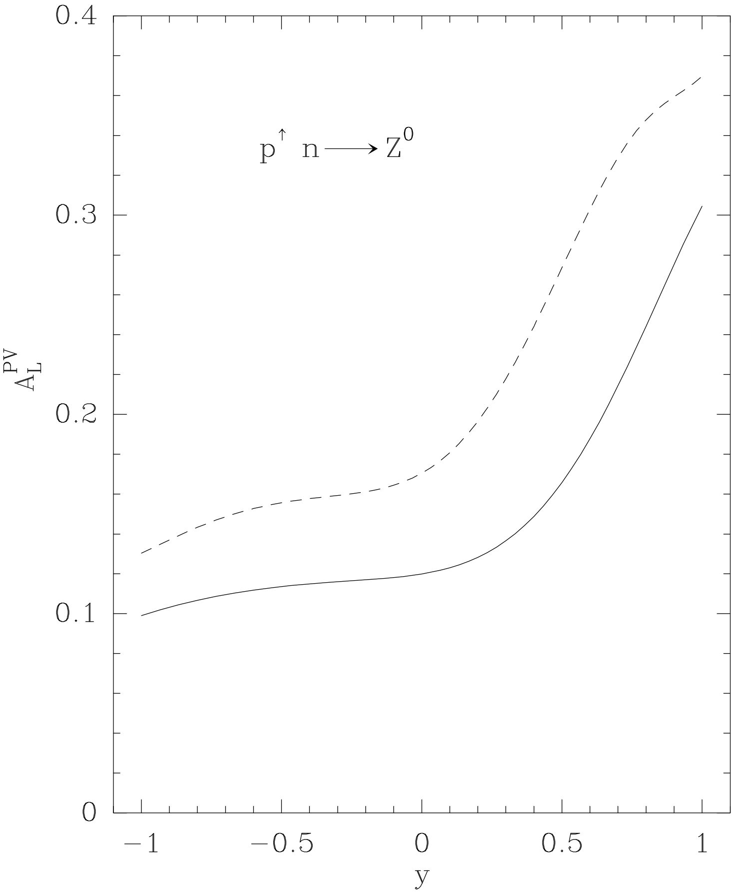

Figure 119: The parity violating asymmetry A_L^{PV} for $p^\uparrow n \to Z^0$ production versus the rapidity y at $\sqrt{s} = 350, 500\text{GeV}$ (dashed, solid).

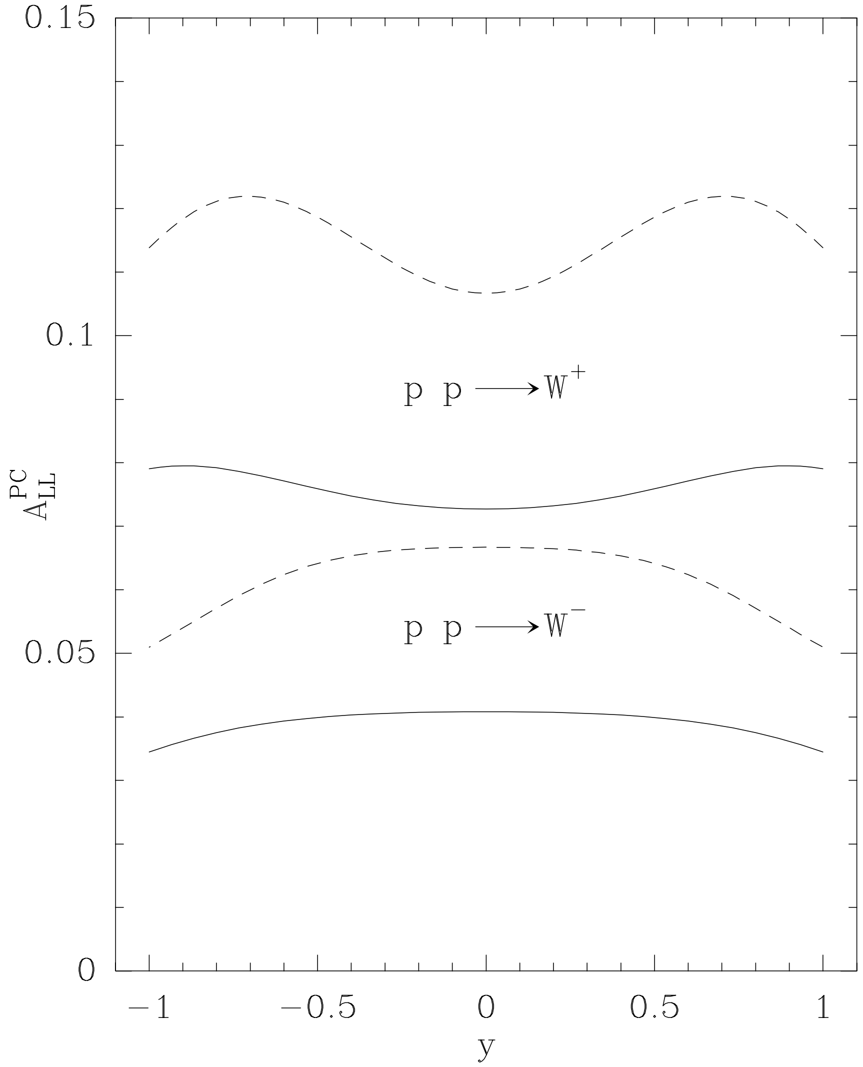

Figure 120: Parity conserving double helicity asymmetry A_{LL}^{PC} for $pp \to W^{\pm}$ production versus the rapidity y at $\sqrt{s} = 350, 500\text{GeV}$ (dashed, solid) .

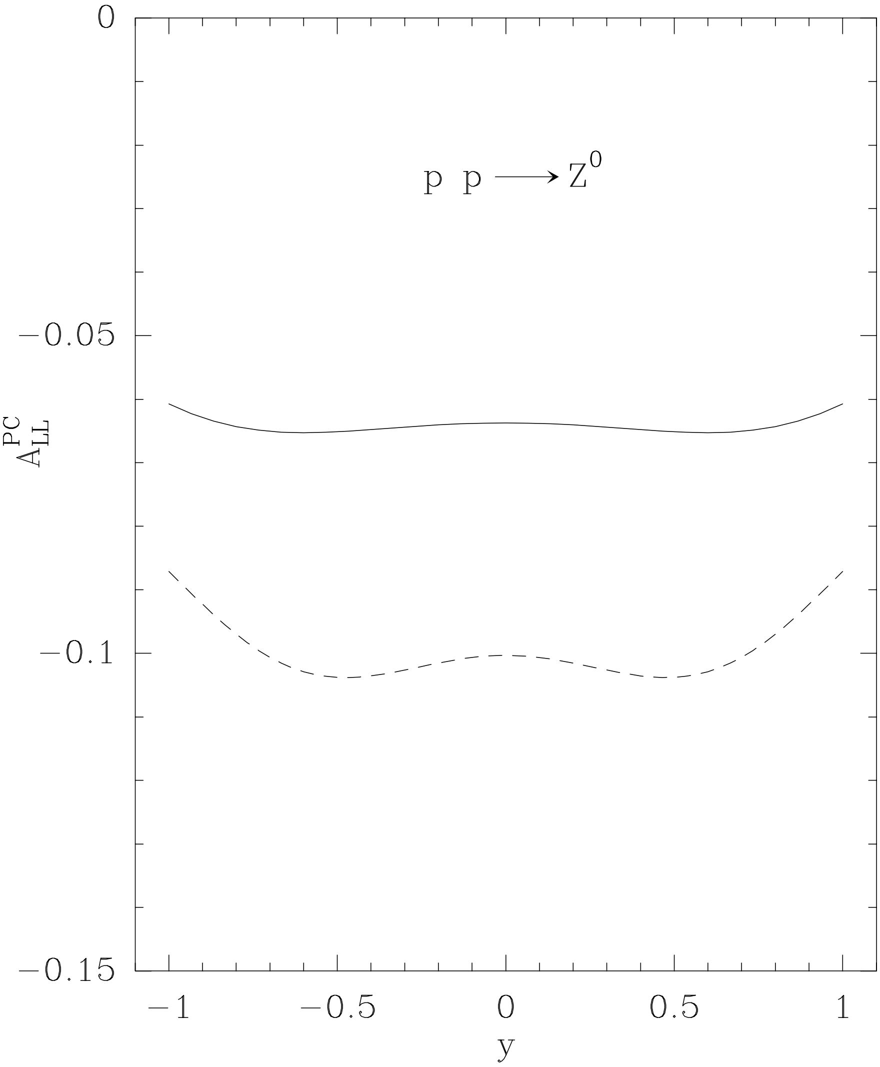

Figure 121: Parity conserving double helicity asymmetry A_{LL}^{PC} for $pp \to Z^0$ production versus the rapidity y at $\sqrt{s} = 350, 500\text{GeV}$ (dashed, solid) .

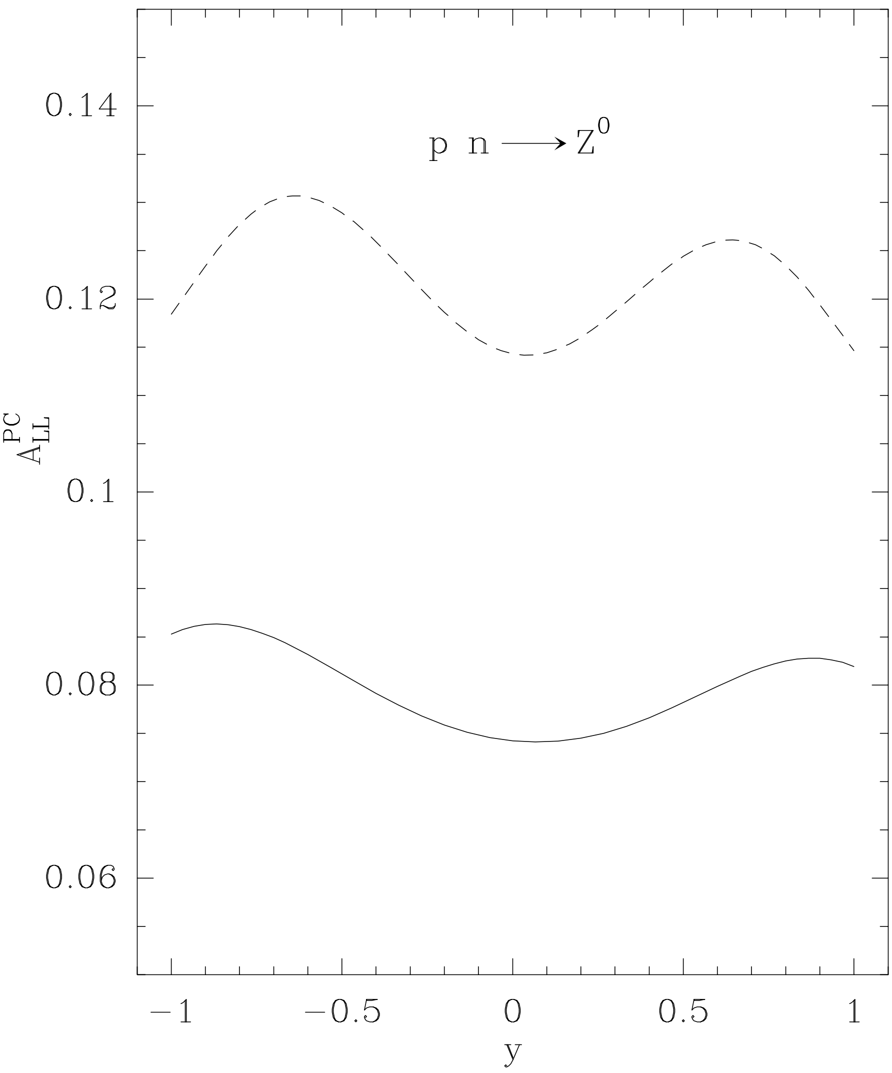

Figure 122: Parity conserving double helicity asymmetry A_{LL}^{PC} for $pn \rightarrow Z^0$ production versus the rapidity y at $\sqrt{s} = 350, 500$GeV (dashed, solid) .

References

[1] "A statistical approach for polarized parton distributions"
C. Bourrely, F. Buccella and J. Soffer, Eur. Phys. J. C **23** (2002) 487 (hep-ph/0109160).

[2] "Recent tests for the statistical parton distributions"
C. Bourrely, F. Buccella and J. Soffer, Mod. Phys. Lett. A **18** (2003) 771 (hep-ph/0211389).

[3] " Statistical approach for unpolarized fragmentation functions for the octet baryons"
C. Bourrely and J. Soffer, Phys. Rev. D **68** (2003) 014003 (hep-ph/0305070).

[4] "The statistical parton distributions: status and prospects"
C. Bourrely, F. Buccella and J. Soffer, Eur. Phys. J. C **41** (2005) 327 (hep-ph/0502180).

[5] "The extension to the transverse momentum of the statistical parton distributions"
C. Bourrely, F. Buccella and J. Soffer, Mod. Phys. Lett. A **21** (2006) 143 (hep-ph/0507328).

[6] " Strangeness asymmetry of the nucleon in the statistical parton model"
C. Bourrely, F. Buccella and J. Soffer, Phys. Lett. B **648** (2007) 39 (hep-ph/0702221).

[7] AFS Collaboration, E. Anassontzis *et al.*, Sov. J. Nucl. Phys. **51**, 836 (1990).

[8] ALEPH Collaboration, D. Buskulic *et al.*, Z. Phys. C **66**, 355 (1995).

[9] ALEPH Collaboration, R. Barate *et al.*, Phys. Rep. C **294**, 1 (1998).

[10] P. Amaudruz *et al.*, Nucl. Phys. B **371**, 3 (1995).

[11] BCDMS Collaboration, A. C. Benvenuti *et al.*, Phys. Lett. B **223**, 485 (1989).

[12] BCDMS Collaboration, A. C. Benvenuti *et al.*, Phys. Lett. B **237**, 592 (1989) .

[13] CCFR Collaboration, P. Z. Quintas *et al.*, Phys. Rev. Lett. **71**, 1307 (1993); W. C. Leung *et al.*, Phys. Lett. B **317**, 655 (1993); W. G. Seligman *et al.*, Phys. Rev. Lett. **79**, 1213 (1997); J. H. Kim *et al.*, Phys. Rev. Lett. **81**, 3595 (1998); U. K. Yang *et al.*, Phys. Rev. Lett. **86**, 2741 (2001).

[14] CCFR Collaboration, A.O. Bazarko *et al.*, Z. Phys. C **65**, 189 (1995).

[15] CELLO Collaboration, H. J. Behrend *et al.*, Z. Phys. C **46**, 397 (1990).

[16] CLAS Collaboration, R. Fatemi *et al.*, Phys. Rev. Lett. **91**, 222002 (2003) [nucl-ex/0306019].

[17] CDF Collaboration, T. Affolder *et al.*, Phys. Rev. D **64**, 032001 (2001).

[18] D0 Collaboration, B. Abbott *et al.*, Phys. Rev. D **64**, 032003 (2001).

[19] B. Dressler *et al.*, Eur. Phys. J. C **14**, 147 (2000).

[20] DELPHI Collaboration, P. Abreu *et al.*, Nucl. Phys. B **444**, 3 (1995).

[21] DELPHI Collaboration, P. Abreu *et al.*, Phys. Lett. B **318**, 249 (1993).

[22] DELPHI Collaboration, P. Abreu *et al.*, Z. Phys. C **67**, 543 (1995).

[23] FNAL E665 Collaboration, M. R. Adams *et al.*, Phys. Rev. D **54**, 3006 (1996)

[24] FNAL E665 Collaboration, M. R. Adams *et al.*, Phys. Rev. Lett. **75**, 1466 (1996)

[25] FNAL Nusea Collaboration, E. A. Hawker *et al.*, Phys. Rev. Lett. **80**, 3715 (1998); J. C. Peng *et al.*, Phys. Rev. D **58**, 092004 (1998); R. S. Towell *et al.*, Phys. Rev. D **64**, 052002 (2001)

[26] FNAL E866/NuSea Collaboration, J.C. Webb *et al.*, submitted to Phys. Rev. Lett. [hep-ex/0302019].

[27] FNAL E605 Collaboration, G. Moreno *et al.*, Phys. Rev. D **43**, 2815 (1991).

[28] FNAL E772 Collaboration, P.L. McGaughey *et al.*, Phys. Rev. D **50**, 3038 (1994), D **60**, 119903 (1999).

[29] CCFR Collaboration, U.K. Yang *et al.*, Phys. Rev. Lett. **87**, 251802 (2001); U.K. Yang Ph. D. Thesis, University of Rochester (2001).

[30] NuTeVPack is available at www-nutev.phyast.pitt.edu/results_2004/nutev_sf.html

[31] NuTeV Collaboration, D. Naples *et al.*, Proceedings from DIS03, St. Petersburg, Russia, April 2003. V. Radescu, XII International Workshop on Deep Inelastic Scattering, Slovakia (April 2004).

[32] Experiment E94-110 at TJNAF, Z.-E. Meziani and P. Souder, update to E99-117, Z.-E. Meziani, J. P. Chen and P. Souder.

[33] EMC Collaboration, J. Ashman *et al.*, Phys. Lett. B **206**, 364 (1988).

[34] EMC Collaboration, J. Ashman *et al.*, Phys. Lett. B **206**, 364 (1988).

[35] EMC Collaboration, Ashman *et al.*, Nuc. Phys. B **328**, 1 (1989).

[36] EMC Collaboration, M. Arneodo *et al.*, Nucl. Phys. B **321**, 541 (1989).

[37] H1 Collaboration, S. Aid *et al.*, Nucl. Phys. B **470**, 3 (1996); T. Ahmed *et al.*, Nucl. Phys. B **439**, 471 (1995); C. Adloff *et al.*, Nucl. Phys. B **497**, 3 (1996).

[38] H1 Collaboration, C. Adloff *et al.*, Eur. Phys. J. C **13**, 609 (2000).

[39] H1 Collaboration, S. Aid *et al.*, Nucl. Phys. B **449**, 3 (1995).

[40] H1 Collaboration, C. Adloff *et al.*, Eur. Phys. J. C **19**, 269 (2001) [hep-ex/0012052].

[41] H1 Collaboration, C. Adloff *et al.*, Eur. Phys. J. C **30**, 1 (2003) [hep-ex/0304003].

[42] Z. Zhang, *'New insights into the proton structure with ep collider HERA'*, LAL 00-57 [hep-ph/0012249].

[43] HERMES Collaboration, S. Belostotski, O. Grebenyuk and Yu. Naryshkin, Acta Physica Polonica B **33**, 3785 (2002).

[44] HERMES Collaboration, K. Ackerstaff *et al.*, Phys. Lett. B **404**, 383 (1997); Phys. Lett. B **464**, 123 (1999); A. Airapetian *et al.*, Phys. Lett. B **442**, 484 (1998).

[45] Jefferson Lab Hall A Collaboration, X. Zheng *et al.*, Phys. Rev. Lett. 92, 012004 (2004).

[46] HERMES Collaboration, A. Airapetian *et al.*, Phys. Rev. Lett. **92**, 012005 (2004) [hep-ex/0307064].

[47] HERMES Collaboration, H.E. Jakson, Int. J. Mod. Phys. A **17**, 3551 (2002).

[48] HERMES Collaboration, A. Airapetian *et al.*, Phys. Lett. B **442**, 484 (1998).

[49] HERMES Collaboration, K. Ackerstaff *et al.*, Phys. Lett. B **404**, 383 (1997).

[50] HRS Collaboration, P. Baringer *et al.*, Phys. Rev. Lett. **56**, 1346 (1986).

[51] HRS Collaboration, M. Derick *et al.*, Phys. Rev. D **45**, 2639 (1987).

[52] HRS Collaboration, T. L. Geld *et al.*, Phys. Rev. D **45**, 3949 (1992).

[53] Jlab E99-117 Collaboration, X. Zheng *et al.*, Phys. Rev. Lett. **92**, 012004 (2004) [nuc-ex/0308011].

[54] JLab E99-117 Collaboration, X. Zheng *et al.*, Phys. Rev. C **70**, 065207 (2004) [nucl-ex/0405006].

[55] L3 Collaboration, M. Acciari *et al.*, Phys. Lett. B **328**, 223 (1994).

[56] NMC Collaboration, M. Arneodo *et al.* Phys. Rev. D **50**, R1 (1994) and references therein; P. Amaudruz *et al.*, Phys. Rev. Lett. **66**, 2712 (1991); Nucl. Phys. B **371**, 3 (1995)

[57] NMC Collaboration, D. Allasia *et al.*, Phys. Lett. B **258**, 493 (1991)

[58] NMC Collaboration, M. Arneodo *et al.*, Phys. Lett. B **364**, 107 (1995); Nucl. Phys. B **483**, 3 (1997)

[59] NMC Collaboration, M. Arneodo *et al.*, Phys. Rev. D **50** (1994) R1.

[60] NMC Collaboration, M. Arneodo *et al.*, Phys. Rev. D **50**, R1 (1994) and references therein; Phys. Lett. B **364**, 107 (1995).

[61] OPAL Collaboration, G. Alexander *et al.*, Z. Phys C **73**, 569 (1997); *ibid.* **73**, 587 (1997).

[62] PHENIX Collaboration, S.S. Adler *et al.*, Phys. Rev. Lett. **91**, 241803 (2003) [hep-ex/0304038].

[63] R806 Collaboration, C. Kourkoumalis *et al.*, Z. Phys. C **5**, 95 (1980).

[64] SLAC E80 Collaboration, M. J. Alguard *et al.*, Phys. Lett. **37**, 1261 (1976); *ibidem* **41**, 70 (1978).

[65] SLAC E130 Collaboration, G. Baum *et al.*, Phys. Rev. Lett. **51**, 1135 (1983).

[66] SLAC E142 Collaboration, P.L. Anthony *et al.*, Phys. Rev. D **54**, 6620 (1996).

[67] SLAC E142 Collaboration, P. L. Anthony *et al.*, Phys. Rev. Lett. **71**, 959; Phys. Rev. D**54**, 6620 (1996).

[68] SLAC E143 Collaboration, K. Abe *et al.*, Phys. Lett. B **452**, 194 (1999).

[69] SLAC E143 Collaboration, K. Abe *et al.*, Phys. Rev. Lett. **75**, 25 (1995); Phys. Rev. D **58**, 112003 (1998).

[70] SLAC E143 Collaboration, K. Abe *et al.*, Phys. Rev. D **58**, 112003 (1998).

[71] SLAC E143 Collaboration, K. Abe *et al.*, Phys. Rev. Lett. **74**, 346 (1995).

[72] SLAC E154 Collaboration, K. Abe *et al.*, Phys. Lett. B **404**, 377 (1997).

[73] SLAC E154 Collaboration, K. Abe *et al.*, Phys. Lett. B **405**, 180 (1997); Phys. Rev. Lett. **79**, 26 (1997)

[74] SLAC E154 Collaboration, K. Abe *et al.*, Phys. Rev. Lett. **79**, 26 (1997).

[75] SLAC E154 Collaboration, K. Abe *et al.* Phys. Lett. B **405**, 180 (1997).

[76] SLAC E155 Collaboration, P. L. Anthony *et al.*, Phys. Lett. B **493**, 19 (2000).

[77] SLAC E155 Collaboration, P.L. Anthony *et al.*, Phys. Lett. B **553**, 18 (2003) [hep-ex/0204028].

[78] SLAC E155 Collaboration, P.L. Anthony *et al.*, Phys. Lett. B **458**, 529 (1999).

[79] SLD Collaboration, K. Abe *et al.*, Phys. Rev. D **59**, 052001 (1999).

[80] SMC Collaboration, B. Adeva *et al.*, Phys. Rev. D **58**, 112001 (1998); Phys. Rev. D **60**, 072004 (1999)

[81] SMC Collaboration, Adeva *et al.*, Phys. Rev. D **60** ,072004 (1999).

[82] Spin Muon Collaboration, D. Adams *et al.*, Phys. Lett. B**329**, 339 (1994); Erratum, Phys. Lett. B **339**, 332 (1994); *ibidem* B **396**, 338 (1997); B. Adeva *et al.*, Phys. Lett. B **412**, 414 (1997).

[83] Spin Muon Collaboration, D. Adams *et al.* 1995 Phys. Lett. B**357**, 248 (1995); Phys. Rev. D **56**, 5330 (1997); B. Adeva *et al.*, Phys. Rev. D **58**, 112001 (1998).

[84] A. Daleo, C.A. García Canal, G.A. Navarro and R. Sassot, Int. J. Mod. Phys. A**17**, 269 (2002) [hep-ph/0106156].

[85] TASSO Collaboration, R. Brandelik *et al.*, Phys. Lett. B **105**, 75 (1981).

[86] TASSO Collaboration, M. Althoff *et al.*, Z. Phys C **17**, 5 (1983).

[87] TASSO Collaboration, M. Althoff *et al.*, Z. Phys C **27**, 27 (1985).

[88] TASSO Collaboration, W. Braunschweig *et al.*, Z. Phys. C **42**, 189 (1989).

[89] TASSO Collaboration, W. Braunschweig *et al.*, Z. Phys. C **45**, 209 (1990).

[90] TPC Collaboration, H. Aihara *et al.*, Phys. Rev. Lett. **61**, 1263 (1988).

[91] ZEUS Collaboration, M. Derrick *et al.*, Phys. Lett. B **345**, 576 (1995).

[92] ZEUS Collaboration, M. Derrick *et al.*, Phys. Lett. B **316**, 412 (1993); Z. Phys. C **65**, 379 (1995); Z. Phys. C **72**, 399 (1996).

[93] ZEUS Collaboration, J. Breitweg *et al.*, Eur. Phys. J. C **7**, 609 (1999).

[94] ZEUS Collaboration, XXX Int. Conf. High Energy Phys. Osaka (Japan) July 2000, abstract 1049; J. Breitweg *et al.*, Eur. Phys. J. C **11**, 427 (1999).

[95] ZEUS Collaboration, S. Chekanov *et al.*, Eur. Phys. J. c **28**, 175 (2003) [hep-ex/0208040].

[96] ZEUS Collaboration, S. Chekanov *et al.*, Phys. Lett. B **539**, 197 (2002), Err. B **552**, 308 (2003) [hep-ex/0205091].

[97] ZEUS Collaboration, S. Chekanov *et al.*, Eur. Phys. J. C **32**, 1 (2003) [hep-ex/0307043].

[98] J. Soffer and O. Teryaev, Phys. Lett. B **490**, 106 (2000).

[99] F. Zomer, Nucl. Phys. B (Proc. Suppl.) **79**, 115 (1999).

[100] B.A. Kniehl, G. Kramer and B. Potter, Nucl. Phys. B **582**, 514 (2000).

[101] J. Binnewies, B.A. Kniehl and B. Potter, Z. Phys. C **65**, 471 (1995).

[102] COMPASS Collaboration, V.Y Alexakhin *et al.*, hep-ex/0609038.

[103] M. Goncharov *et al.*, Phys. Rev. D 64 (2001) 112006.

[104] M. Hirai, S. Kumano and N. Saito, Phys. Rev. D **74**, 014015 (2006).

[105] D. de Florian, A. Navarro and R. Sassot, Phys. Rev. D **71**, 094018 (2005).

[106] E. Leader, A.V. Sidorov and D.B. Stamenov, Phys. Rev. D **73**, 034023 (2006).

[107] M. Glück, E. Reya, M. Stratmann and W. Vogelsang, Phys. Rev. D **63**, 094005 (2001).

[108] A.D. Martin, R.G. Roberts, W.J. Stirling and R.S. Thorne, Eur. Phys. J. C **28**, 455 (2003).

[109] V.Yu. Alexakhin *et al.* Compass Collaboration, Phys. Lett. B to be published, hep-ex/0609038.

[110] A. Korzenev, Compass Collaboration, XV International Workshop on Deep-Inelastic Scattering and Related Subjects, April 2007, Munich, Germany. hep-ex/0704.3600.

[111] C. Adloff *et al.*, H1 Collaboration, Eur. Phys. J. C **21**, 33 (2001).

[112] C. Adloff *et al.*, H1 Collaboration, Phys. Lett. B **520**, 183 (2001).

[113] V.Yu. Alexakhin *et al.*, Compass Collaboration, Phys. Lett. B **647**, 8 (2007).

[114] A. Airapetian *et al.*, Hermes Collaboration, Phys. Rev. D **75**, 012007 (2007).

[115] B. Adeva *et al.*, SMC Collaboration, Phys. Rev. D **58**, 112001 (1998).

List of Figures